2015-05-05

Integrated Interpretation of Microseismic with Surface Seismic Data in a Tight Gas Reservoir, Central Alberta, Canada

Rafiq, Aamir

UNIVERSITY OF CALGARY

Integrated Interpretation of Microseismic with Surface Seismic Data in a Tight Gas Reservoir, Central Alberta, Canada

by

Aamir Rafiq

A THESIS

SUBMITTED TO THE FACULTY OF GRADUATE STUDIES

IN PARTIAL FULFILMENT OF THE REQUIREMENTS FOR THE

DEGREE OF MASTER OF SCIENCE

GRADUATE PROGRAM IN GEOLOGY AND GEOPHYSICS

CALGARY, ALBERTA

APRIL, 2015

Abstract

Integrated interpretation of microseismicity with surface seismic data can provide valuable information about reservoir characteristics, mechanical stratigraphy, induced and pre-existing fracture systems. Although there are numerous integrated studies that focus on unconventional plays, relatively little attention has been given to tight gas environments. Typical interpretation of microseismic data focuses on the spatial and temporal distribution of microseismic events to estimate stimulated reservoir volume and, in some cases, to infer the character and geometry of discrete fracture networks. This thesis describes a methodology for integrated interpretation of 3D seismic data with microseismicity recorded during the open hole stimulation of two horizontal treatment wells of a tight-sand unit deposited in the Hoadley field, a Cretaceous marine barrier-bar complex in Western Canada. I introduce a novel approach, *Microseismic Facies Analysis (MFA)*, to extract additional information from microseismic clusters. The interpreted microseismic facies are then correlated with surface seismic attributes in order to delineate reservoir partitions that are interpreted to reflect lithofacies variations associated with depositional trends.

Acknowledgements

This thesis would not have been possible without the support of several people, whom I am grateful to consider as friends, mentors and colleagues. I would like to express my special appreciation and thanks to my supervisor, Prof. Dr. David Eaton, for taking me on as a student at the Microseismic Industry Consortium and for his advice, and guidance since very early stages of this research. He has been a great mentor, providing me unyielding encouragement, push and support in various ways.

I am thankful to Maria Gallant, Project Manager at the Microseismic Industry Consortium, for her exceptional, timely help and support. In addition, I would like to thank my friends and colleagues in the Microseismic Industry Consortium for creating a wonderful work environment. As well, I extend my appreciation to my colleague, Dr. Enrico Caffagni, for his positive feedback.

I gratefully acknowledge my dearest friend Dr. Jubran Akram, who always encouraged and supported me, especially when I was under stress and going downhill. I appreciate his time and discussions over long coffee breaks, which shaped my research and this thesis draft. Sincerest thanks to my friend, Wasim Nasir, for his encouragement and positive outlook. If not for you I would have never even considered this endeavor.

I would like to thank the sponsors of the Microseismic Industry Consortium, in particular ConocoPhillips Canada, ESG Solutions, ARCIS Seismic Solutions and Transform for donating this interesting and challenging dataset and software. I extend my appreciation to Larry Matthews, Iris Tomlinson, Chris Bird, Matteo Niccoli and Mohammad Hossein Nemati, who have been always delightfully and cheerfully giving me support and advices during my graduate studies.

Finally and most importantly, I would like to thank my parents whose constant prayers and inseparable support have kept me going through the difficult stages of this journey. Thank you to my family and parents-in-law, especially sister Lubna for her support and prays. Infinite thanks to my nieces Ashhel and Cemal for hugs and smiles that made me persist.

Above all, thank you to my wife, Sadia, for invaluable help, motivation, extraordinary patience, and unconditional love throughout this entire process. Without your encouragement, sense of humor and support, I could not have done this.

Table of Contents

List of Tables

List of Figures and Illustrations

List of Symbols, Abbreviations and Nomenclature

Symbol	**Definition**
AVO	Amplitude variation with offset
GR	Gamma ray
Hz	Hertz
k_1	Most positive curvature
k_2	Most negative curvature
Kmax	Maximum curvature
Kmin	Minimum curvature
KB	Kelly bushing
LAS	Log ASCII standard
mD	Millidarcy
MFA	Microseismic facies analysis
MMb	Million barrels
ms	Millisecond
MS	Microseismic
M_W	Magnitude
P	Compressional
PP	Post pumping
POSTM	Post-stack time migrated
$POSTM_W$	Post-stack time migrated, with spectral whitening
RMS	Root-mean square
S	Shear
STA/LTA	Short- and long-term average ratio
SRD	Seismic reference datum
SRV	Stimulated reservoir volume
SHmax	Maximum horizontal stress
SOM	Structure oriented median
SI	Shape index
Tcf	Trillion cubic feet
TOC	Total organic carbon
TVD	True vertical depth
VSP	Vertical seismic profile
WCSB	Western Canada sedimentary basin
Zp	P-impedance
σ	Standard deviation
λ	Lambda
μ	Mu
ρ	Rho
3D	Three-dimensional

Chapter One: **Introduction**

During the past few decades, the focus of exploration activity has shifted considerably within the Western Canada Sedimentary Basin, and more broadly within North America. Conventional exploration and production technologies have been replaced by technologies currently labeled as "unconventional". The availability of these unconventional technologies such as horizontal drilling, hydraulic fracturing, microseismic monitoring and advanced techniques in seismic interpretation, are playing a significant role in the exploitation of the unconventional resources such as tight sands, shale gas and oil sands (Akram, 2014 and the references therein).

Figure 1.1 shows a pictorial view of the conventional and unconventional reservoirs in the subsurface. Unconventional reservoirs are of lower quality, i.e. permeability ranges from 0.0001mD to 0.1mD and porosity ranges from 3% to 9%. As shown in Table 1.1, unconventional gas reservoirs can be classified into four main types: Natural Gas from Coal (NGC) or CBM, Shale Gas, Tight Gas, and Gas Hydrates. Tight gas reservoirs are natural gas reservoirs with low porosity (3-9%) and low permeability (< 0.1mD). Shale gas reservoirs are reservoirs where natural gas is contained within an organic shale unit. These are characterized by low matrix porosity (3-9%) and are often highly heterogeneous. The mechanical properties are important drivers of productivity in these reservoirs (Williams-Kovacs and Clarkson, 2011).

Canada has an estimated 3900 Tcf of natural gas resources; of this, about 18% comes from conventional sources, while a significant amount of the estimated resource comes from tight gas (~33%), shale gas (~28%), and coal bed methane/coal (~20%). Unconventional gas currently accounts for 30% of Canada's natural gas production (Heffernan and Dawson, 2010).

Table 1.1: Classification of unconventional gas reservoirs (Taken from Williams-Kovacs and Clarkson, 2011).

Resource	Overview
Tight Gas	• Natural gas reservoirs with low porosity (generally 3-9%) and low permeability (<0.1mD, and often <0.01mD) • Primary free gas storage • Clastic (fine-grained sand, silt) or carbonates • Natural fractures may contribute to productivity • Discontinuous sweet spots, multi-layers
Shale Gas	• Natural gas contained within shale sequences • Shale has extremely low permeability (often <0.01mD, sometimes <0.0001mD) • Low matrix porosity (generally 3-9%) • Variable TOC, which affects sorption and mechanical properties • Variable matrix mineralogical properties, often high clay content • Mechanical properties (i.e. brittleness) are key drivers of productivity (due to requirement for hydraulic fracturing to aid production) • Natural fractures may contribute to productivity • Discontinuous sweet spots, multi-layers • Often highly heterogeneous and laminated • Single-phase or multi-phase production
Coalbed Methane	• A deposit comprised of greater than 50% by weight or 70% by volume of organic matter • Primarily absorbed gas due to high organic content and cleats often initially saturated with water, which must be removed prior to significant gas production • Naturally fractured, with fractures being essential to productivity • Primarily composed of Type III organic matter • Stress and desorption sensitive fracture porosity and permeability • Simultaneous gas and water production (multi-phase flow)
Gas Hydrates	• Ice-like substances that are composed of water and natural gas • Form when water and gasses combine at low temperature and high pressure

1.1 Tight gas reservoirs

A tight gas reservoir is simply defined as a low-permeability and low-porosity rock unit, including very fine grained silt/sand or carbonate, containing gas trapped within pore spaces. Tight gas reservoirs generally have less than 9% porosity and less than 0.1mD permeability. Natural fractures may contribute to productivity, but normally horizontal drilling, hydraulic fracturing and microseismic monitoring are required to make these reservoirs economically viable (Naik, 2010).

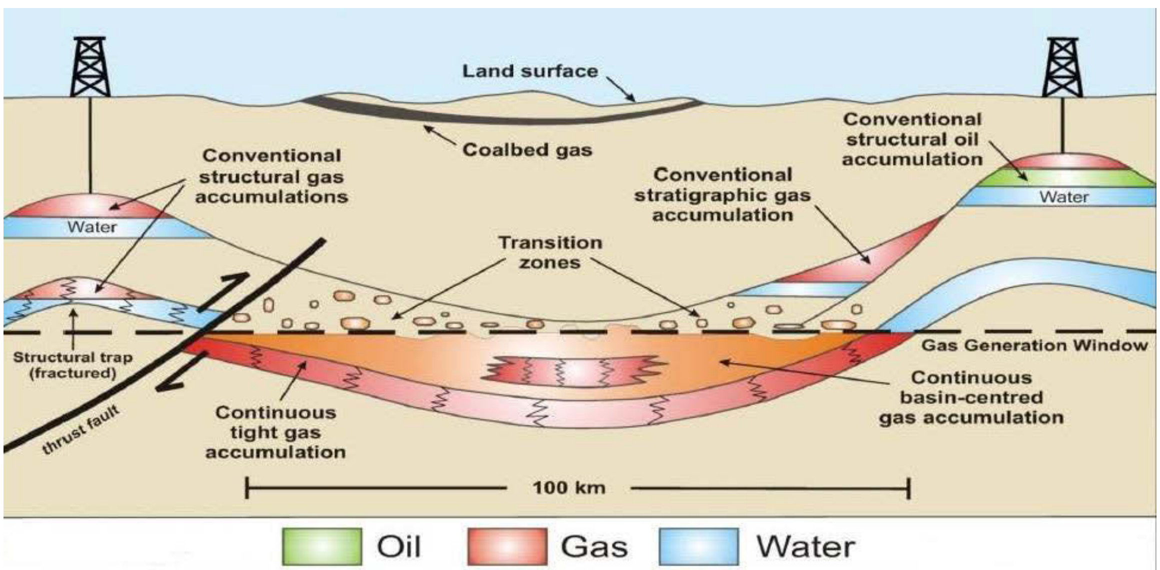

Figure 1.1: Setting of conventional and unconventional reservoirs (Source: CSUR, 2012).

Table 1.2 summarizes some examples of tight gas reservoirs from Western Canada Sedimentary Basin (WCSB). The Glauconitic sand member of Lower Cretaceous Upper Mannville group, which is the reservoir of interest in this study, consists of shallow marine sandstone deposits.

1.2 Hydraulic fracturing

Advanced techniques that make unconventional resources viable to produce commercially are used extensively in North America. Availability of these new technologies has changed the face of classical oil and gas exploration and production. Hydraulic fracturing is one of these technologies; it is defined as a process of transmitting pressure by fluid or gas to create cracks or to open existing crack or fractures in hydrocarbon bearing rocks underground (Nash, 2010).

Table 1.2: Tight gas reservoirs from the Western Canada Sedimentary Basin (modified from Naik, 2010).

Geological Period	Reservoir Formation (Geographic location)
Devonian	• Jean Marie Member (NEBC)
Mississippian/Pennsylvanian/Permian	• Mattson Formation (Liard Basin) • Stoddart Group (NEBC and Peace River Plains)
Triassic	• Montney - Turbidite play (Peace River Plains) • Doig - Shoreface/channel sands (NEBC) • Halfway - NEBC Foothills, Peace River Plains • Baldonnel / Pardonet – (NEBC Foothills)
Jurassic	• Rock Creek (West-Central Alberta) • Nikanassin - Buick Creek (NEBC, West-central Alberta) • Kootenay (South Western Alberta)
Upper Cretaceous	• Dunvegan (West-Central Alberta and B.C.) • Cardium - Kakwa shoreface (West-Central Alberta and B.C.) • Belly River (west-central Alberta)
Lower Cretaceous	• Cadomin / Basal Quartz (Alberta / B.C. western Plains and Foothills) • Bluesky / Gething (Peace River Plains, west central Alberta) • Falher / Notikewin (NEBC and Alberta) • Notikewin / Upper Mannville channels (west-central Alberta) • Cadotte (West-Central Alberta and B.C.) • Viking – (West-Central Alberta) • Base Glauconite (Hoadley, south central Alberta)

Hydraulic fracturing involves injecting fluid into reservoir, known as fracturing fluid, at high pressures deep into borehole. This creates fractures or cracks of few millimeters aperture, sometimes extending for distances of up to hundreds of meters. After the pressure is withdrawn or released, these fractures have a tendency to close, preventing the flow of hydrocarbon. To keep these fractures open, small particles such as sand or ceramic beads, called proppant, are added and pumped with fracturing fluid. The suspended fluid/proppant mixtures fill the open fractures and keep them open after the fracture pressure is released (King, 2012).

After hydraulic fracturing is completed, some of the fluid injected during the injection process flows back as production stream. The flow back period may extend up to two weeks for multistage fracturing and several days for single stage fracturing. The flow back of fracturing fluid decreases while flow back of hydrocarbon content increases as production stream comes online. Ultimately, flow from well is primarily hydrocarbons (King, 2012).

Fractures in oil and gas bearing rocks will extend along the path of least resistance. In general, the rock will have three principal stresses acting at any point i.e. a vertical stress due to overburden of overlying strata and two horizontal stresses from front to back and side to side. Pushing back on the least of these three stresses by fluid pressure creates fracture. Fractures will extend if the pressure within them is maintained and additional fluid is injected. In general, fractures will extend in a vertical direction until a more ductile rock formation is encountered. These ductile formations restraint and cause the remaining fracture to grow horizontally within brittle formations (CSUR, 2014).

Microseismicity typically accompanies the brittle failure within the reservoir due to hydraulic fracturing processes. The recording of microseismicity is important as it can provide valuable insight into the fracturing process within the reservoir (Akram, 2014 and the references therein).

Along with hydraulic fracturing, horizontal drilling has greatly increased the capability to recover oil and natural gas from low permeability geologic plays. Practical application of horizontal drilling goes back to 1980s. Since then the advancement of downhole drilling technology and supporting equipment has enabled drilling into more complex plays. The purpose of horizontal drilling is to increase contact between reservoir and wellbore. Usually a well is drilled vertically up to the predetermined depth above the top of tight reservoir. The well is then kicked off to a sharp angle until it meets the reservoir interval in the horizontal plane by using advanced techniques i.e. rotary-steerable bits, geo-steering and logging while drilling (LWD). Once the borehole is horizontal to reservoir, it is drilled to certain extent as per drilling and regulatory plans (Giger, 1984).

1.3 Microseismic monitoring

Microseismic monitoring is an effective technique to image fracturing. At this point in time, microseismic monitoring is one of the only techniques that can physically image the subsurface geometry of stimulated fractures. Maxwell (2014) noted that microseismic monitoring involves passive seismic recording of microearthquakes or acoustic emissions. Microseismic events are "associated with naturally occurring or artificially induced fracture movements". Microseismic events are usually < 0 magnitude and very hard to detect in some cases.

The development of microseismic monitoring dates back to 1970s as a technique to monitor enhanced geothermal systems. Fenton Hill New Mexico hot dry rock (HDR) experiment is the earliest example of downhole microseismic monitoring (Aki et al., 1982). Many experiments of microseismic monitoring and imaging were performed during 1980s and 1990s. A series of experiments were performed at M-site in Piceance Basin, Colorado to validate microseismic images of hydraulic fractures by drilling through microseismic cloud and identifying fractures in recovered core (Maxwell, 2014). The encouraging results of these experiments led to an extensive study in

Cotton Valley fields of East Texas (Walker, 1997). A dramatic transformation occurred in commercial microseismic monitoring after Barnett Shale imaging (2000-2001) followed by Cotton Valley sands experiments (Maxwell et al., 2002).

1.3.1 Data acquisition

Microseismic data can be acquired from downhole, surface or near-surface monitoring arrays. Geophones or other type of sensors are deployed permanently or temporarily during continuous passive seismic monitoring. Some monitoring is permanently in place for the whole life of field; however, most monitoring is only for the duration of the hydraulic fracture treatment (Warpinski, 2009).

Surface and borehole arrays have advantages and disadvantages for microseismic acquisition. The advantages of surface arrays are the ability to deploy large number of geophones at the ground surface or at shallow depth. There is a much larger solid angle of acquisition than downhole array. This results in improved source position accuracy (Eaton and Forouhideh, 2011). The main challenge in surface monitoring is reduced signal amplitude, coupled with increased noise levels. The detected microseismicity at surface is characterized by a lower signal to noise ratio than data recorded in downhole environment (Eisner et al., 2011).

Acquiring downhole microseismic data needs extra efforts as it requires access to an observation well to install a geophone string. Often it happens that there is no observation well available in field near treatment well or it may happen that a production tubing needs to be pulled out of hole to use this as observation well, which may cause extra associated cost and production losses (Maxwell, 2014).

1.3.2 Data processing

Microseismic processing involves the determination of microseismic source parameters (location, magnitude) from signals that are measured during hydraulic fracturing. Event locations are used to infer hydraulic fracture geometry in final stages (Pike, 2014).

The generalized microseismic processing workflow can be summarized as follows:

- Geometry definition and sensor orientation
- Velocity model building and calibration
- Microseismic event detection
- Event hypocentre location
- Event attribute computation
- Acquisition and processing quality control (QC)

The first step in a processing sequence is to set up the acquisition survey geometry. Much care is required to convert survey coordinates to local coordinates to avoid any geometry error. A controlled perforation shot or vibrator at surface is used to obtain the orientation of receivers in a borehole (Pike, 2014). During polarization analysis, direction of the incoming wavefield is determined on each receiver level and P-wave pulse is identified in the orientation signal. This can be facilitated by plotting hodograms of the relative signal amplitude on the horizontal components (Maxwell, 2014).

Determination of velocity structure is a critical element in the microseismic processing workflow. Even with optimal data acquisition techniques, an inappropriate velocity model can result in substantial misplacement of microseisms data by 10’s of meters. Usually, the primary source for extracting velocity information is a dipole-sonic log, which enables both compressional and shear wave velocities to be obtained with high resolution. Velocity models can be constructed from various other sources including sonic logs, VSPs, crosswell or 3D seismic tomography. Log derived velocities represent vertical velocities along a segment of borehole. These velocities are generally not correct for microseismic analysis. Microseismic analysis for borehole data requires horizontal velocities, which can be 10-20% different from log-derived velocities (Warpinski, 2009). Corrections need to be applied to balance the vertical log-derived velocities to horizontal formation velocities for use in microseismic event location. Once the velocity model is obtained, P- and S- arrivals are picked and a forward modeling technique is used to calculate the travel times across a grid and position the events (Warpinski, 2009 and Pike, 2014).

The next step in microseismic processing is to detect potential microseismic events. The easiest method of event detection is based on detecting signal amplitude above a certain threshold level, calculated for each component for each receiver (Eaton, 2013). Alternatively, a short term/long term average (STA/LTA) ratio method can also be used (Akram et al., 2013). The detected events should be verified to ensure that they are actual microseismic events and not noise.

Hypocentre locations of microseismic events are a prime source attribute and the primary focus of processing. Hypocentre locations can be estimated by single 3C receiver, time difference (t_s - t_p) together with P-wave hodogram analysis. On the other hand, S-wave hodogram can be used to constrain the raypath orthogonal to the observed S-wave polarization (Maxwell, 2014). The direction is determined by analyzing the polarization characteristic of P- and S-waves. P-wave particle motion points back to the source, while S-waves will have orthogonal polarization (Warpinski, 2009). The final processing step involves determination of event characteristics and attributes and acquisition/processing QC.

1.4 Seismic attributes

Liner et al., (2004) defines seismic attributes as specific measures of geometric, kinematic, dynamic, or statistical features derived from seismic data. In a general sense, a seismic attribute includes all parameters derived from seismic data. Thus interval velocity, pore pressure, acoustic impedance, reflector terminations, complex trace attributes and amplitude variations with offset are considered attributes (Chopra and Marfurt, 2005).

Seismic attribute analysis originated in the 1930s when geophysicists started to pick traveltimes of reflections on field records. The advancement of computer technology in 1960s helped seismic attributes to develop further. For example digital recording in the 1960s brought some improvements in measuring seismic amplitudes and revealed correlations between strong amplitudes and hydrocarbon pore fluids i.e. bright spots. In the 1970s, the introduction of color printers enabled explorationists to overlay color display of reflection strength, frequency, phase and interval velocity on black and white seismic records. Interpretation workstation technology developed in the early 1980s was a major development that provided interpreters with the ability to manipulate color and scale and to integrate seismic traces with well data. In the last decade, robust progression in technology has made it possible for interpreters to integrate large volumes of data, calculating various attributes and getting reservoir and engineering information from seismic data (Chopra and Marfurt, 2005).

1.4.1 Classification

Attributes are generally classified based on the information that can be obtained from them. Over the last three decades the number of attributes has increased in terms of variety and usage. To better understand their application in geoscience, a number of authors have classified attributes into different categories. Composite attributes documented in the literature are constructed from the sum, products or combination of fundamental attributes. Some major classifications are described below.

Taner et al., (1994) divided attributes into two general categories: physical and geometrical. Physical attributes relate to physical parameters and thus lithology. These include amplitude, frequency and phase. Geometrical attributes are used to enhance the visibility of geometrical characteristics of seismic data, which includes azimuth, dip and continuity.

Brown (2004) classified attributes on the basis of time, frequency, amplitude and attenuation, which can be further subdivided into post-stack and pre-stack attributes. While post-stack subclassification can be further divided into horizon based or window based attributes. As a broad generalization, time-derived attributes provide information about structure while amplitude driven attributes provide stratigraphic information. Frequency and attenuation derived attributes are not well understood and are not widely used, but they can provide some additional information about reservoirs (Chopra and Marfurt, 2005).

Chen and Sidney (1997) proposed another way of classifying attributes based on wave kinematics/dynamics and reservoir features. Attributes based on wave kinematics/dynamics include amplitude, waveshape, frequency, attenuation, phase, correlation, and energy. On the other hand seismic attributes based on reservoir features are bright and dim spots, unconformity and faults, oil and gas bearing, thin layer reservoir, stratigraphic discontinuity, structural discontinuity, lithological pinchout and clastic – limestone differentiation.

Barnes (1997) developed another classification based on complex-trace attributes depending on different attributes and seismic data. This classification has helped in the development of multi-attribute analysis to define subsurface complexity more sophistically.

Another classification of attributes is described by Liner et al., (2004). This classification scheme provides a measure of geometric, kinematic, dynamic, or statistical features derived from seismic data. Attributes in this classification include reflector amplitude, reflector time, reflector dip and azimuth, complex amplitude and frequency, generalized Hilbert attributes, illumination, edge detection, coherence, AVO and spectral decomposition.

1.4.2 Main attributes

The analysis of seismic attributes permits us to identify key structural and petrophysical properties of the subsurface strata, which may be below the resolution of typical seismic amplitude data. Seismic attributes are widely used in oil and gas industry to identify lateral changes in the dip direction of horizons, fracture network, areas of high porosity and permeability, continuity in reflections, stratigraphic pinch outs, and many other features of interest which can be used in exploration and development of oil & gas field.

This study focuses on the following attributes:

- Coherence / Similarity
- Curvature
- Shape index

1.4.2.1 Coherence

Analysis of geometrical attributes began with examining coherence of the waveforms. Coherence is defined as the measure of similarity between waveforms or traces (Chopra and Marfurt, 2007) and measures how similar one trace or group of traces is with respect to surrounding traces.

Areas of high coherence shows continuous reflections while areas of low coherence often appear as discontinuous reflections, which may be indicative of faults and fractures. An example of coherent and incoherent event is illustrated in Figure 1.2. A coherent event is shown in figure 1.2a, with flat, laterally stable waveforms. Figure 1.2b shows a variant or incoherent event with laterally variable waveform. Figure 1.3a shows lateral changes as seen on seismic section, and Figure 1.3b is the corresponding response as seen on coherence slice, where lateral changes show up as low-coherence features (Chopra and Marfurt, 2007).

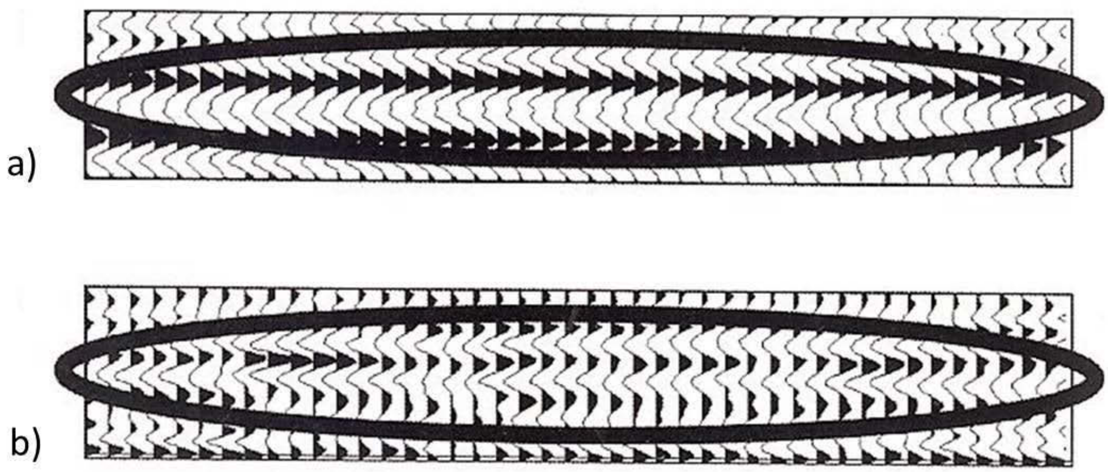

Figure 1.2: Examples of lateral variation in seismic waveforms: (a) flat. Laterally coherent waveform, (b) laterally variable, incoherent waveform (from Chopra and Marfurt, 2007).

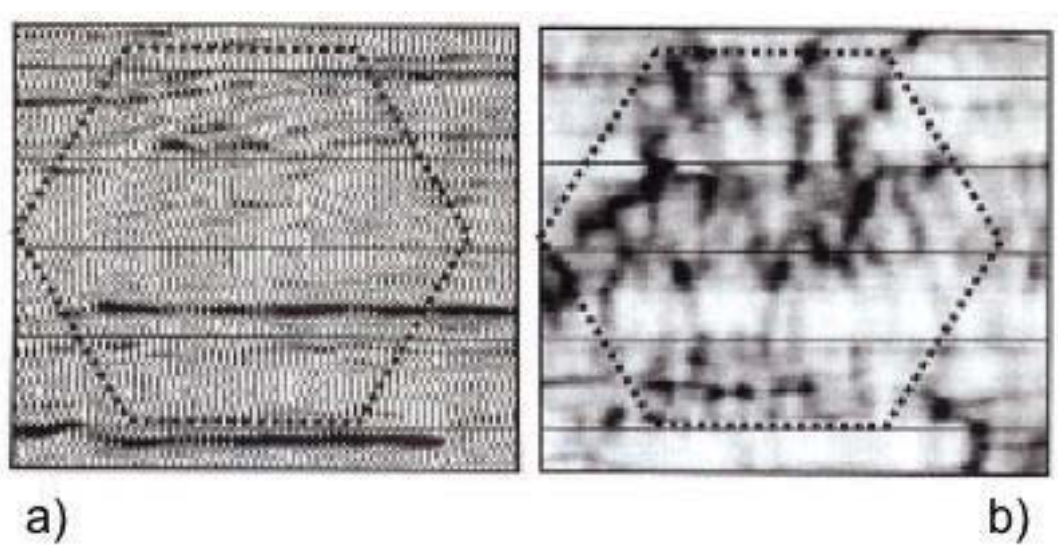

Figure 1.3: a) Lateral variations as seen on seismic data volume, b) Correspondent coherence slice (from Chopra and Marfurt, 2007).

1.4.2.2 Curvature

Chopra and Marfurt (2007) define curvature as a three-dimensional property of a quadratic surface that quantifies the degree to which the surface deviates from being planar. Curvature attributes are the 2nd order derivative of the structural component of seismic time or depth of reflection event (Chopra and Marfurt, 2012).

Surface seismic analysis normally does not map fractures and small-scale features, but it can map faults, folds and flexures. On the other hand curvature attribute analysis of surfaces can depict small-scale features that are associated with deposition and small-scale faults. Geometric curvature attributes computed from 3D surface seismic data give an overall picture of subsurface in predicting fractures. Fracture projections can be validated using formation images, tracer data, production logs and in our case through microseismic reactivation of paleo-zones of weakness (Chirinos, 2010).

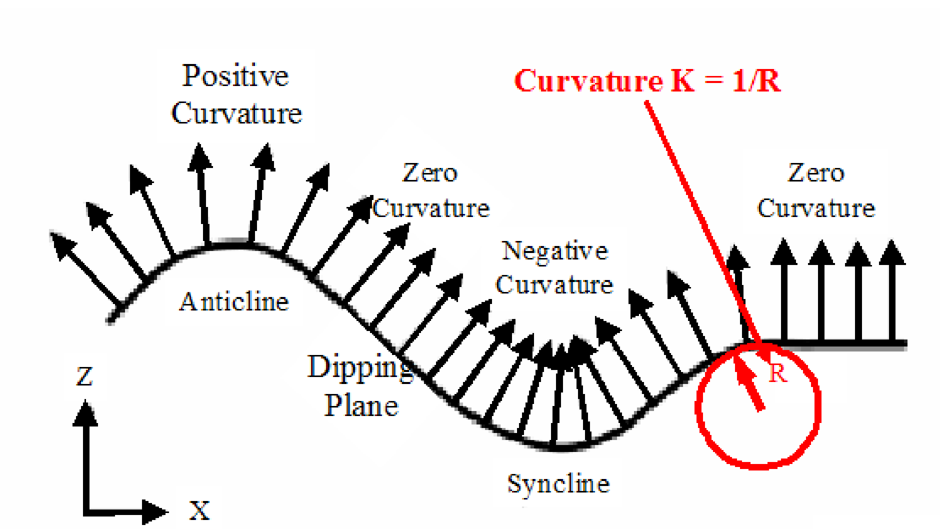

Figure 1.4: Two-dimensional curvature, synclinal features showing negative curvature, anticlinal features show positive curvature, while planar feature show zero curvature (from Roberts, 2001).

Roberts (2001) explained curvature of surface at any point as the inverse of the radius of a circle that touches tangentially a given curve, as shown in Figure 1.4. Curvature can be computed at each individual point on a gridded surface by fitting a quadratic surface to the surface seismic data and using the coefficients of quadratic equation. As an unlimited number of circles in normal planes of different azimuth may be tangent to the surface at any point, the circle with the minimum radius is defined as maximum curvature (k_{max}) and the circle which is perpendicular to the first circle of maximum curvature is defined as minimum curvature (k_{min}) and always has a radius greater than or equal to the maximum curvature. Interpreters usually prefer to use most positive principal curvature (k_1 or k_{pos}) and most negative principal curvature (k_2 or k_{neg}) (Chirinos, 2010).

To define curvature attribute in relation to subsurface features, 3D quadratic shapes can express more efficiently as a function of k_1 and k_2. Those six quadratic shapes are the plane, bowl, saddle, ridge, valley and dome. If both k_1 and k_2 are less than zero, quadratic shape is a bowl and if both are greater than zero, shape is a dome and if both k_1 and k_2 are equal to zero, it is a plane. Figure 1.5 describes different shapes resulting from different k_1 and k_2 values.

The curvature attributes can image faults and fractures using surface seismic volume. It is well known that microseismicity tends to occur within pre-existing faults and fractures. Applying curvature attributes to our study area, can help identify microseismic activity zones and can link surface seismic with microseismic.

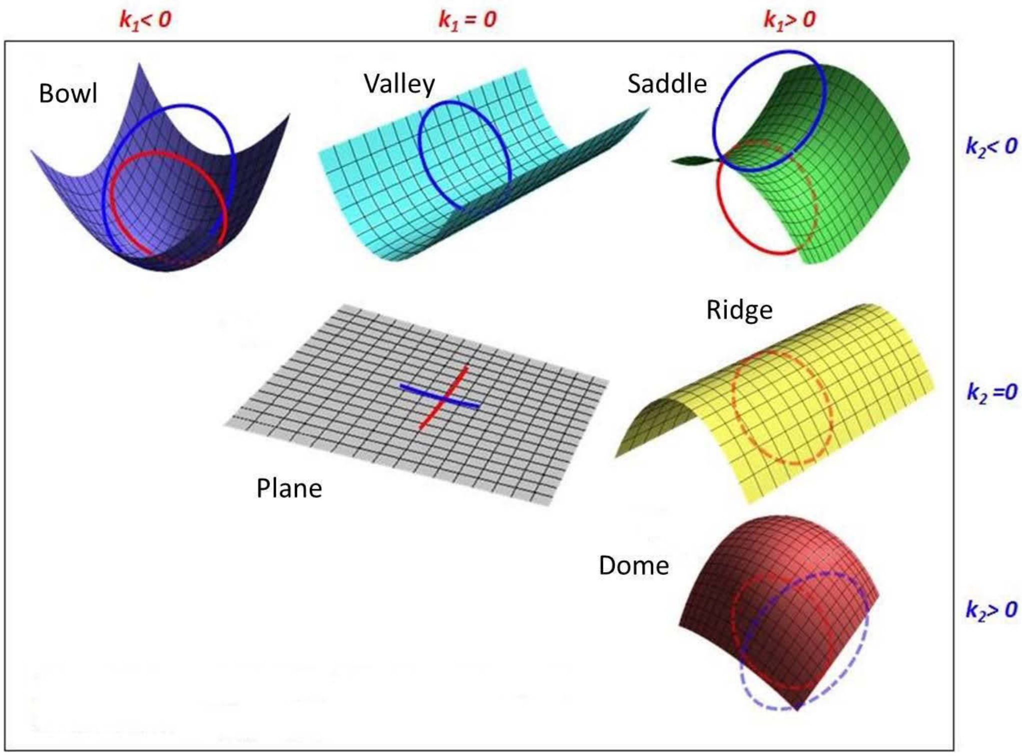

Figure 1.5: The definition of three-dimensional quadratic shapes expressed as most-positive (k_1), and most-negative (k_2), principal curvatures (modified from Mai, 2010).

1.4.2.3 Shape index

Chopra and Marfurt (2007) define shape index as:

$$s = \frac{2}{\pi}\tan^{-1}\left[\frac{k_2 + k_1}{k_2 - k_1}\right] \qquad (1.1)$$

This attribute shows the morphological structure of the mapped surface. The shape index of the dome is 1, 0.5 for the antiform, 0 for the saddle, -0.5 for the valley, and its value is -1 for the bowl.

1.5 Geology of the study area

The study area is the Hoadley field in south-central Alberta, Canada, which is a giant gas-condensate field that was discovered in 1977. The part of the Alberta foredeep basin is bounded on the east by the Canadian Shield, on the west by Rocky Mountains disturbed belt, on the north by Peace River Arch and on the south by the SweetGrass Arch (Chiang 1984) as shown in Figure 1.6. The field is hosted by the Glauconitic member of the Lower Cretaceous Upper Mannville Group, a lithologically diverse unit derived from the adjacent Cordillera.

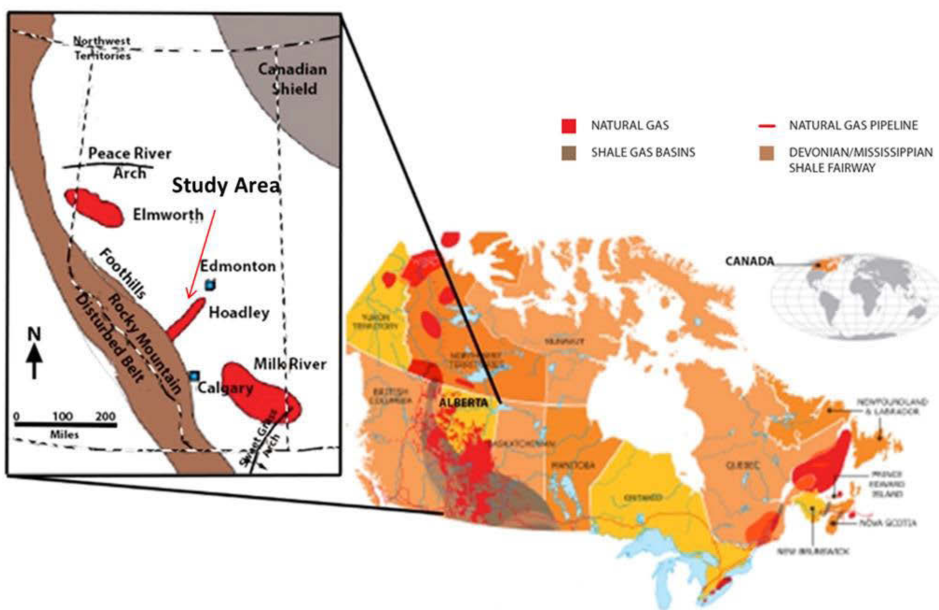

Figure 1.6: Location map showing Hoadley barrier bar and surrounding structures in the study area, Alberta foredeep basin in south central Alberta, Canada. (modified from Surdam, 1997 and history.alberta.ca).

The Glauconitic sandstone member contains shallow marine sandstone deposits interpreted to have formed as an extensive barrier bar complex, extending SW-NE for approximately 210 km along strike. The barrier bar complex is more than 25km wide and covers an area of ~4000 km^2. It marks the northern limit of continental to marginal marine depositional environment (Hayes et al., 1994). Modern examples of this type of depositional environment include Galveston Island (Texas gulf coast) and north shore of Prince Edward Island (Reynolds et al., 2012).

The lithology of the Hoadley shoreface complex indicates coarsening upward sequence, varying from porous sand facies to interbar lagoon and tidal-channel facies (Newbert et al., 1987). The barrier bar system contains progradational shallow marine sandstone bodies up to 32km in length, each of which hosts several distinct reservoirs (Newbert et al., 1987).

The Lower Cretaceous Glauconitic sandstone is overlain by continental sediments of the Blairmore formation, which consists of sandstone, siltstone and coalbeds, and is underlain by marginal marine limestone beds of the Ostracod zone (Figure 1.7). The Medicine River coal, which caps Glauconitic sands, acts as a seal and a regional marker. This coal is aerially extensive and varies in thickness from 0.5m to 5m (Reynolds et al., 2012).

Two distinct sands can be recognized within the shoreface complex, called lower or basal Glauconite and upper Glauconite by Chiang (1984). Basal Glauconitic sandstone is less permeable (~0.5mD) and is separated from upper permeable sandstone (~1-10mD) by an impermeable shaly siltstone referred to as the middle Glauconite. The reservoir is characterized by good quality sand bars separated by low permeability inter-bar sands. Consequently, there is potential of dual permeability behavior within the reservoir (Sorensen and Little, 1993). Measurement of regional stress orientation indicate that maximum principal stress is parallel to the main bar trends i.e. SW-NE (Churcher et al., 1996).

Glauconitic sandstone comprises a 7.5-24m thick pay zone. The middle and southwestern portion of the barrier bar is entirely saturated with gas and natural gas liquids, trapped laterally by impermeable shale and up-dip by shale-filled tidal channels (Chiang, 1984). The field is estimated to contain an ultimate potential recoverable reserve of 6 to 7 Tcf of gas and 350 to 400 million barrels (MMb) of associated natural gas liquids.

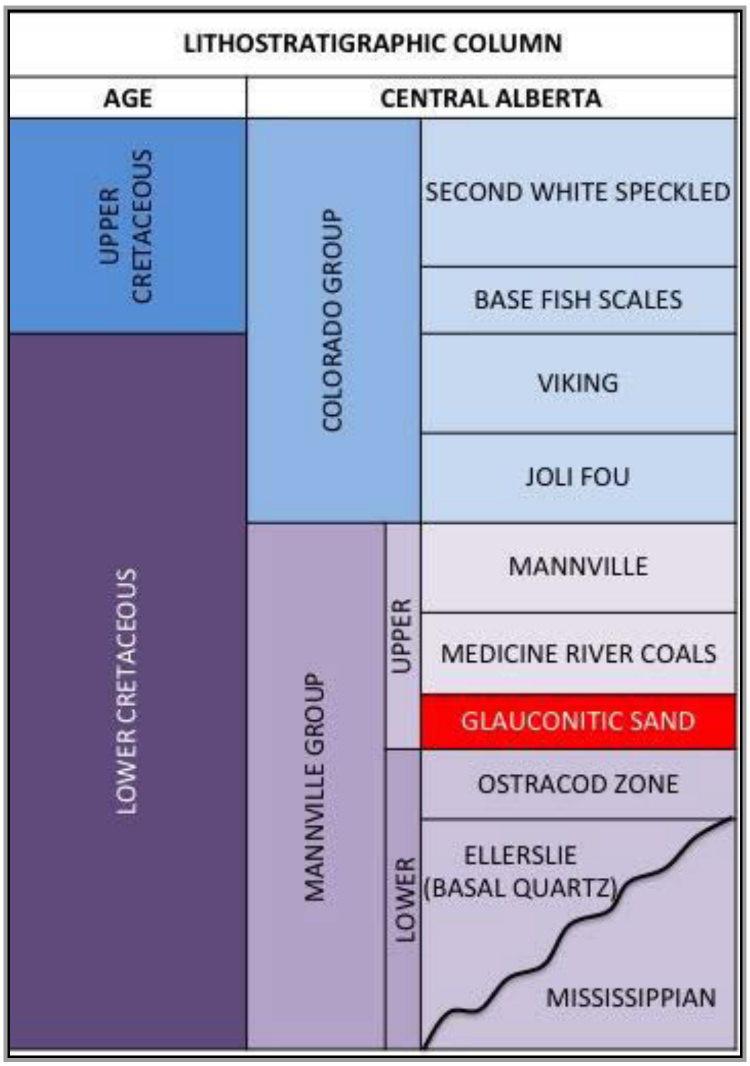

Figure 1.7: Chronostratigraphic column for the central Alberta basin. The reservoir is highlighted in red. (modified from Chiang 1984).

The Glauconitic sandstone's composition, low porosity and permeability require an integrated approach to delineate this tight sand reservoir. The following chapters will discuss the theory behind the methods used in this study.

1.6 Software used

The work shown in this thesis was accomplished by using the following software:

- Transform, a DrillngInfo software used for 3D seismic data interpretation, microseismic event analysis and seismic attribute calculations,
- Hampson-Russell STRATA, a CGG software used for model-based inversion of post-stack seismic data,
- Matlab, used for SRV and microseismic attribute calculation.

1.7 Thesis motivations

This thesis presents a general framework of several techniques and workflows developed in this study to improve the understanding of unconventional reservoirs using 3D reflection seismic and passive borehole seismic. The focus is on how surface seismic data can be integrated with microseismic data in a tight gas environment, in terms of understanding unconventional reservoirs. Integrating 3D seismic data with the microseismicity provides an integrated view of reservoir and is useful by (1) predicting microseismic response using surface seismic data, (2) validating reservoir heterogeneity inferred from microseismic, (3) mapping rock fabric, (4) delineating reservoir sweet spots, (5) optimizing well placement and (6) assisting in fracture engineering design.

The specific objectives of this thesis are as follows:

- develop workflow to integrate passive seismic with 3D reflection seismic;
- integrate microseismic into geologic framework;
- delineate distinct reservoir regions using recorded microseisms and attribute analysis;
- define characteristics of fracture-prone zones from mapped microseisms clusters for fracture network analysis;
- post-stack seismic inversion to extract rock property attributes.

1.8 Thesis contributions

Based on various technical analysis in this integrated study, e.g. attribute analysis, magnitude statistics, *b*-value variations, and stress orientations, I perform an integrated interpretation that links reservoir heterogeneity and rock fabric to compartments in the reservoir. These may in turn reflect variations in depositional environment and lithofacies. A novel approach *"microseismic facies analysis"* is introduced to delineate distinct reservoir regions.

The contributions of this thesis can be summarized as follows:

- introduced a novel approach "*microseismic facies analysis"*;
- developed workflow to correlate rock fabric with microseismicity;
- calculated, interpreted and correlated microseismic attributes with surface seismic attributes to understand reservoir geomechanics;
- generated post-stack seismic inversion volumes but could not calculate rock property attributes due to data limitation.

1.9 Organization of thesis

The thesis is organized as follows:

Chapter 2 discusses the available field data e.g. Hoadley Flowback microseismic experiment, microseismic data acquisition, processing and field layout, surface seismic data acquisition and processing summary and well log data.

Chapter 3 briefly describes 3D-seismic attribute calculation, correlation and analysis, and discusses the methodology and workflow for post-stack seismic data inversion.

Chapter 4 deals with integrated interpretation of microseismic and surface seismic data, including correlation of microseismic attributes with surface seismic attributes and results pertaining to microseismic facies. It introduces new methods for microseismic attribute calculations. The content in this chapter contains material from a poster presented at the 2014 EAGE meeting in Amsterdam (Rafiq and Eaton, 2014) as well as from a manuscript from a paper presented at the 2014 Discrete Fracture Network Engineering conference in Vancouver, BC, sponsored by ARMA (Eaton et al., 2014).

Chapter 5 concludes the thesis with a summary of analysis and results focusing on new approaches developed in this thesis, as well as future directions for research.

Chapter Two: **Field data**

The overall aim of this thesis is to integrate 3D surface seismic data with microseismicity. Integrated studies using advanced techniques help to unveil the potential of unconventional resources and aid in further development. This work describes a methodology for integrated interpretation of microseismicity recorded during the stimulation of two horizontal treatment wells and attributes from a coincident 3D surface seismic survey. Various types of field data that were used include 3D post stack seismic, microseismic events and well log data. A detailed overview of field data that was available for this study is discussed in this chapter.

2.1 Microseismic data

Microseismic data used in this project were acquired using downhole seismic monitoring of a multi-stage hydraulic fracture treatment in two horizontal wells in the Lower Cretaceous Glauconitic tight sand reservoir of the Mannville Group. As outlined below, this work was undertaken as a part of the Hoadley flowback microseismic experiment (HFME) by the Microseismic Industry Consortium. A total of 1660 microseismic events were recorded and located (Figure 2.2) during this 24-stage treatment, including 240 post pumping events after stimulation of well A and 19 post pumping events after stimulation of well B (Eaton et al., 2013a). Depth distribution and layering effect of microseismic events during hydraulic fracture treatment is shown in Figure 2.3.

Data were monitored and processed by Engineering Seismology Group (ESG). During processing, hypocentre locations were calculated using a velocity model that was generated from a sonic log from observation well and a dipole sonic log taken from an offset well. The velocity model was improved by control points taken from ball sleeve openings (Eaton et al., 2013a). The final velocity model is shown in Figure 2.4. The main information provided within the microseismic dataset includes the estimated XYZ coordinates, the local date/time of occurrence, and moment magnitude of microseismic events. A weighting factor indicating the reliability of microseismic moment magnitudes is also included.

2.1.1 Hoadley flowback microseismic experiment (HFME)

The Hoadley flowback microseismic experiment (HFME) was undertaken to acquire continuous downhole microseismic data during and after an open-hole multi-stage hydraulic fracture treatment of a tight sand reservoir in Hoadley field, Alberta (Eaton et al., 2014b). A continuous stream of data was acquired over the period of 295 days from September 12, 2012 to July 03, 2013. Twelve tri-axial downhole geophones were deployed to observe microseismicity during hydraulic fracture treatment, flowback and initial production periods. The main scientific objectives of this experiment are:

1. to undertake real-time microseismic monitoring of an open-hole multistage hydraulic fracture treatment in a tight sand reservoir i.e. Hoadley gas field;
2. to perform long-term monitoring of post-frac microseismicity during flow-back and production;
3. to develop a geomechanical model for flowback- and production-related microseismic activity;
4. to integrate interpretation of microseismic observations and seismic attributes derived from coincident 3D seismic survey.

This thesis covers the fourth objective of this experiment.

2.1.2 Operational setup

The downhole recording equipment consisted of a 12-sensor retrievable array of 15-Hz tri-axial geophones. The geophone pods were installed at the end of multi-conductor wireline, 2057m in length. Magnets were used to achieve coupling between pods and wellbore steel casing. Inter-pod spacing varied from 15.25m for the bottom 8 units to 30.5m for the top 4, having an array length of 229m as shown in Figure 2.4. The vertical observation well was situated between two horizontal treatment wells (Figure 2.1). The acquisition array was deployed in August 20-21, 2012 from 1605m to 1835m depth. Other elements of microseismic acquisition system included a mobile acquisition station that housed the digital acquisition system, a diesel generator that was upgraded to thermo-electric generator (TEG) and a spooler (Eaton et al., 2014).

2.1.3 Post-frac monitoring

The continuous data were harvested for a 10.5 - month period following the fracture treatment. The continuous time series were sampled with a sample rate of 4000 samples per second over a period of 295 days, and recorded on removable solid state drives (SSDs) in ringbuffer files. The data were harvested every 4-6 weeks on 6 SSDs and swapped from Paladin system. The data were archived and backed up on a processing/archival system at the University of Calgary, which yielded a total dataset of 12.6 TB. Events were detected and analyzed automatically and interactively using ESG's Hyperion Network Acquisition System (HNAS) software. The continuous stream of data was visually inspected, including triggered event files. The detected

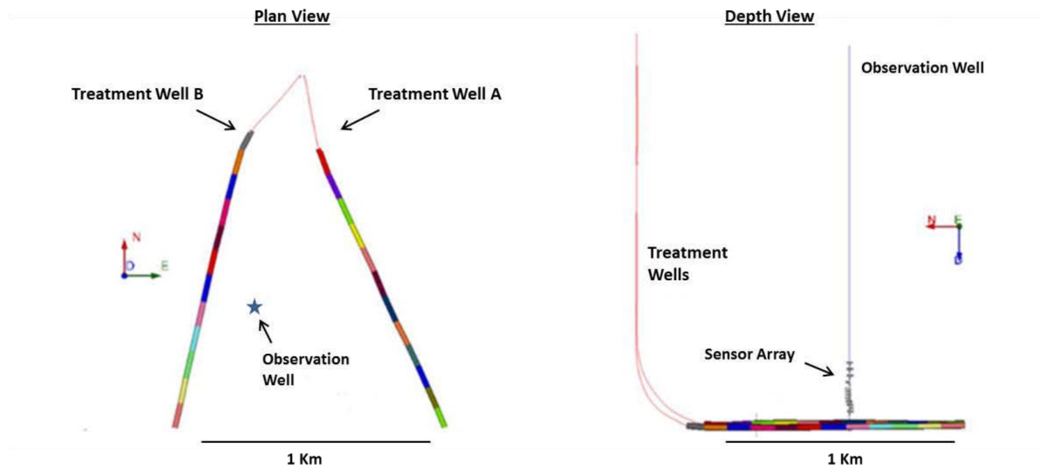

Figure 2.1: Layout of the treatment wells, observation well and sensor array. Left: plan view. Right: depth view. Sensor array is indicated by bars. Treatment stages are denoted by different colors along the horizontal treatment wells (modified from Eaton et al., 2014a).

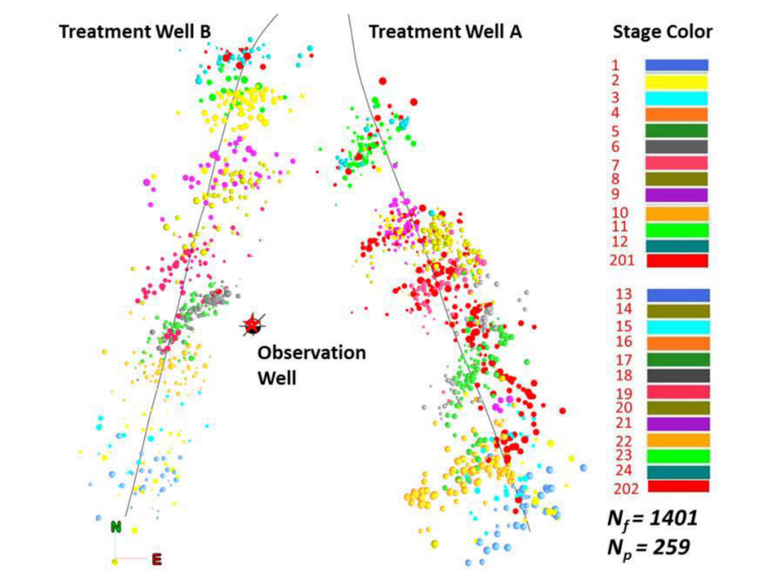

Figure 2.2: Distribution of 1660 microseismic (MS) events recorded during the 2-day hydraulic-fracture treatment program. Events shown in red are post-pumping. Nf and Np denote number of events recorded during, fracture treatment and post-pumping periods, respectively.

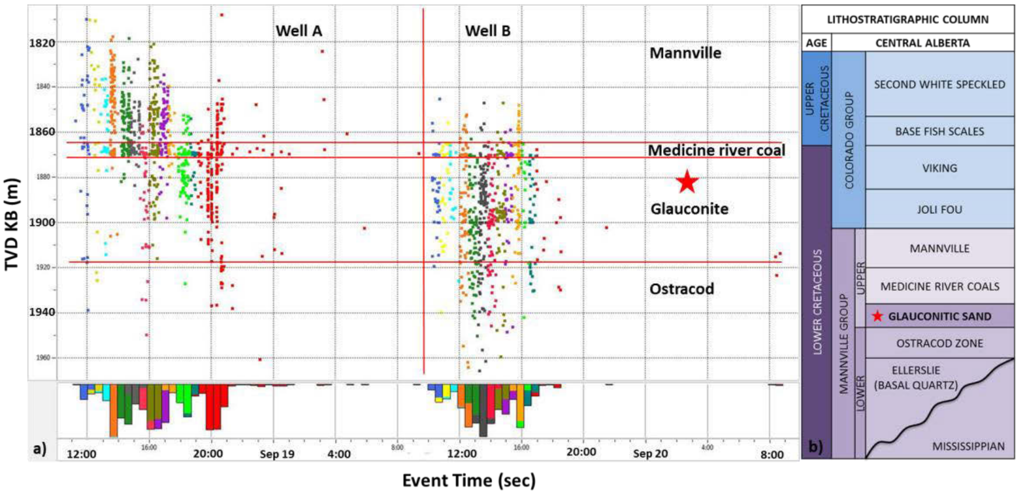

Figure 2.3: Distribution of microseismic events and layering. a) cross section showing depth distribution of microseismicity during treatment program, b) stratigraphic succession of the study area used to establish layering. Treatment zone is indicated by red star.

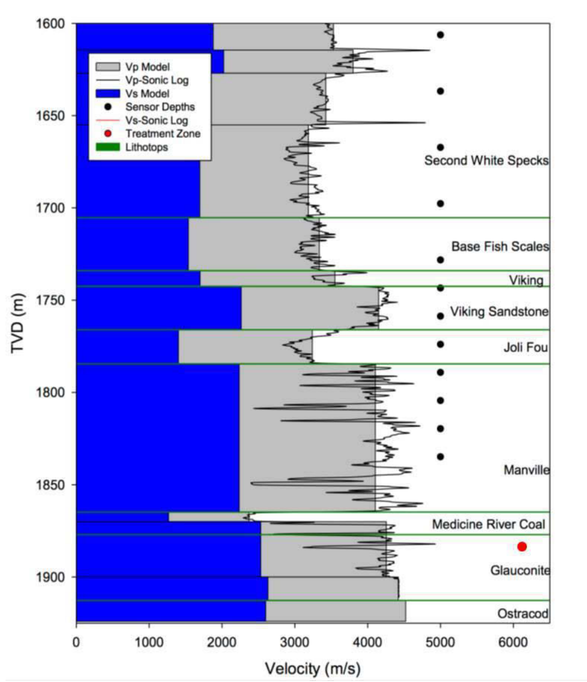

Figure 2.4: Velocity model used to calculate hypocentre locations. Geophone depths, indicated by the black dots, in the observation well. Also shown are formation boundaries in green and red dot indicates treatment zone.

events from the continuous microseismic data were classified into 1) microseismic events 2) long period, long duration signals 3) low frequency events 4) tube waves. Appendix A provides the detailed description of this classification scheme.

2.2 3D seismic data

In addition to microseismic data, this study makes use of 3D seismic data that were acquired by Arcis Seismic solutions. The 3D survey was recorded in January 2013, about 4 months after completion of hydraulic-fracture treatment program. The 3D seismic data were acquired in Ille Lake, located northwest of Red Deer in north-central Alberta, covering an area of 169.93 km^2 as shown in Figure 2.5. The seismic survey was acquired using 1.5 kg dynamite shots @ 9m depth, with 2016 receiver channels and 60m source and receiver intervals. Seismic acquisition survey parameters are summarized in Table 2.1. The seismic data were processed by Arcis Seismic Solutions. The processed data products used in this study consist of post-stack time migration (POSTM), with spectral whitening applied to enhance data resolution. Figure 2.6 summarizes the processing workflow applied on Hoadley seismic data as documented in EBCDIC header.

For this study, 14 km^2 out of 169.93 km^2 of 3D seismic data (full survey) in SEG-Y format were available for the Hoadley Gas field (Figure 2.5). The post stack data included:

- Post-stack time migrated (POSTM)
- Post-stack time migrated, with spectral whitening (POSTMw)

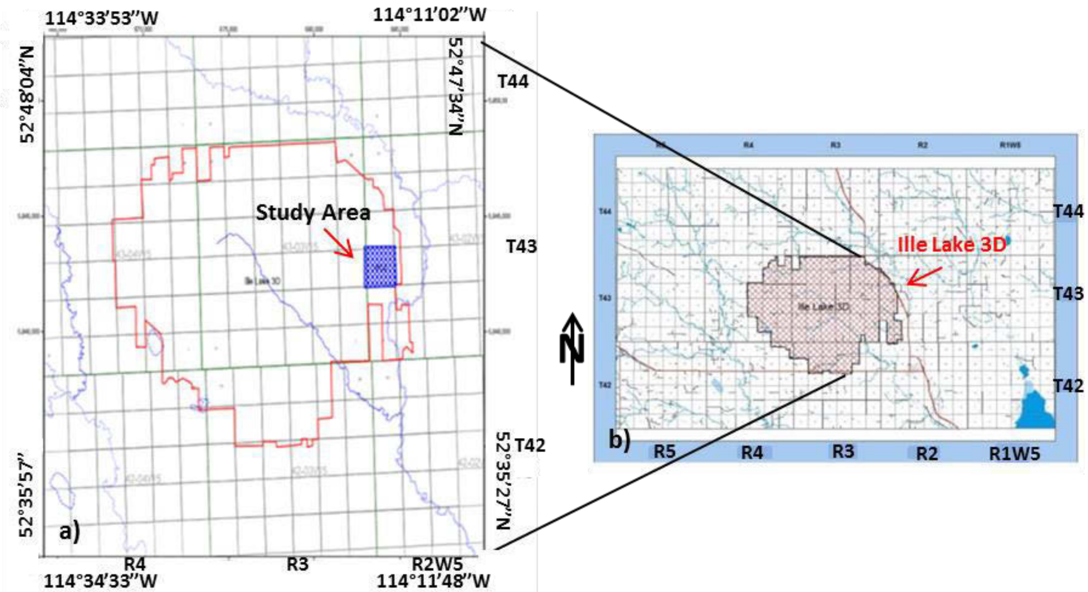

Figure 2.5: a) Zoomed out location map showing part of survey 14 km^2, provided for this study. Blue rectangle represents the part of survey provided, b) Ille Lake 3D seismic survey (169.93 km^2) location map.

Table 2.1: Ille Lake 3D seismic survey acquisition parameters.

Parameter	Value
Coverage	169.93 km^2
Source	Dynamite 1.5 kg @ 9m
Source Interval	60 m
Crossline Interval (Direction)	420 m (N-S)
Receiver Interval	60 m
Inline Interval (Direction)	300 m (W-E)
Patch Size	18 lines × 112 receiver groups (2016 channels)
Bin Size	30 m × 30 m
Sample Rate	1 ms
Record Length	5.0 s

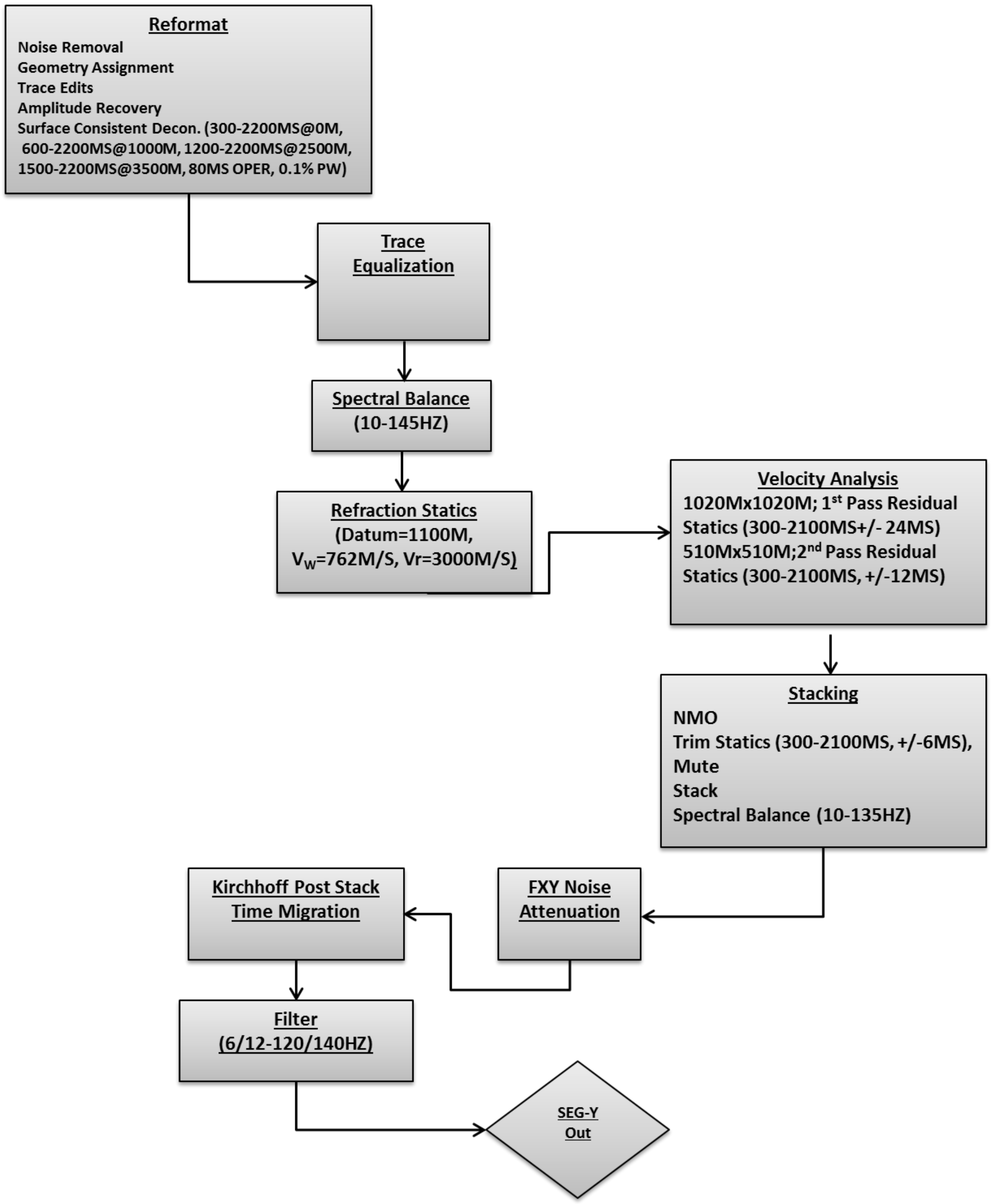

Figure 2.6: Seismic data processing workflow applied by Arcis Seismic Solutions (taken from EBCDIC header).

Both versions of post-stack seismic data were loaded into and QC'd in the Transform software, provided by DrillingInfo. The spectrally enhanced seismic data were selected for this study due to its superior data quality. Spectral whitening is usually applied on post-stack seismic data during processing, to enhance data quality.

It is well known that post-stacked seismic data can suffer from the acquisition footprint at shallow levels, which may mask the output response (Pelaez, 2012). Acquisition footprint is a linear spatial grid pattern seen on 3D seismic time or horizons slices, mirroring parts of acquisition geometry (Chopra and Larsen, 2000). It is therefore recommended to condition data for noise suppression and cancellation of any acquisition/processing footprint, before doing advanced interpretation (Chopra and Marfurt, 2008). For this purpose I applied FX-Decon (Chopra and Marfurt, 2007) and structure-oriented median filter (Chopra and Marfurt, 2008, 2012, and Transform software user guide, 2015) to suppress noise and to enhance lateral continuity. A detailed description of data conditioning is discussed in chapter 3.

I have interpreted ten horizons and computed corresponding attributes above and below the Glauconite reservoir zone, on the time domain seismic data and then converted horizons and attributes to the depth domain to enable correlation with microseismicity.

2.3 Well data

The available well data included well logs, well deviation survey, well locations, and formation tops in the wells. A full suite of well logs (except shear sonic log) were available for the observation well while a gamma ray (GR) log was also available for the treatment well B, in log ASCII standard (LAS) format. Figure 2.7 shows the available well logs displayed in Transform software.

The datum for the well data including deviation surveys, well tops and well logs are taken from Rotary Kelly bushing (RKB), which is 951.40m for the observation well. Since the well data was in depth domain and the surface seismic data was in time domain, a depth-to-time conversion was done using (sonic logs) well to seismic tie. Other uses of well to seismic tie include matching seismic with stratigraphy (horizon interpretation), checking and adjusting the phase of seismic data (zero phasing), and extracting wavelet for seismic inversion and modeling.

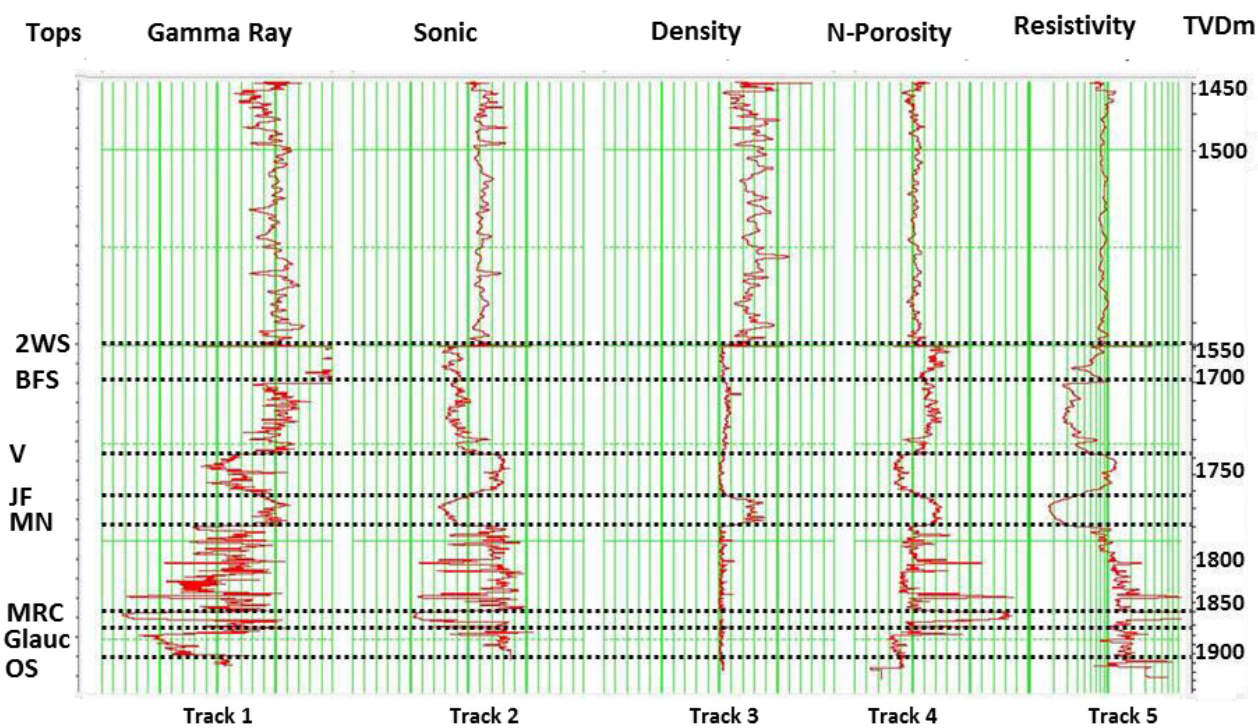

Figure 2.7: Formation tops with available well logs from the observation well. From left to right panel showing, gamma ray, sonic, density neutron porosity and resistivity logs. Abbreviations of Cretaceous formations are as follows: 2WS = Second White Specks; BFS = Base Fish Scales; V = Viking; JF = Joli Fou; MN = Mannville; MRC = Medicine river coal; Glauc = Glauconite; OS = Ostracod.

Chapter Three: **Post-stack seismic attributes and inversion**

Post-stack seismic attribute analysis and inversion is an integral part of this study. Attributes have long been used by interpreters to map subtle stratigraphic details and structural deformation that are not readily observable on seismic data (Chopra and Marfurt, 2007). I have computed numerous attributes including edge detector geometrical, stratigraphic and frequency-enhancing, volume and horizon attributes using post-stack time-migrated 3D seismic data. I converted attributes to the depth domain to enable correlation with microseismic events. During this process, I narrowed them down to the key interpretable attributes that show promising correlation with microseismic attributes, as discussed in chapter 4.

Post-stack seismic impedance inversion is a powerful tool to extract physical rock properties and to improve vertical seismic resolution (Latimer et al., 2000). It plays an important role in stratigraphic interpretation and reservoir characterization. Different methods are available to perform post-stack acoustic impedance inversion, depending upon the level of sophistication and data availability e.g. stochastic inversion, model-based inversion, recursive inversion, sparse-spike inversion and colored inversion, as discussed by Oldenburg et al., (1983), Russell, (1988), Haas and Dubrule (1994) and Chopra and Marfurt (2007).

In this study, I have computed the P-impedance volume from post-stack seismic data through model-based inversion. Inversion results and attributes are equally sensitive to input data quality; therefore input data are conditioned to reduce random noise and acquisition/processing footprint.

3.1 Data conditioning

The quality of inversion results and attribute images depends upon the input data. If the input data are masked with random or coherent noise, then the output can lead to a false interpretation. In particular, post-stacked seismic data can suffer from the acquisition footprint at shallow levels, which may mask attribute response but heals with depth (Pelaez, 2012). It is therefore recommended to condition the data, even if the noise and footprint cannot be totally eliminated (Chopra and Marfurt, 2008). For this purpose I have applied FX-Decon (Chopra and Marfurt, 2007) and structure-oriented median filter (Chopra and Marfurt, 2008, 2012, and Transform software user guide, 2015) to suppress noise and to enhance lateral continuity.

3.1.1 FX- deconvolution

FX deconvolution (FX-Decon) filter is applied to time migrated 3D-post stack data. It is a predictive deconvolution filter applied spatially across seismic spectral traces (FX=frequency, space), along constant time levels, to attenuate random noise and retain coherent seismic signal. FX-Decon is usually applied in areas of moderate to low geologic complexity (Transform software user guide, 2015), as was the case here. The seismic traces reconstructed from this filter are characterized by more coherent signal relative to random noise as shown in Figure 3.1b.

3.1.2 Structure oriented median filter

Structure Oriented Median (SOM) filter is applied to time-migrated data to remove acquisition/processing footprint patterns and to enhance lateral seismic continuity by preserving subtle geologic features (Transform software user guide, 2015). SOM is usually applied after

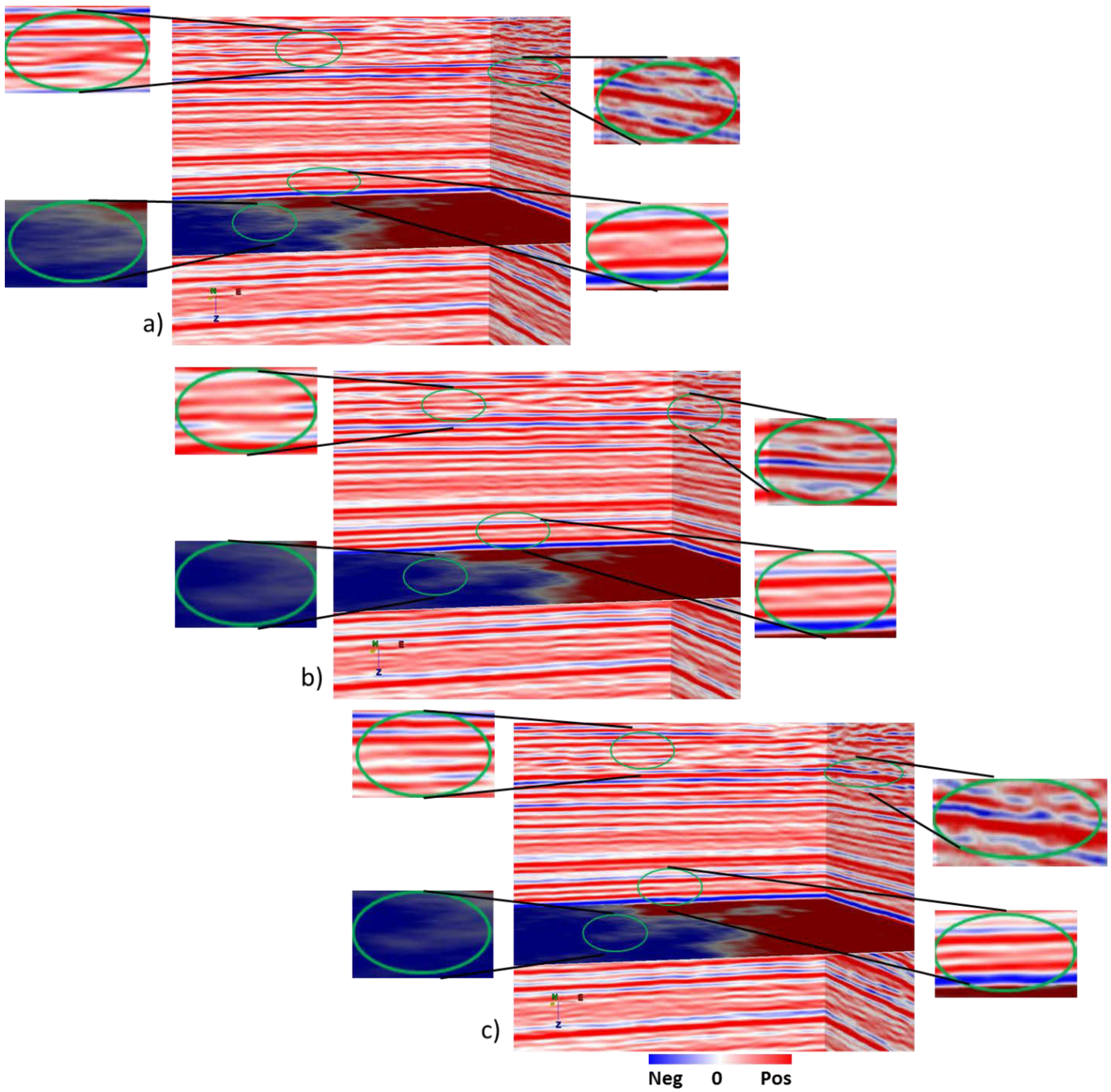

Figure 3.1: Segments of 3D-seismic depth volume from a) Input post-stack seismic amplitude data, b) data after FX-Decon filter applied to remove random noise, c) data passed through structural-oriented 3 x 3 median filter, applied to enhance lateral continuity. Notice the improvement in lateral continuity in the highlighted zoomed portions.

removing random background noise. Median values of multiple time samples are selected from adjacent traces in both inline and crossline direction. For optimal preservation of subtle geologic features, the actual spatial size of the median filter is dynamically adjusted from the specified values, based upon tests applied on data. The size of the median filter is adjusted carefully to optimize data quality without attenuation of true signals. I have used 3 x 3 values for the gentlest data filtering. A comparison of results is shown in Figure 3.1c.

3.2 Seismic attributes

Seismic attributes are defined as "specific measures of geometric, kinematic, dynamic, or statistical features derived from seismic data" (Liner et al., 2004). In a general sense, a seismic attribute may represent any parameter derived from seismic data. Thus interval velocity, pore pressure, acoustic impedance, reflector terminations, complex trace attributes and amplitude variations with offset (AVO) are all considered attributes (Chopra and Marfurt, 2005). For details on seismic attributes and their history, see chapter 1.

I have computed numerous volume and horizon attributes based on amplitude, velocity, time and frequency information from the input seismic data. Volumetric curvature, which belongs to the geometrical attribute class, is one of the many computed attributes and is useful in the prediction of fractures from surface seismic data (Chopra and Marfurt, 2007). A variety of curvature attributes such as the most positive curvature, the most negative curvature, mean curvature, root-mean square (rms) curvature and Gaussian curvature were computed. Other computed attributes include shape index, incoherence and thin-bed reflectivity etc. Based on the key criteria, which was to find attributes that are more representative of structural or stratigraphic features such as lineaments, fractures etc., I picked four key attributes from an extensive initial attribute set, comprising incoherence, shape index, the most-positive curvature (k_1) and the most-negative curvature (k_2). Incoherence results in a discontinuity attribute volume showing faults and other discontinuous features. The shape index shows the morphological structure of the mapped surface. The most-positive and most-negative curvatures provide useful information for the delineation of faults, fractures, flexures and folds (Chopra and Marfurt, 2007).

The use of multiple attributes is important, as one attribute may be sensitive to a specific type of geologic feature of interest, while a second attribute may be sensitive to another kind of feature. For example, some attributes are sensitive to anticlinal features i.e. most positive curvature attribute, while some are sensitive to synclinal features i.e. most negative curvature (Chopra and Marfurt, 2007). Therefore, I combined multiple attributes to enhance the contrast between the features of interest and their corresponding stratigraphic and structural details. Further, I have tested various visualization combination techniques and co-rendered various attributes. I found promising results from RGB and RGBGray scale display, as shown in Figure 3.2(f,g)-3.11(f,g).

3.2.1 Attribute analysis

To better understand reservoir characteristics, fracture network and microseismicity, I have interpreted ten horizons above and below the reservoir and computed corresponding attributes. Figure 3.2 to 3.11 shows depth slices of each attribute, including multi-attributes combined using Red-Green-Blue (RGB) and Red-Green-Blue-Gray (RGBGray) scales. Since the microseismic events are distributed in several zones above and below the Glauconite reservoir (Figure 4.2), the attribute analysis was performed for these zones to seek possible correlations. It is clear from the analysis that the major features imaged in the reservoir and below are most likely to be natural and not artifacts arising from the acquisition/processing footprint (Figure 3.2-3.3). However, it seems that there may be some acquisition/processing footprint or noise impacting the information in the attributes at the shallow level.

In the case of the RGB scale, red represents most-positive curvature, green represents most-negative curvature and blue represents incoherence attribute, whereas in the case of the RGBGray scale red is most-positive curvature, green is shape-index, blue most-negative curvature and gray represents incoherence attribute. This approach highlights finer structural details for interpretation of reservoir compartments. To better visualize and compare, I have arranged them in a way that each computed attribute for a single horizon displays in a single figure.

Depth horizon slices through three different attribute cubes (incoherence, most-positive curvature and most-negative curvature) exhibit a set of bar-like features that trend NE-SW and N-S, as shown in Figures 3.2-3.4. Two well-developed trends are sub-parallel to the regional depositional trend (part of Hoadley barrier-bar complex) and are interpreted as sandbar and interbar sands based on the correlation of curvature and shape index values with depositional environment as specified in Newbert et al., (1987). Another set of features is transverse to the depositional trend and is almost parallel to the sediment transport direction i.e. N-S. These lineations are similar in character to the inferred sandbars and are shorter. They terminate against NE-SW trending anomalies in various ways, as shown in Figures 3.2-3.4.

A north-ward shifting trend of anomalies appears to align approximately with N-S oriented lineaments while moving from deeper to shallower attributes, as shown in Figures 3.2-3.11. RGB and RGBGray scaled multi-attributes in Figure 3.5(f,g)-3.9(f,g) show a better view of NE-SW and N-S trending anomalies and reservoir compartments. Another north-ward shift trend of lineaments is observed on shallower depth slices as shown in Figure 3.10-3.11. The lineaments seen on these figures are aligned in NNW-SSE and N-S direction but do not exhibit any interpretable features.

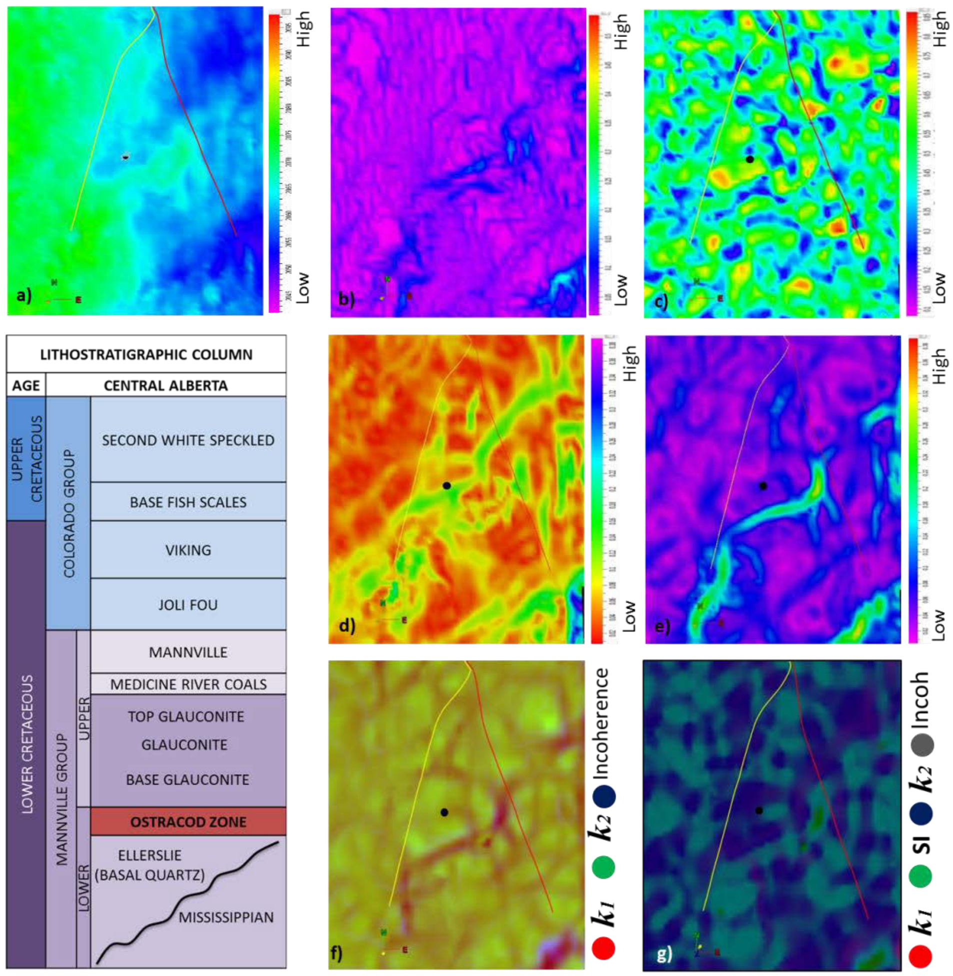

Figure 3.2: Depth slices at Ostracod horizon, showing the following attributes, a) amplitude, b) incoherence, c) shape index, d) most-positive curvature, (k_1), e) most-negative curvature, (k_2), f) most-positive curvature co-rendered with most negative curvature and incoherence on RGB scale (note how the display shows NE-SW trending lineaments and compartmentalization of the reservoir), g) most-positive curvature co-rendered with shape index, most-negative curvature and incoherence on RGBGray scale.

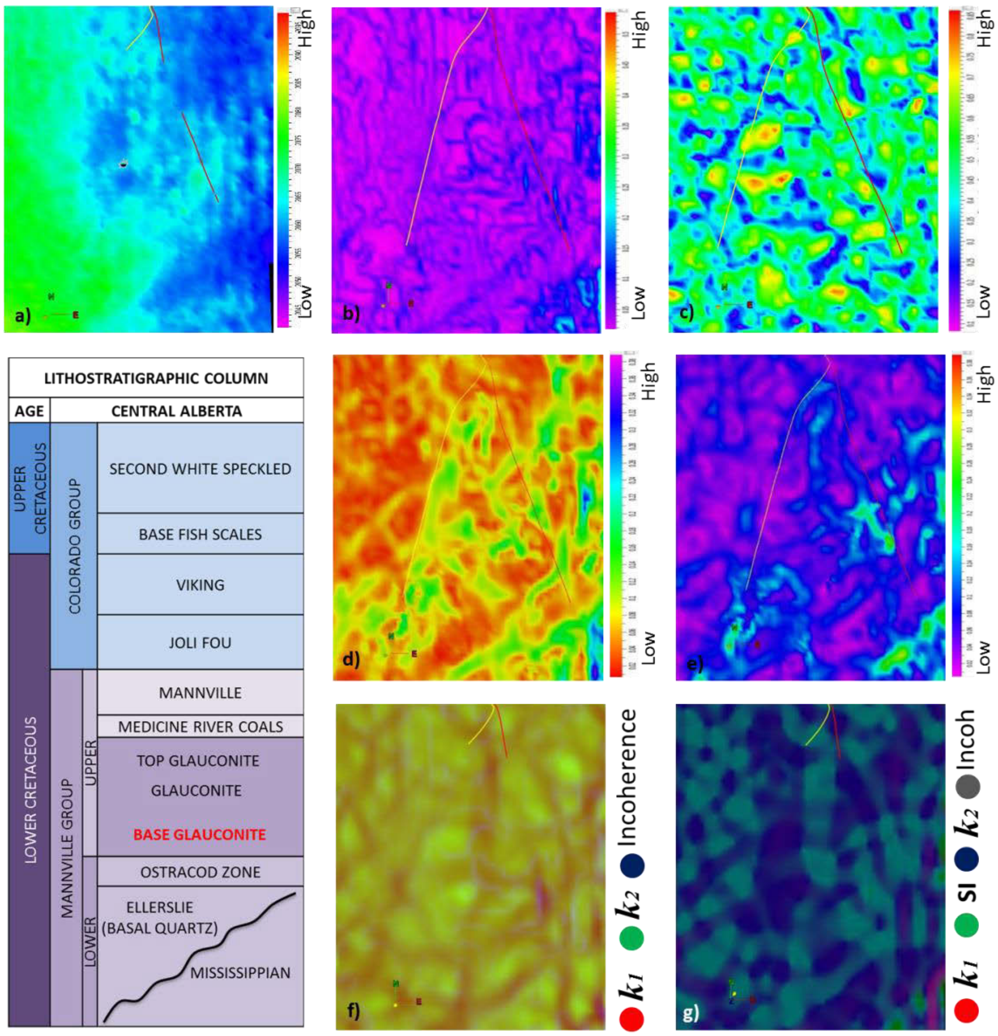

Figure 3.3: Depth horizon slices at Base Glauconite horizon, showing the following attributes, a) amplitude, b) incoherence (note the high amplitude and high incoherence anomaly trending NE-SW), c) shape index, d) most- positive curvature, (k_1), e) most-negative curvature, (k_2) (note NE-SW trend of curvature anomalies), f) most-positive curvature co-rendered with most negative curvature and incoherence on RGB scale (note how the display shows NE-SW trending lineaments and compartmentalization of the reservoir), g) most-positive curvature co-rendered with shape index, most-negative curvature and incoherence on RGBGray scale.

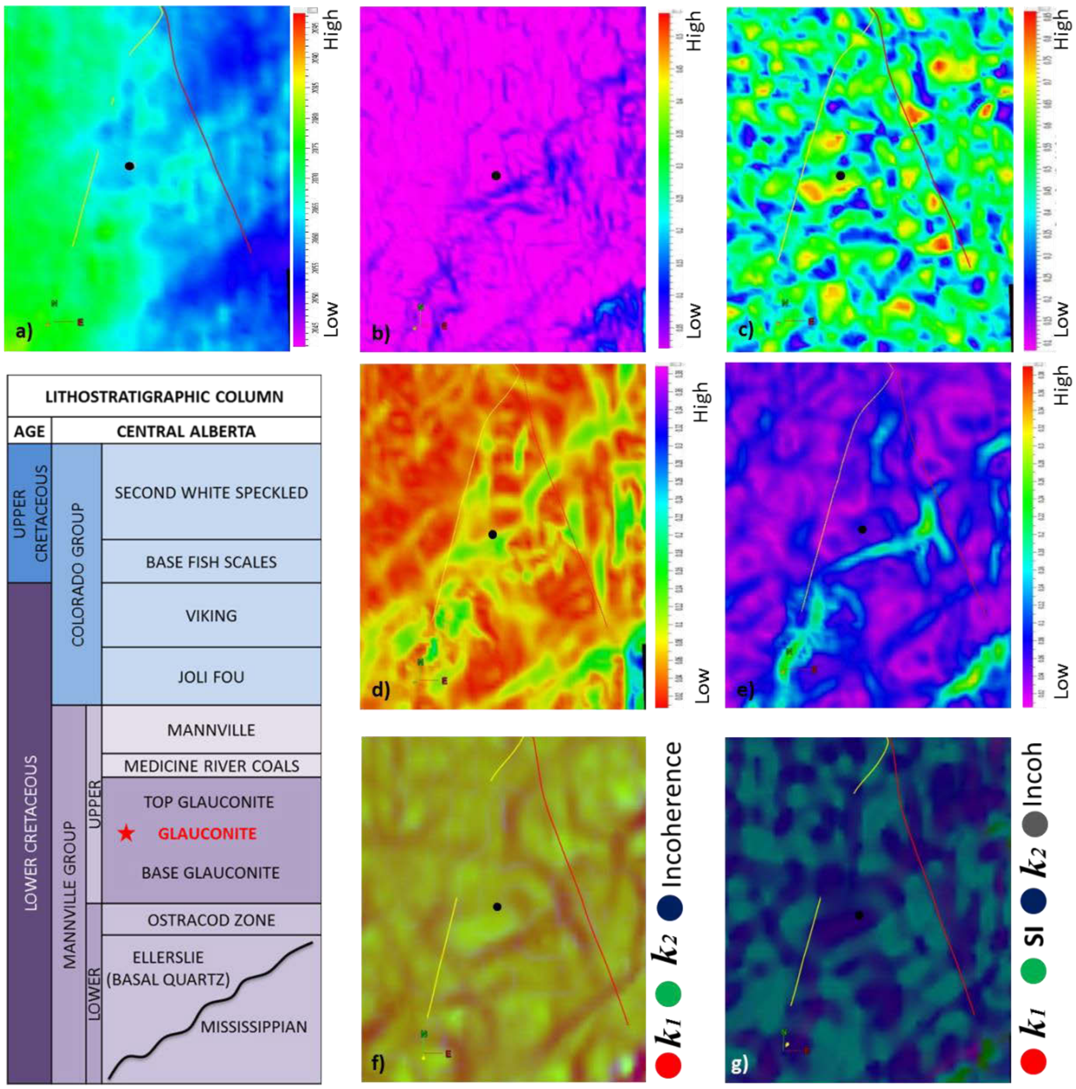

Figure 3.4: Depth horizon slices at Glauconite horizon showing the following attributes, a) amplitude, b) incoherence, c) shape index, d) most- positive curvature, (k_1), e) most-negative curvature, (k_2) (note NE-SW trend of curvature anomalies), f) most-positive curvature co-rendered with most negative curvature and incoherence on RGB scale (note how the display shows NE-SW trending lineaments and compartmentalization of the reservoir), g) most-positive curvature co-rendered with shape index, most-negative curvature and incoherence on RGBGray scale.

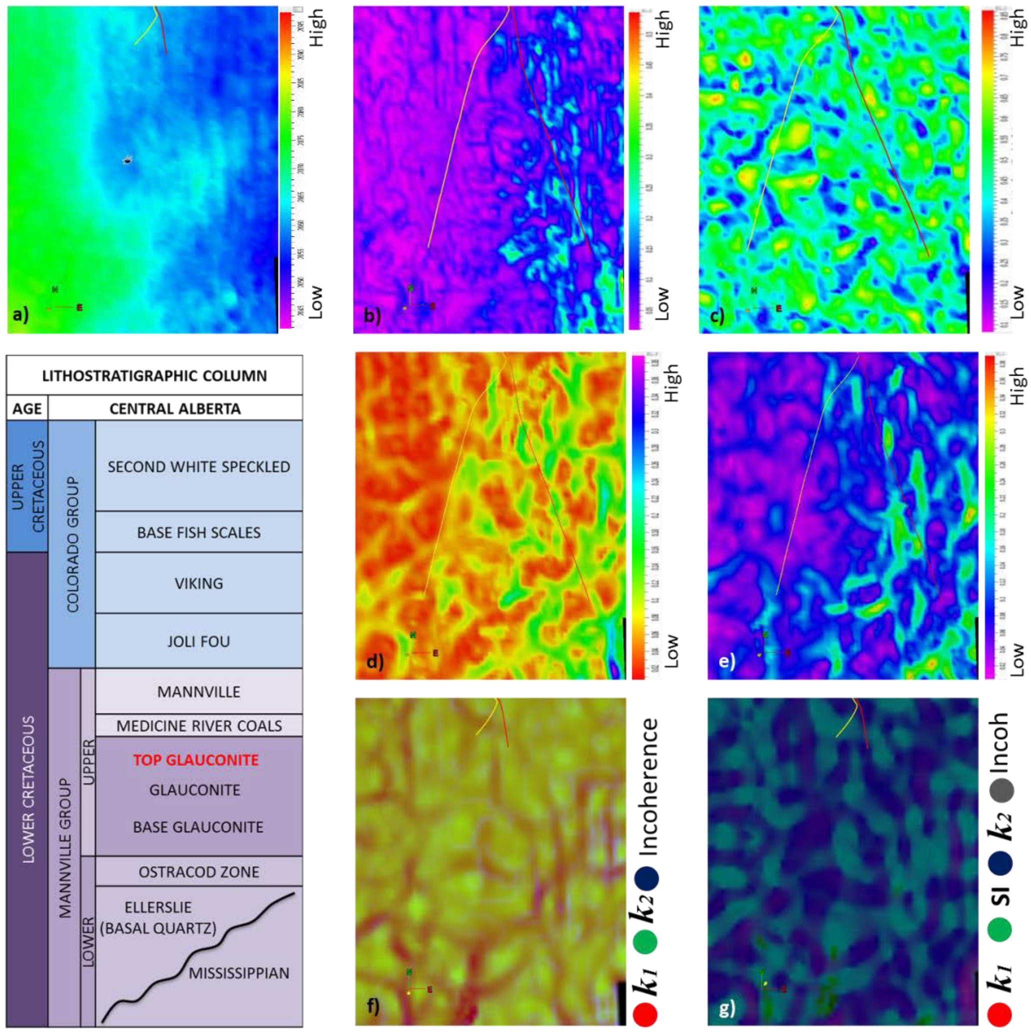

Figure 3.5: Depth horizon slices at Top Glauconite horizon, showing the following attributes, a) amplitude, b) incoherence (note the N-S trending features on amplitude and incoherence), c) shape index, d) most- positive curvature, (k_1), e) most-negative curvature, (k_2) (note the shift in trend of curvature anomalies ~N-S), f) most-positive curvature co-rendered with most negative curvature and incoherence on RGB scale (note how the display shows changing trend of lineaments and compartmentalization of the reservoir), g) most-positive curvature co-rendered with shape index, most-negative curvature and incoherence on RGBGray scale.

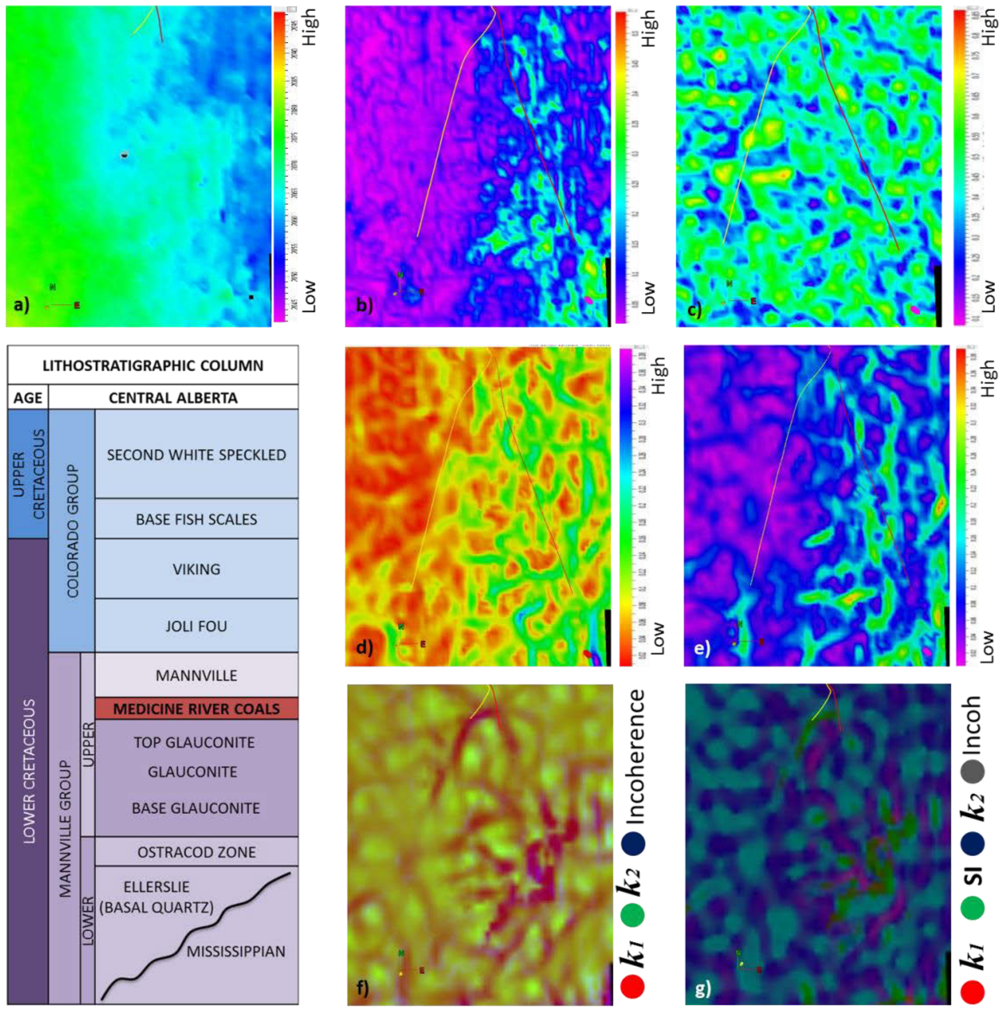

Figure 3.6: Depth horizon slices at Medicine River Coal horizon, showing the following attributes, a) amplitude, b) incoherence (note the N-S trending features on amplitude and incoherence), c) shape index, d) most- positive curvature, (k_1), e) most-negative curvature, (k_2) (note the shift in trend of curvature anomalies ~N-S), f) most-positive curvature co-rendered with most negative curvature and incoherence on RGB scale (note how the display shows changing trend of lineaments and compartmentalization of the reservoir), g) most-positive curvature co-rendered with shape index, most-negative curvature and incoherence on RGBGray scale.

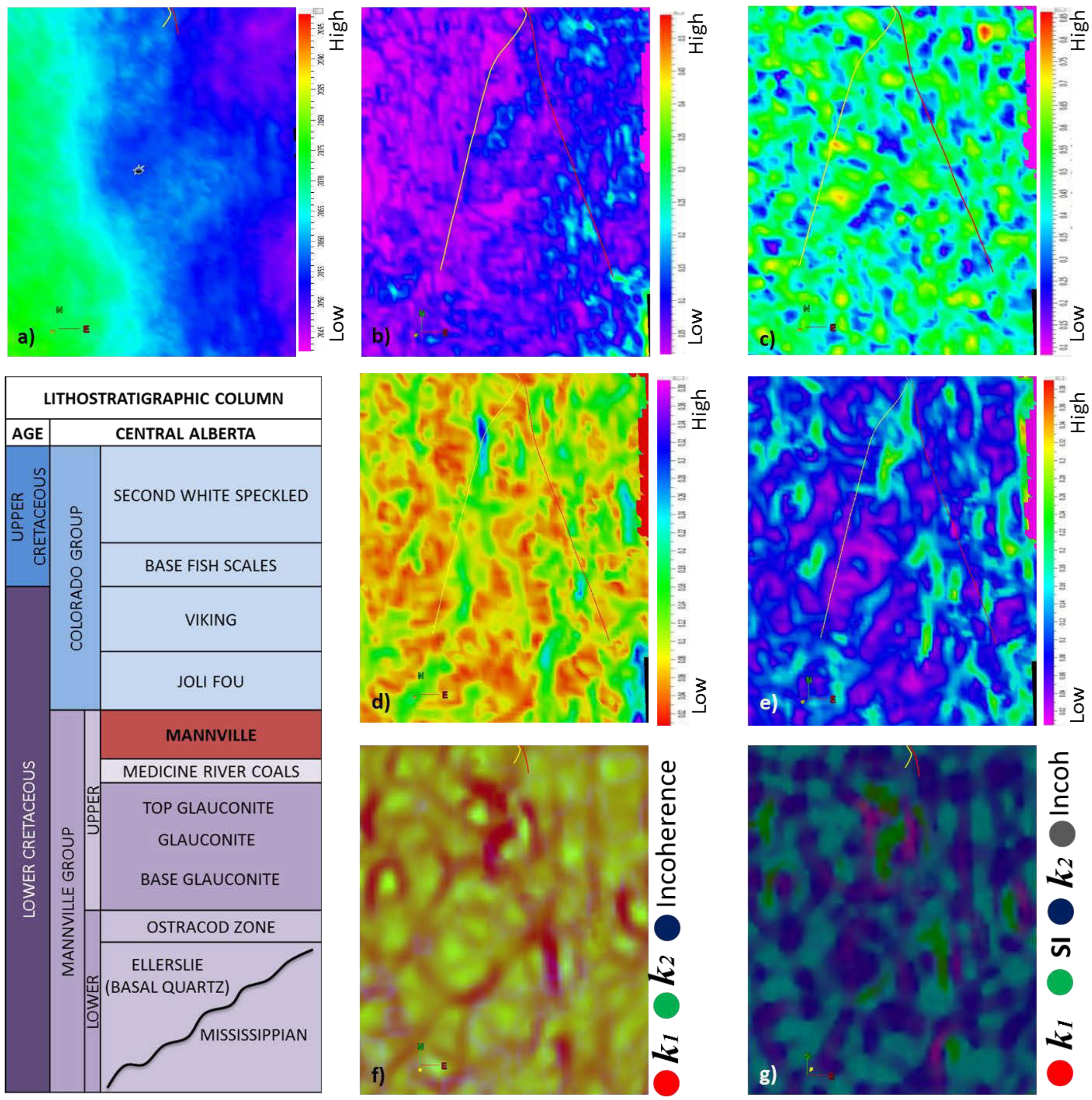

Figure 3.7: Depth horizon slices at Mannville horizon, showing the following attributes, a) amplitude, b) incoherence, c) shape index, d) most- positive curvature, (k_1), e) most-negative curvature, (k_2), f) most-positive curvature co-rendered with most negative curvature and incoherence on RGB scale, g) most-positive curvature co-rendered with shape index, most-negative curvature and incoherence on RGBGray scale.

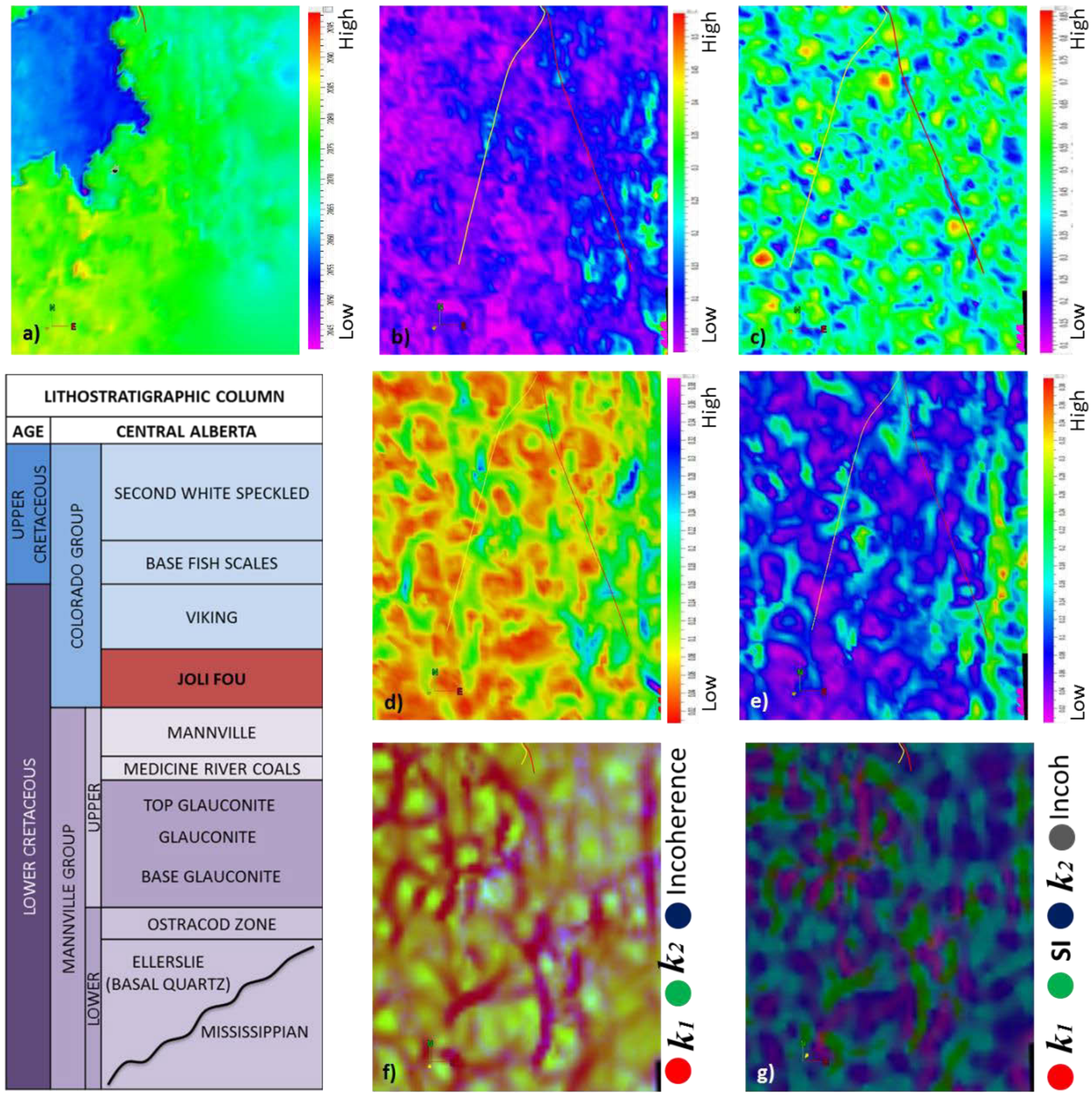

Figure 3.8: Depth horizon slices at Joli Fou horizon, showing the following attributes, a) amplitude (note high amplitudes), b) incoherence (note ~N-S trending anomalies shifting further towards north), c) shape index, d) most- positive curvature, (k_1), e) most-negative curvature, (k_2), f) most-positive curvature co-rendered with most negative curvature and incoherence on RGB scale, g) most-positive curvature co-rendered with shape index, most-negative curvature and incoherence on RGBGray scale.

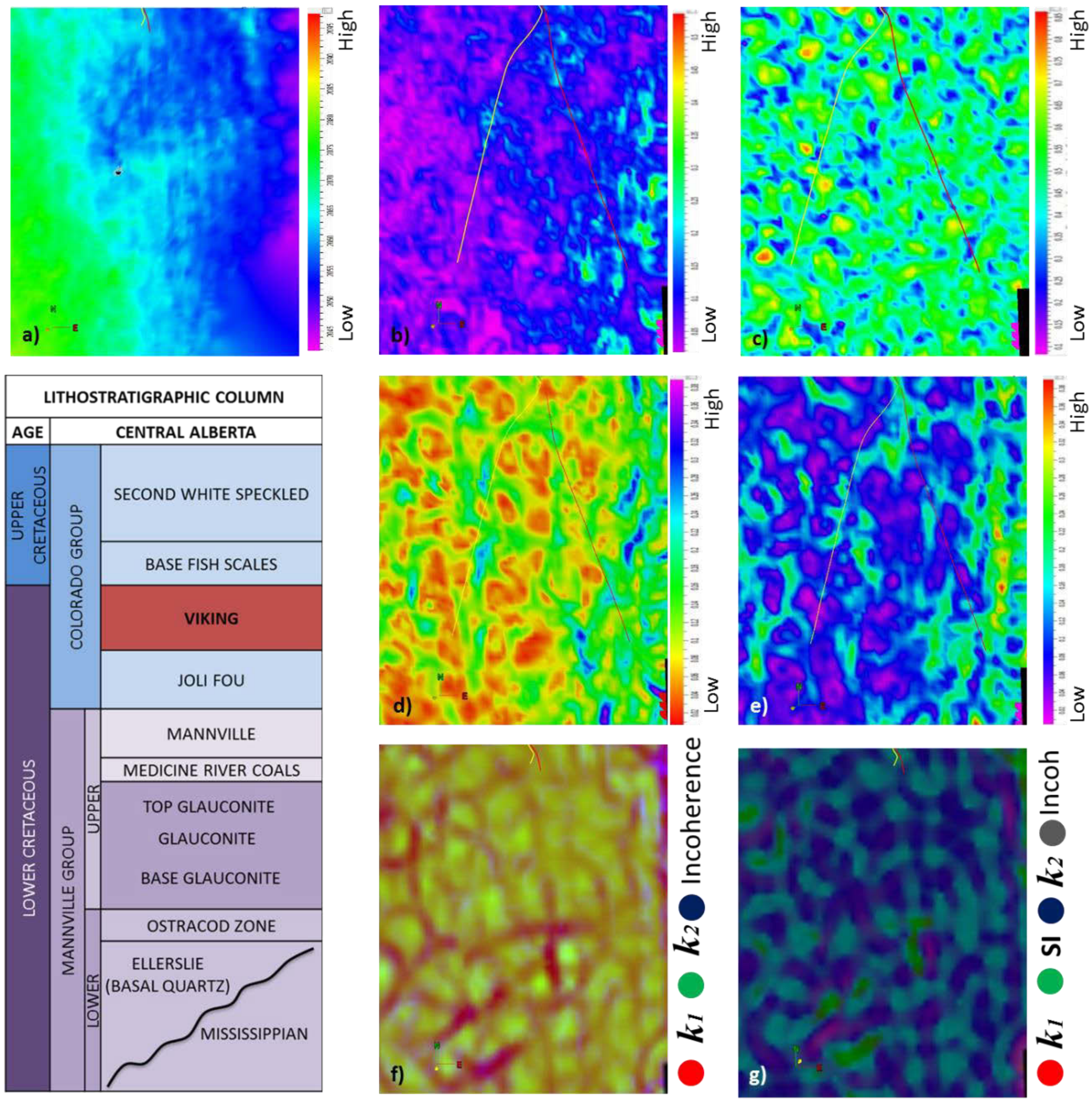

Figure 3.9: Depth horizon slices at Viking horizon, showing the following attributes, a) amplitude (note the sudden change in amplitude as compared to previous slide), b) incoherence, c) shape index, d) most- positive curvature, (k_1), e) most-negative curvature, (k_2), f) most-positive curvature co-rendered with most negative curvature and incoherence on RGB scale, g) most-positive curvature co-rendered with shape index, most-negative curvature and incoherence on RGBGray scale.

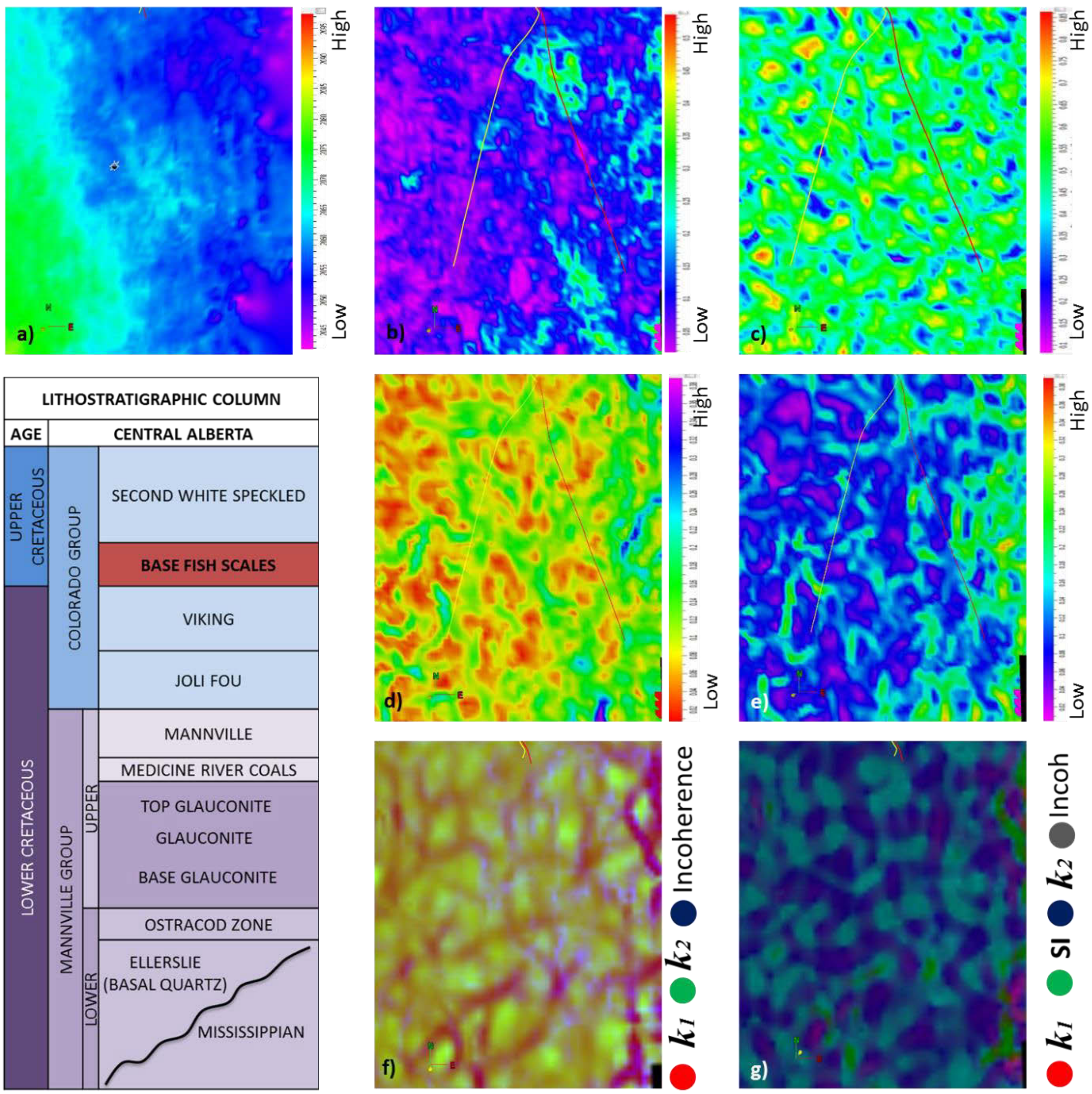

Figure 3.10: Depth horizon slices at Base Fish Scales horizon, showing the following attributes, a) amplitude, b) incoherence, c) shape index, d) most- positive curvature, (k_1), e) most-negative curvature, (k_2), f) most-positive curvature co-rendered with most negative curvature and incoherence on RGB scale, g) most-positive curvature co-rendered with shape index, most-negative curvature and incoherence on RGBGray scale.

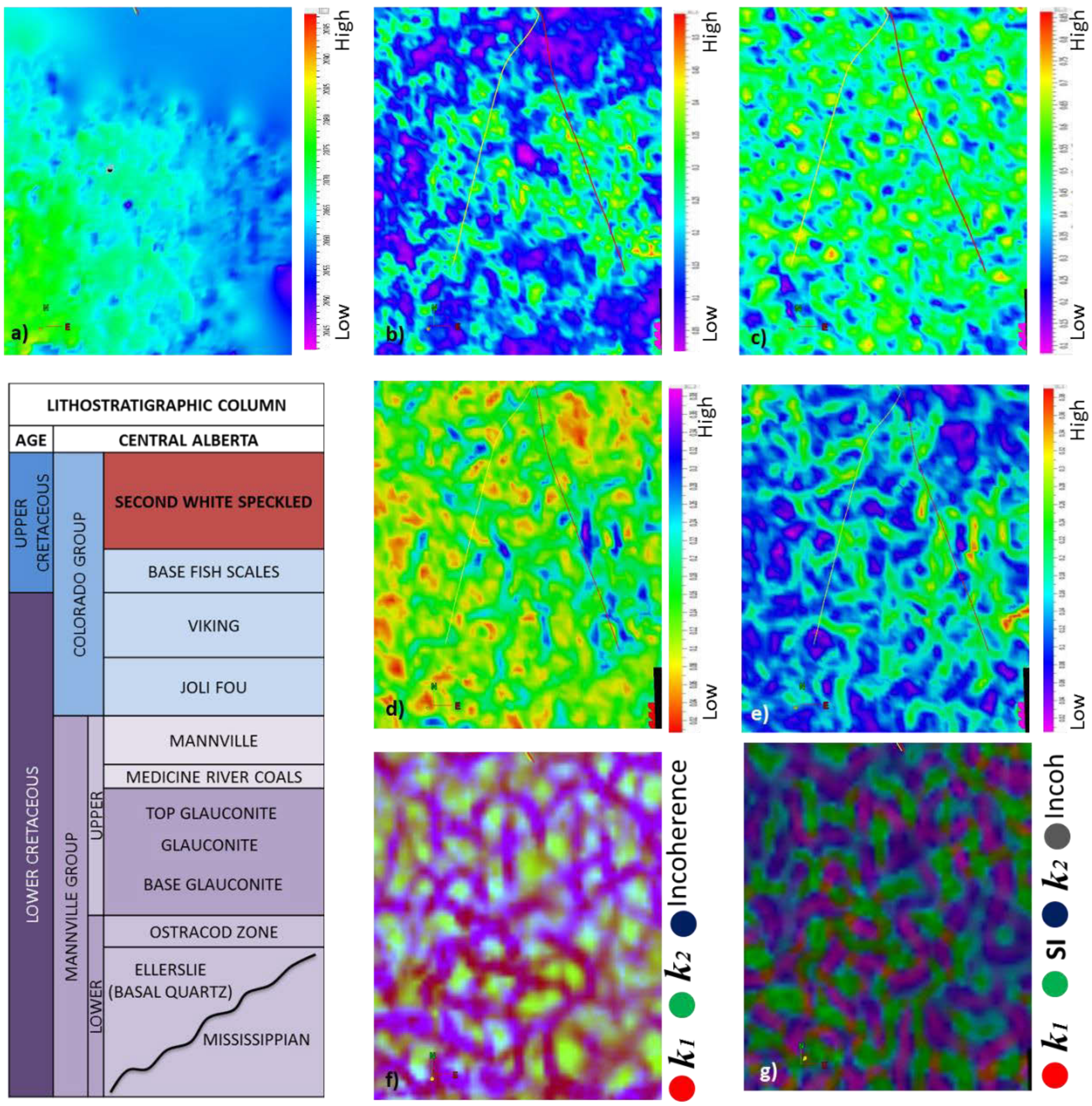

Figure 3.11: Depth horizon slices at Second White Specks horizon, showing the following attributes, a) amplitude, b) incoherence (note highly incoherent anomaly as compared to the previous slide), c) shape index, d) most- positive curvature, (k_1), e) most-negative curvature, (k_2), f) most-positive curvature co-rendered with most negative curvature and incoherence on RGB scale, g) most-positive curvature co-rendered with shape index, most-negative curvature and incoherence on RGBGray scale.

Taken by itself, the shape-index is more difficult to interpret. However, it appears to become useful when co-rendered with curvature and incoherence, where it is inferred to quantify the deformation morphology and delineate reservoir compartments.

3.3 Post-stack seismic data inversion for reservoir properties

Seismic inversion is a trace-based attribute in which each trace is inverted for acoustic impedance. The main purpose of inversion is to extract physical rock property and to enhance vertical data resolution in order to extract additional stratigraphic details to complement the seismic attributes computed before in this study. Since acoustic impedance (AI= ρV) is a layer property as well as physical rock property, we can estimate variations in lithology through variation in impedance.

Table 3.1 summarizes which elastic properties can be extracted depending on the type of seismic data inverted. Pre-stack and S-wave data information are not available for this study, from which many other rock property attributes can be computed. Consequently, this study focuses only on P-impedance (Zp) from the available post-stack time migrated P-wave data. The inversion workflow is outlined in Table 3.1.

3.3.1 Data conditioning, wavelet extraction and comparison

Before starting main processes in inversion, I conditioned the seismic and well log data. For this purpose I applied FX-deconvolution (FX-Decon) and structural oriented median (SOM) filter on seismic volume to remove noise and acquisition/processing footprint as discussed in the previous section and illustrated in Figure 3.1.

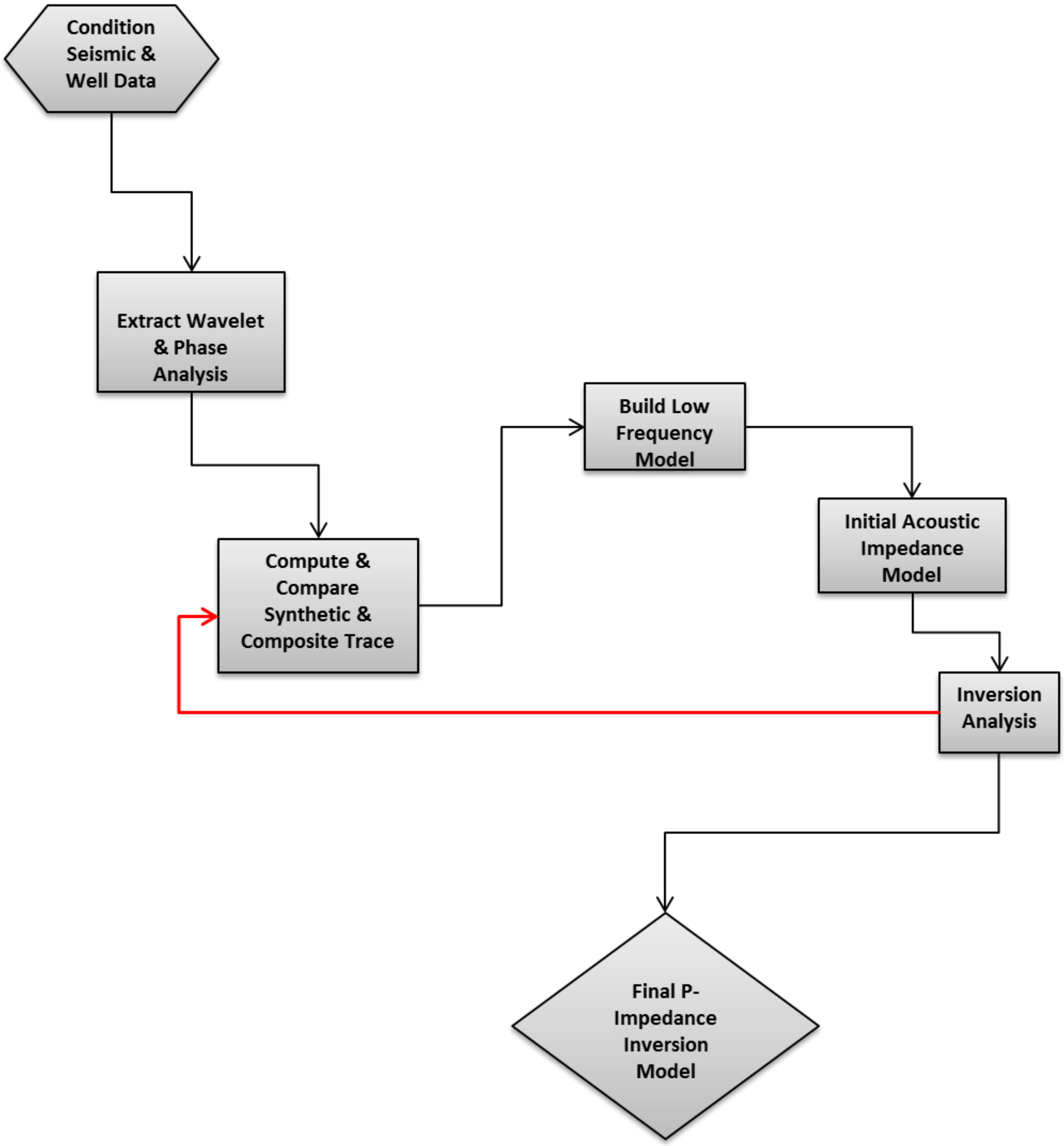

Figure 3.12: Workflow for model-based, post-stack seismic data inversion. (modified from HRS-9, help manual, 2013).

Table 3.1: Summary of rock properties extracted from different types of seismic data inverted.

Seismic Data Type	Rock Properties Extracted
Pre-stack gathers	**Zp , Zs ,Vp /Vs, λρ, μρ, λ/μ, λ , μ, ν and ρ**
Full stack P-wave	**Zp**
Full stack S-wave	**Zs**

I tie all the available well logs (sonic, density and resistivity) and horizons to the conditioned seismic data and then extracted statistical wavelet information, as shown in Figure 3.13. The methodology I followed uses autocorrelation of the seismic data, as the wavelet phase is assumed to be known in this method (Strata workshop slides, 2013). Note that the symmetric shape of wavelet shows that extracted zero-phase wavelet is accurate and phase average is zero, as shown in lower panel of Figure 3.13.

Steps 2 and 3 in the workflow include log processing and correlation with seismic. In this process, I computed composite synthetic trace from the wavelet (extracted in previous process) as shown in Figure 3.14. The log correlation panel in Figure 3.14 shows that the synthetic trace does not match with the composite trace. A newly extracted wavelet in lower panel, showing cross-correlation plot between synthetic trace and composite trace, suggests that a 5ms time lag exists. Figure 3.15 shows the results after 5ms shift applied. I stretched and squeezed synthetic trace to match with composite trace. Note the synthetic trace matches very well with composite trace in Figure 3.15.

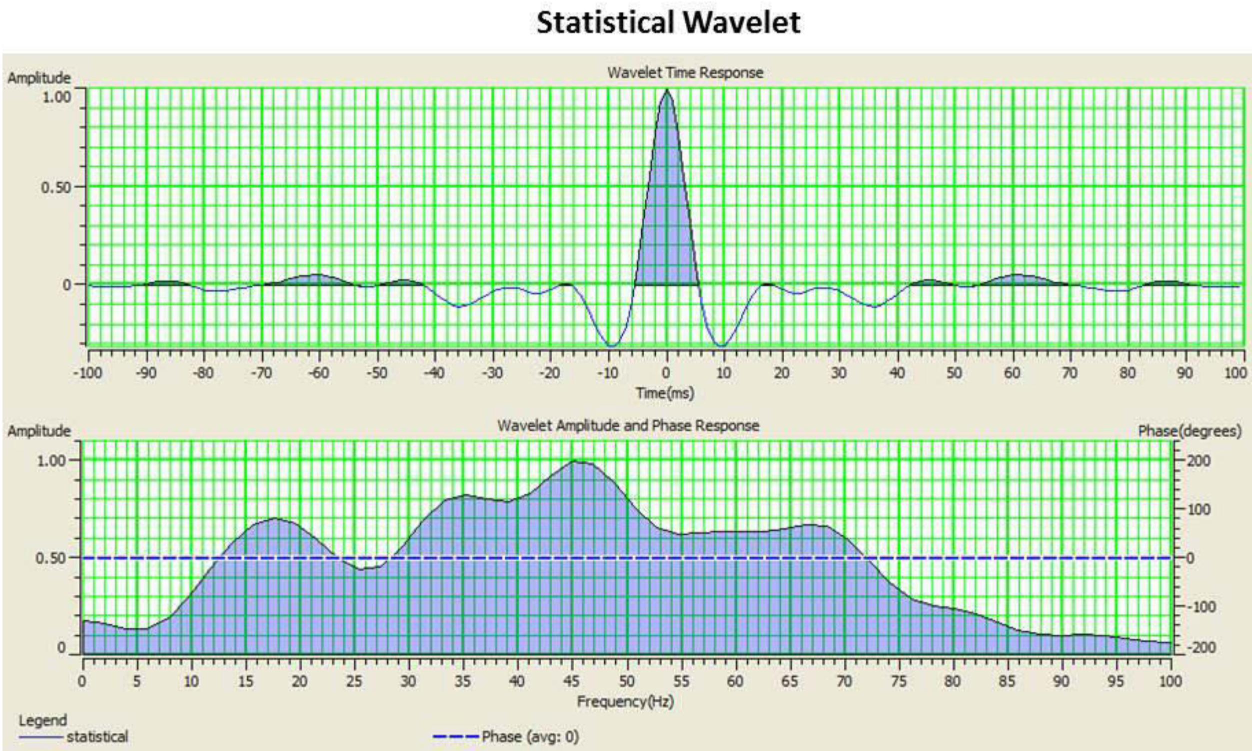

Figure 3.13: Wavelet extracted using a statistical method; phase is assumed to be known in this method. The symmetric shape in the upper-panel means that the extracted zero-phase wavelet is accurate. The lower panel shows that the average phase is zero.

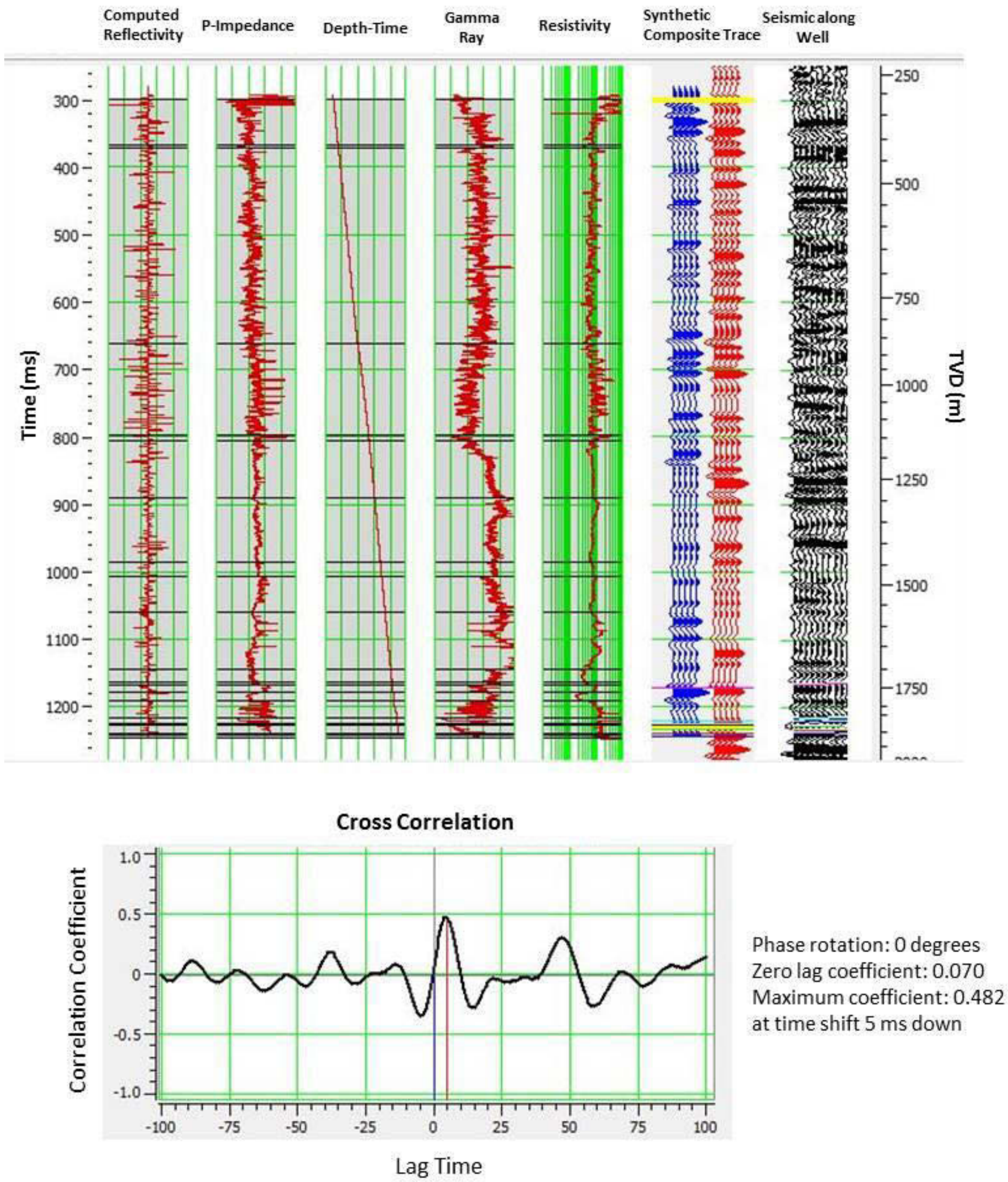

Figure 3.14: Log correlation window. Upper panel shows synthetic trace, which do not give a satisfactory match with actual seismic traces. The lower panel shows a cross correlation plot of the newly extracted wavelet, which indicates a maximum peak with 5ms lag.

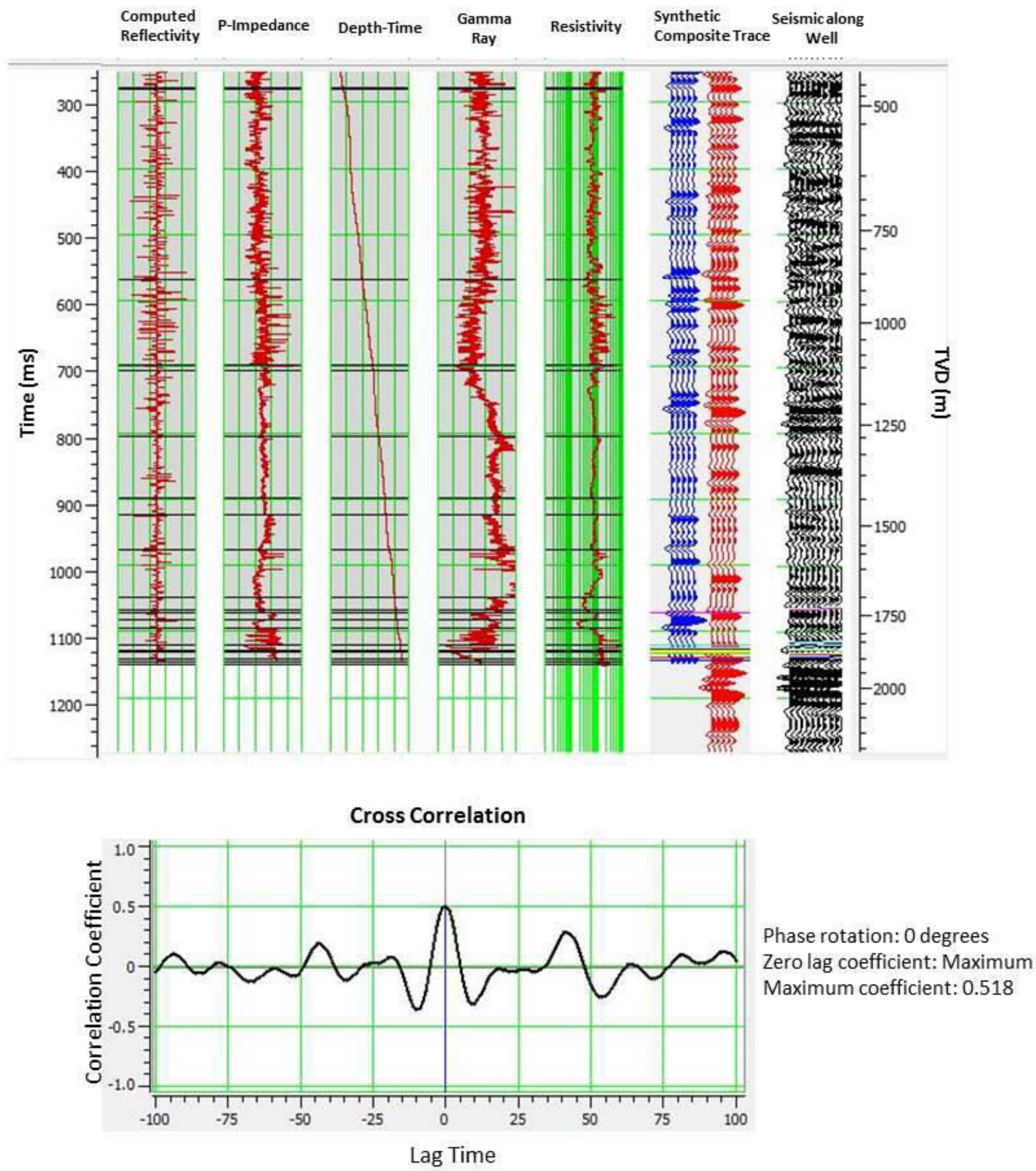

Figure 3.15: Log correlation window after applying time shift. Upper panel shows synthetic traces that match well with actual seismic traces after manual stretch and squeeze. The lower panel shows a cross correlation plot with maximum correlation coefficient of 52% after applying a 5ms time shift.

3.3.2 Low frequency model, inversion analysis and final P- Impedance model

Low frequency content is generally absent in seismic data (Russell and Hampson, 2006). We therefore need to introduce this content to the seismic inversion through well logs, to obtain absolute inverted impedance values (Barclay et al., 2008; Latimer et al., 2000).

I therefore built a low frequency initial strata model as shown in Figure 3.16. The figure shows a smooth initial model where color variation showing acoustic impedance contrast though x-line 190.

After building a low frequency model, the main inversion process begins is divided into two steps. The first step is inversion analysis at well location and the second step is to invert the whole 3D volume for final P-impedance model. Figure 3.17 shows the inversion analysis window. From left to right, the display shows the inversion result (in red), overlying the original impedance log from well. Farther right we see wavelet in blue and synthetic traces (red), followed by the seismic composite trace (in black) and to the extreme right is the error trace after 500 iterations, which is the difference between the composite trace and synthetic trace.

In the final stage the inversion results are carefully analyzed and the inversion is run for the full 3D volume. Figure 3.18 shows the final inversion model. The upper panel displays final P-impedance inversion model with horizons and wells, while the lower panel is the same display without horizons and well data. Different colors are used to show P-impedance (Zp) contrast at X-line 190 i.e. crossing wells.

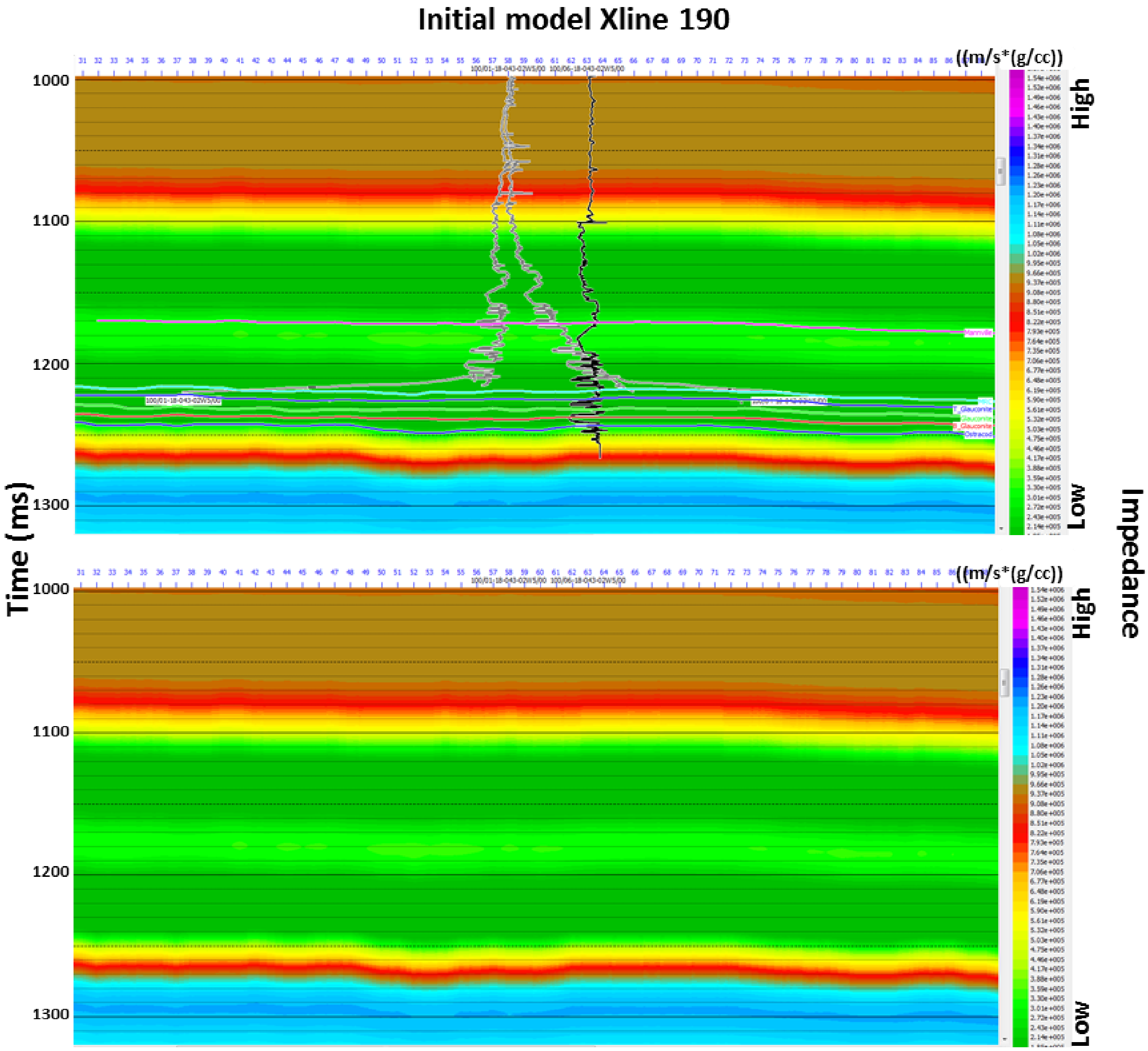

Figure 3.16: Smooth initial low frequency model built for post-stack time migrated data. Different colors show acoustic impedance contrast at X-line 190 crossing wells. Upper panel shows wells and horizons picks, while lower panel is without any horizon and well data.

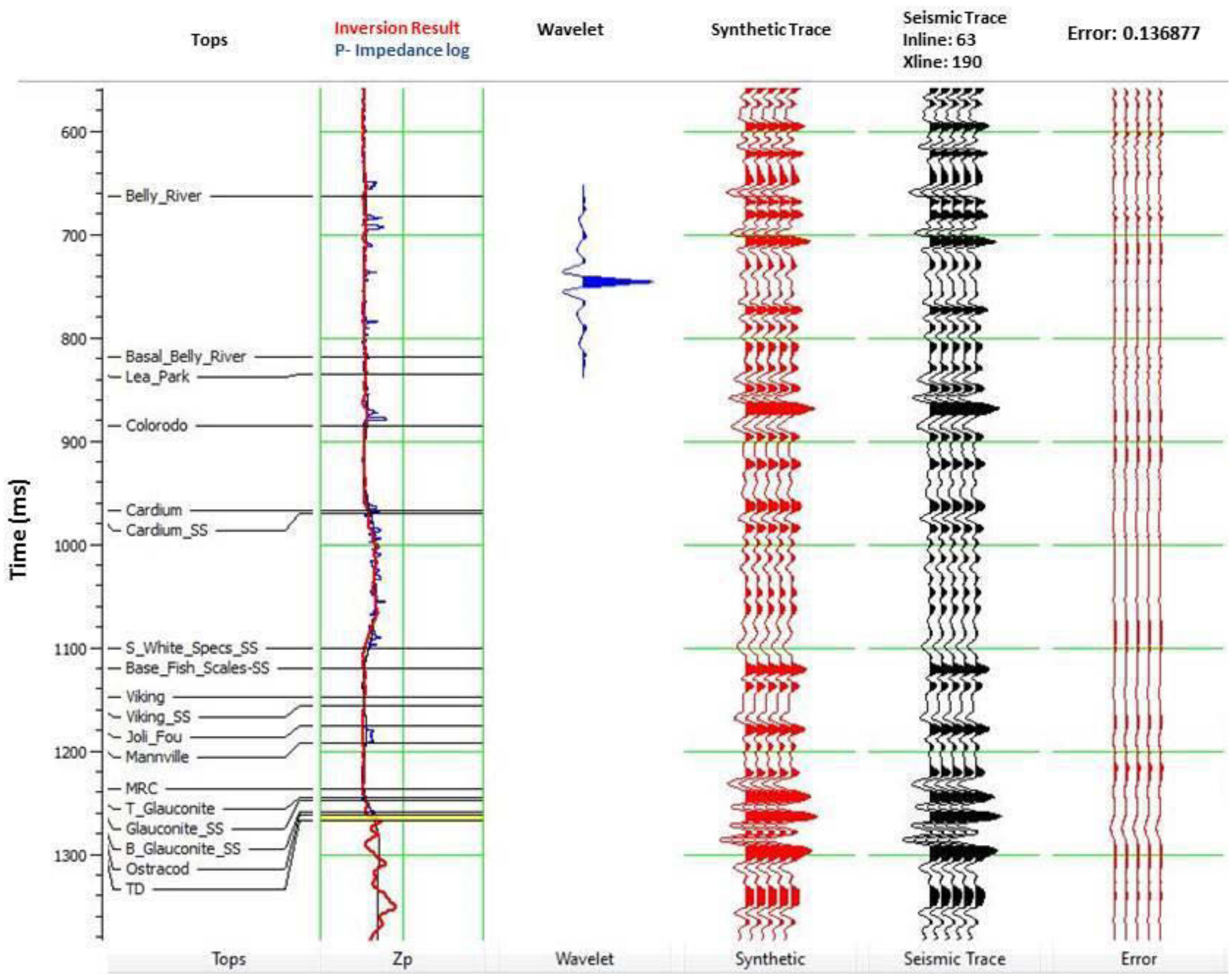

Figure 3.17: Inversion analysis panel after 500 iterations. Display shows the inversion result in red, overlying the original impedance log from well. To the right, the synthetic trace is shown in red, calculated from inversion, followed by the seismic composite trace in black and finally the error trace, showing very little error.

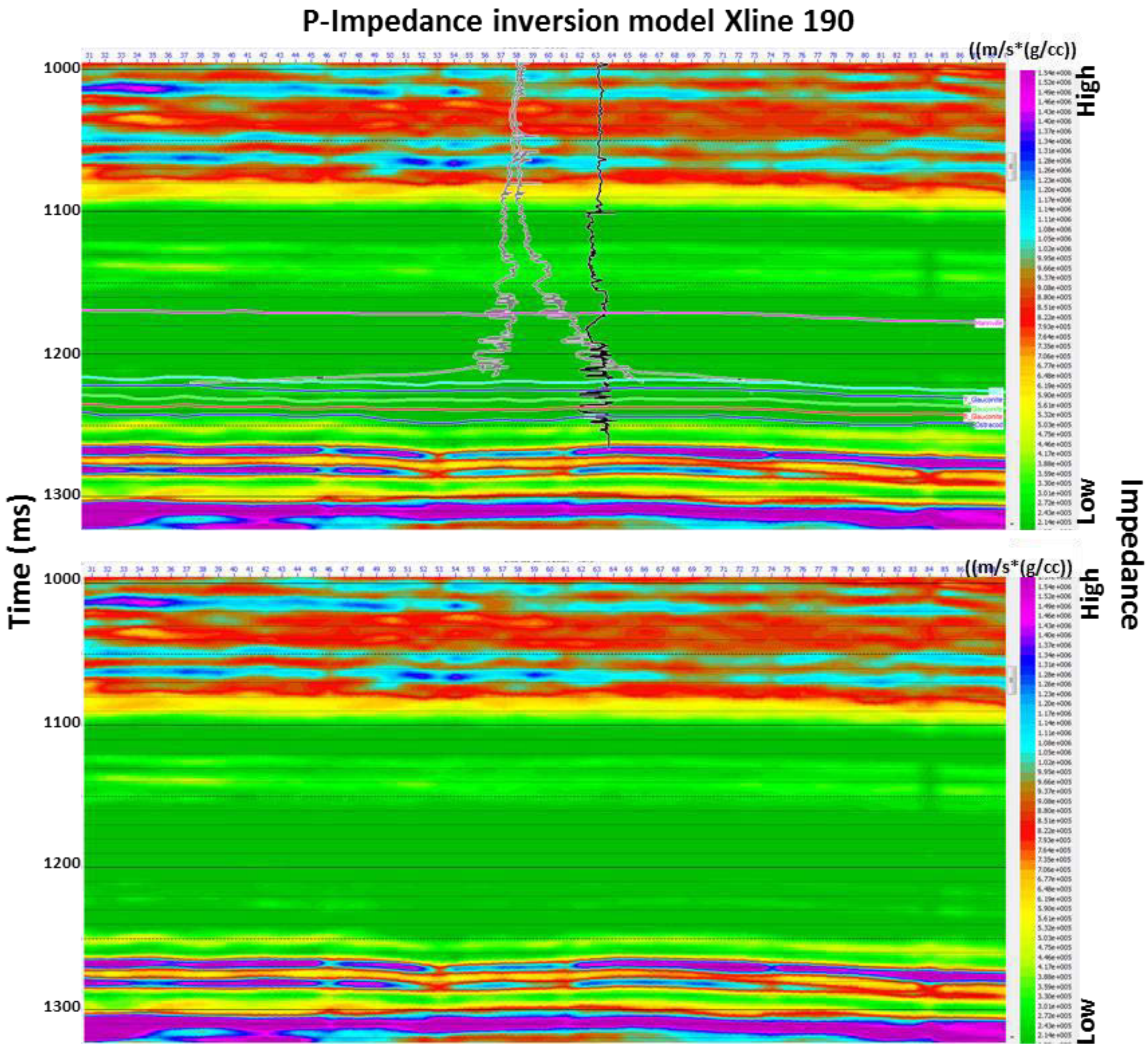

Figure 3.18: Final P-impedance inversion model run on whole 3D volume. Different colors are used to show P-impedance (Zp) contrast at X-line 190 crossing wells. Upper panel shows wells and horizons picks, while lower panel is without any horizon and well data.

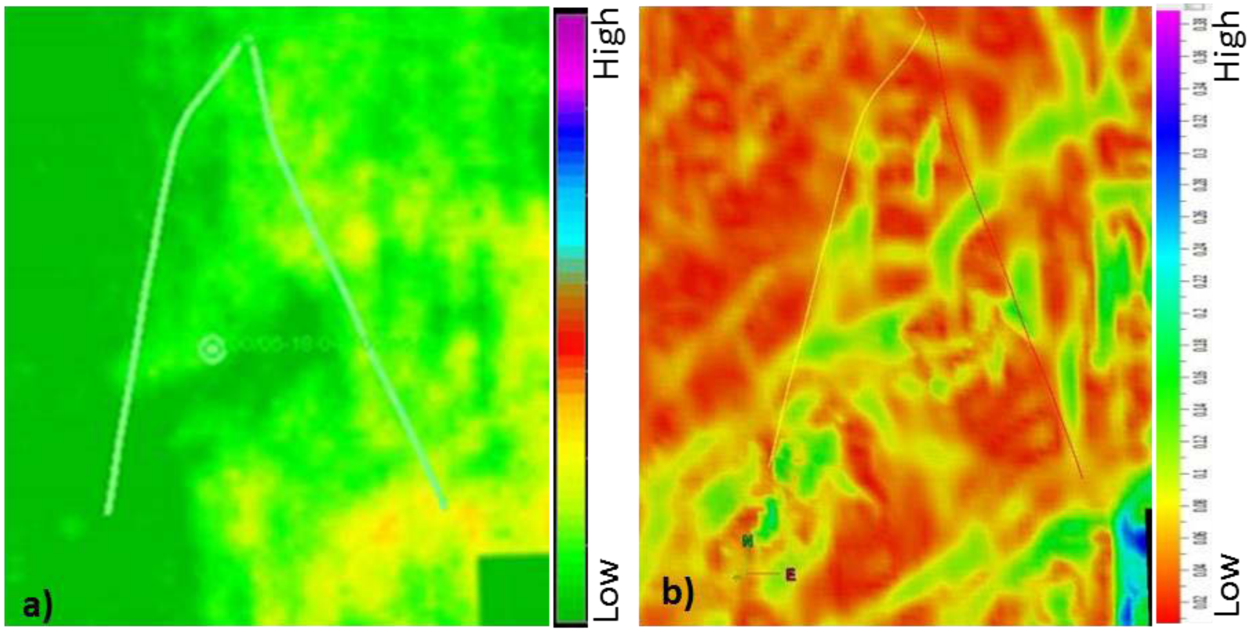

Figure 3.19: a) Time slice through P-impedance inverted volume of the post-stack seismic data at Glauconite level. b) Most positive curvature at the Glauconite level. Similarities are evident, especially in the southeast corner of the time slice.

It is well known that more than one rock type, having different reservoir quality, can produce the same P-wave impedance values. P-wave impedance characterizes the total effect of lithology, porosity and fluid content (Russell and Hampson, 2006). To estimate the effect of each of these factors (lithology, fluid content and porosity), information from S-wave data are required in addition to pre-stack gathers as explained in Table 3.1. The elastic moduli (lambda, mu, rho, Young's modulus), Poisson's ratio and Vp/Vs obtained from the inversion of pre-stack seismic data can be used in the discrimination of lithology, as a fluid indicator, and in providing information about stresses, brittleness and ductility of the reservoir.

Figure 3.19 shows the post-stack inversion slice at the reservoir level, along with the most positive curvature. The high impedance values in the southeastern part of the post-stack inversion map correlates with the NE trending features in the same area on the most-positive curvature map. Although high impedance values can correlate with the presence of fractures, it is essential for the sake of mitigating uncertainty in the interpretation that more information becomes available for the inversion. With the current limitations on data availability, more in-depth interpretation of post-stack inversion results is not possible.

Chapter Four: **Microseismic data analysis and interpretation**

Microseismic event analysis and interpretation provide valuable information about reservoir characteristics. Although there are numerous microseismic studies that focus on unconventional plays, relatively little attention has been given to microseismic attribute analysis. In this study we use a microseismic dataset that was recorded using downhole seismic monitoring array during stimulation of two horizontal wells in a Glauconitic tight sand of the Mannville Group in central Alberta. Over 1660 microseismic events were recorded and located during 24-stage fracture treatment, including 259 post-pumping events (Eaton et al., 2014a, 2014b). A detailed overview of microseismic acquisition, layout and survey geometry is discussed in chapter 2. Figure 4.1 and 4.2 shows a 3D and depth view of microseismic events respectively.

Microseismic attributes such as mean-magnitude, standard deviation, *b*-value (slope of frequency-magnitude distributions) and density, allow interpreters to map subtle stratigraphic details, structural deformation, fracture orientation, stimulated rock volume and stress compartmentalization within a reservoir (Eaton et al., 2014a). A possible link between microseismic magnitude statistics and reservoir properties was suggested by Eaton et al., (2014c), who showed that mechanical layering in a reservoir could result in stratabound discrete fracture networks (DFNs) that could lead to preferred scaling behaviour of magnitudes. Magnitude and *b*-values statistics are very useful attributes to delineate rock fabric (pre-existing zones of weakness) and hydraulic fractures resulting in fault activation (Maxwell et al., 2010).

In this study, I exploit these links and introduce a new approach to compute microseismic attributes. For validation of computed microseismic attributes and inferred reservoir sub-regions, microseismic observations are integrated with interpretation of surface seismic attributes that are discussed in chapter 3.

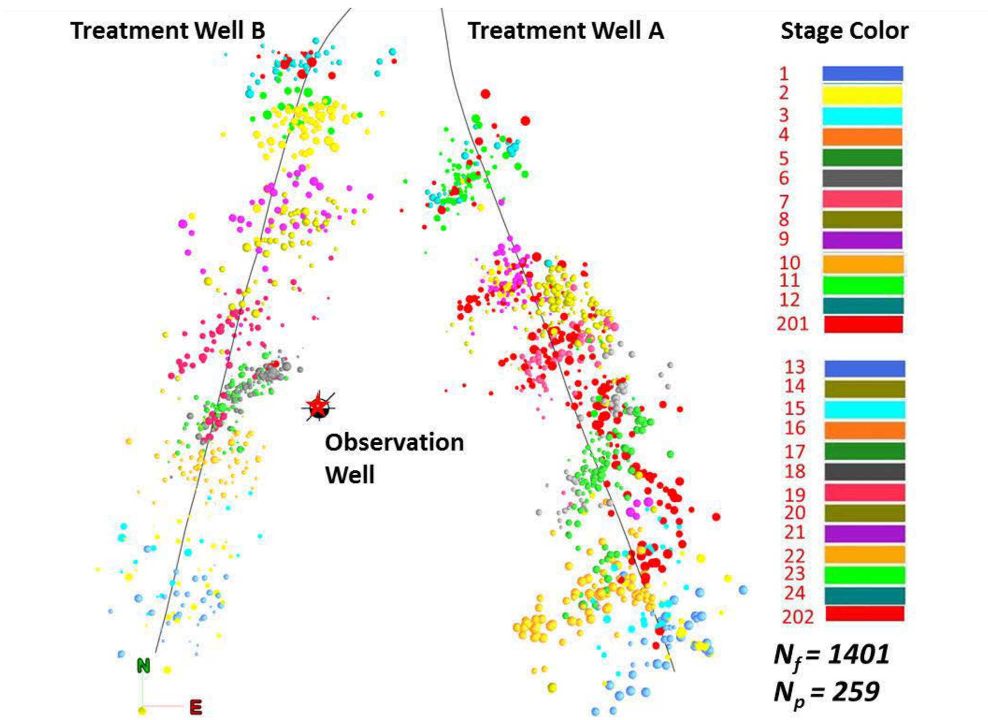

Figure 4.1: Three-dimensional view of the microseismic data recorded for the two horizontal treatment wells. A total of 1660 microseismic (MS) events were recorded during the 2-day hydraulic fracture treatment in 24 stages including 259 post-pumping events, shown in red color. Color denotes the stage number and size of symbol is modulated by magnitude. *Nf* and *Np* denote number of events recorded during fracture treatment and post-pumping periods, respectively.

4.1 Microseismic attributes defined

Microseismic attributes are defined here as a quantitative measure of any measureable property that can be extracted from microseismicity. Examples of microseismic attributes include seismic moment density, magnitude, *b*-value, and many combinations of these. More than 12 distinct microseismic attributes are available and the number is increasing with the development of technology and research methods.

I have analyzed microseismic data using different methods and computed numerous microseismic attributes e.g. standard deviation, mean magnitude and *b*-value statistics. Further I have tested various visualization combinations including cross-plot analysis to extract useful information, comparable to surface-seismic attribute interpretation. Microseismic attribute analysis is discussed in detail below in this chapter.

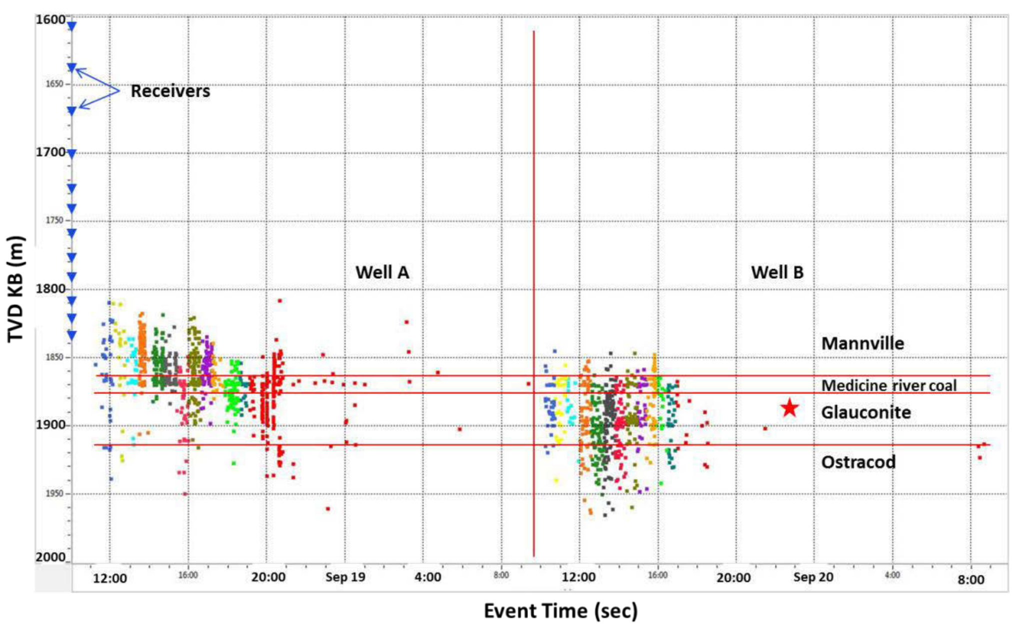

Figure 4.2: Distribution of microseismic events with respect to stratigraphic layering. Microseismic event depth/time plot, showing the event above and below the Glauconite, treatment zone is indicated by red star. Receiver locations are indicated by blue triangles.

4.2 Microseismic data analysis

Microseismic events from a 24-stage open-hole completion in two horizontal wells (Eaton et al., 2014b) are shown in Figure 4.1, including 259 post-pumping events. Typical information provided within the microseismic dataset includes the estimated XYZ coordinates, the local date/time of occurrence, and magnitude of microseismic events. A weighting factor indicating the reliability of microseismic moment magnitudes is also included.

I have performed statistical analysis of microseismic data to prepare it for integrated interpretation and correlation analysis with surface seismic. For this purpose, I have developed two different approaches to analyze microseismic data:

1. *microseismic facies analysis* through Interactive classification of microseismicity into distinct clusters;
2. reservoir classification based on magnitude statistics, *b*-value and rock fabric.

4.2.1 Microseismic facies analysis

Here, I introduce a novel approach, *Microseismic Facies Analysis*, to extract additional information from microseismic event clusters. Our approach is based on proposed links between magnitude-frequency distributions and scaling properties of reservoirs such as mechanical bed thickness. I define *microseismic facies* as a body of rock with specified characteristics extracted from microseismicity.

The following workflow summarizes the steps involved in *microseismic facies analysis* and correlation with surface seismic attributes:

- Interactive classification of microseismicity into distinct clusters.

- Refinement of selected clusters through elimination of outliers by visual inspection and spatial distribution (Figure 4.5).
- Calculation of stimulated reservoir volume (SRV) for each cluster using convex hull algorithm (Figure 4.6).
- Estimation of mean magnitude and standard deviation statistics for each cluster (Table 4.1).
- Identification of clusters with similar information on mean magnitude vs. standard deviation cross-plot. This provides the spatial zonation of cluster (*facies*) with similar statistics (Figure 4.7).
- Correlation of *facies* zones with surface seismic attributes (Figure 4.8).

Figure 4.4 shows the event locations for the 24 treatment stages with an additional 2 stages of post-pumping events for the two treatment wells, labelled here as A and B. In this analysis, I carefully visualized and divided the events that occurred during treatment of Well A into seven clusters and those that occurred during the treatment of Well B into another seven clusters, based on spatial distribution as shown in Figure 4.6. The clustering analysis resulted in either grouping of events from multiple stages, or elimination of spatial or temporal outliers. Multiple stages are grouped together in cases where there is significant overlap in event locations between stages, including persistence of activity after the treatment time window for a given stage. In general, clusters are elongate in NE-SW direction, which is also the direction of regional maximum horizontal stress (SHmax) and may indicate the newly generated fractures as shown in Figure 4.3. Some clusters exhibit trends that deviate significantly from SHmax; these are interpreted as activation of pre-existing fracture systems (Eaton et al., 2014a).

Stimulated reservoir volume (SRV) is calculated for each cluster using a convex hull algorithm as shown in Figure 4.6 and Table 4.1. Eaton et al., (2013) describe a procedure to estimate stimulated reservoir volume (SRV) using the method of convex hulls. Formally, a convex hull is defined as the smallest convex set containing all of the points from a point cloud (e.g., Barber et al., 1993). The volume is formed from triplets of points and thus creates a tessellated convex volume comprised of triangular surface elements. Informally, a convex hull can be viewed as a shrink-wrapped surface around the exterior of the point cloud. Here, this method is implemented using the convhull intrinsic command in matlab, which uses the quickhull algorithm (Barber et al., 1993). Practical advantages of the use of convex hulls include uniqueness for a given point cloud and its inherently conservative estimate of volume, since it is the smallest convex volume that contains the points.

In practice, clusters can be estimated by defining a polyhedral region around a cluster of microseismic events that are interpreted to form a spatially coherent cluster. This process is performed interactively using the matlab functions ginput and inpolygon. Once clusters of microseismic events have been identified, the statistical characteristics can be determined such as mean and standard deviation of magnitude, SRV dimensions, cluster orientation, etc. Table 4.1 summarizes the statistics calculated from each cluster.

Magnitudes of microseismic events due to hydraulic fracturing in a layered medium can be strongly influenced by the scale-length of layering (Eaton et al., 2014c). In particular, the common occurrence of fracture arrest at bedding boundaries gives rise to stratabound fracture networks. In these circumstances, the distribution of event magnitudes may deviate significantly from the commonly assumed power-law distribution implied by the Gutenberg-Richter relation from earthquake seismology. In particular, a regular layered bed-set would be expected to produce a magnitude distribution with a small standard deviation, whereas a bed-set with a large range of thicknesses due to complex depositional environment may exhibit a large standard deviation.

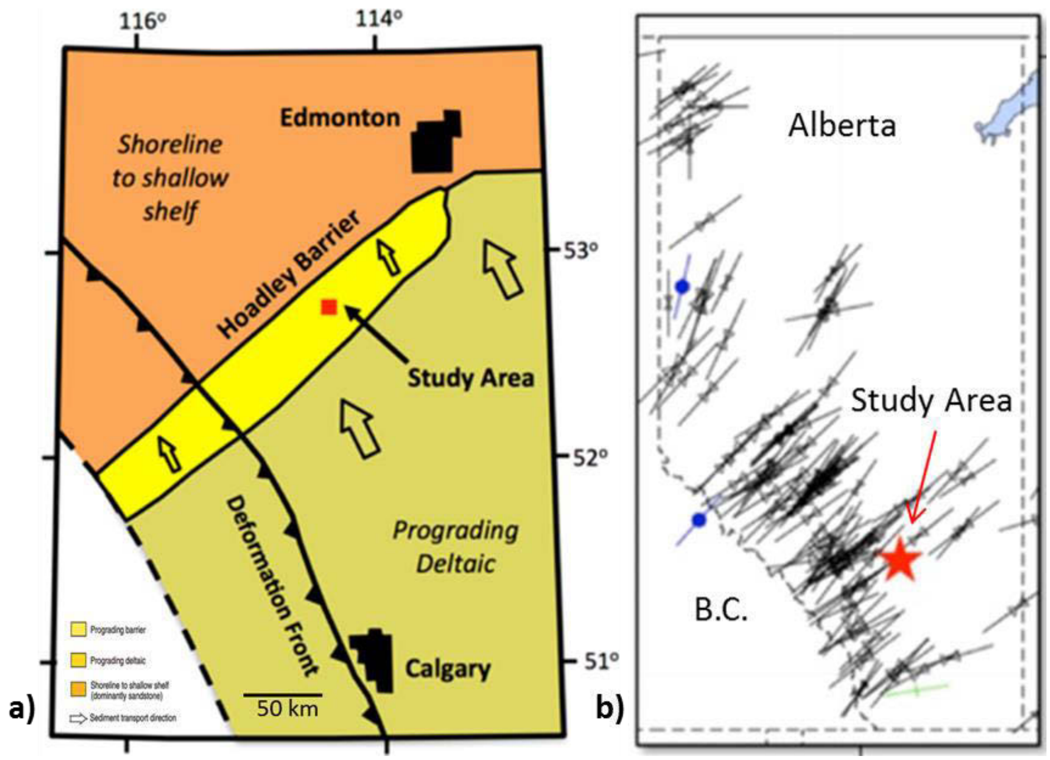

Figure 4.3: a) Location map of the study area, showing Cretaceous paleogeography of Hoadley barrier bar complex. Open arrows show sediment transport direction i.e. ~NW-SE. (modified from Smith, 1994), b) Regional stress orientation map showing NE-SW trending maximum horizontal stress direction (world-stress-map.org).

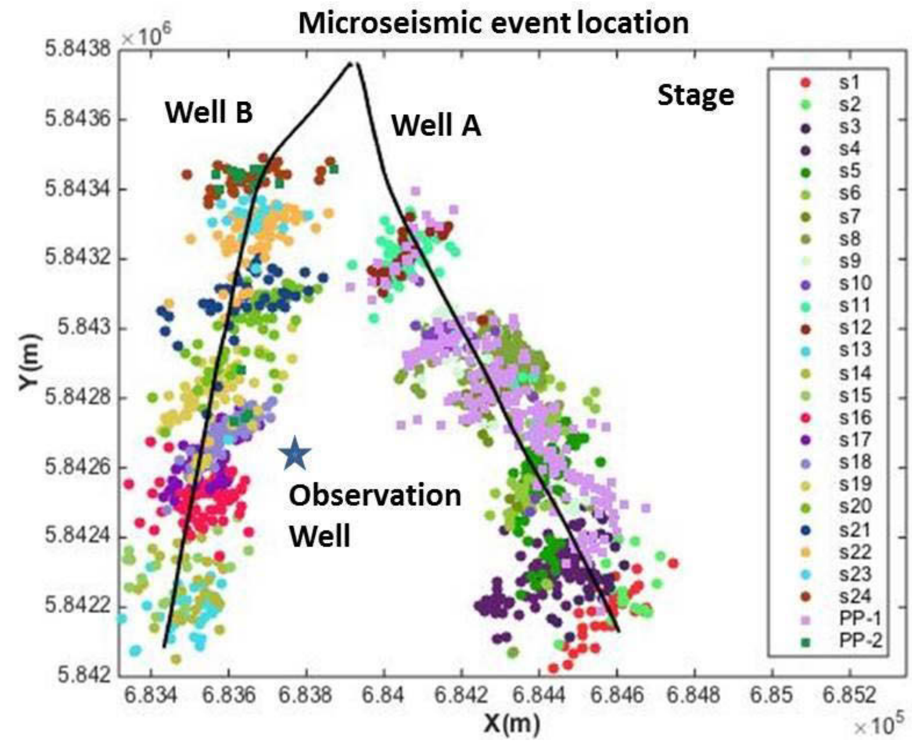

Figure 4.4: MS event locations for the 24 treatment stages with additional 2 post-pumping stages. Stage number is shown by symbol color. Observation well is indicated by blue star.

Figure 4.7 shows a cross-plot of mean magnitude versus standard deviation derived from the magnitude distribution within the inferred microseismic clusters. Based on this cross-plot, I interpret a number of possible microseismic facies. According to the interpretive framework outlined above, the four clusters of events with the largest mean magnitude may occur within the most brittle (quartz-rich?) and/or massively bedded region of the reservoir indicated as facies zone A. In contrast, the three clusters in facies zone C, with the lowest standard deviation may represent a relatively homogeneous but less brittle region, whereas the remaining seven microseismic clusters shown as facies zone B may occur within a region that has more diverse bed thickness characteristics but is less brittle than the first set of microseismicity clusters. Based on clusters of events in Figure 4.7, I divided well A & B into facies zone A, B and C (Figure 4.8a) and for comparison, I plotted these zones onto most positive curvature (k_1) attribute in Figure 4.8b, which indicates that most of the events tends to occur on or near positive curvature anomaly. This attribute describes anticlinal features as positive anomaly that is comparable to the major structures in study area, as shown in figure 4.3a.

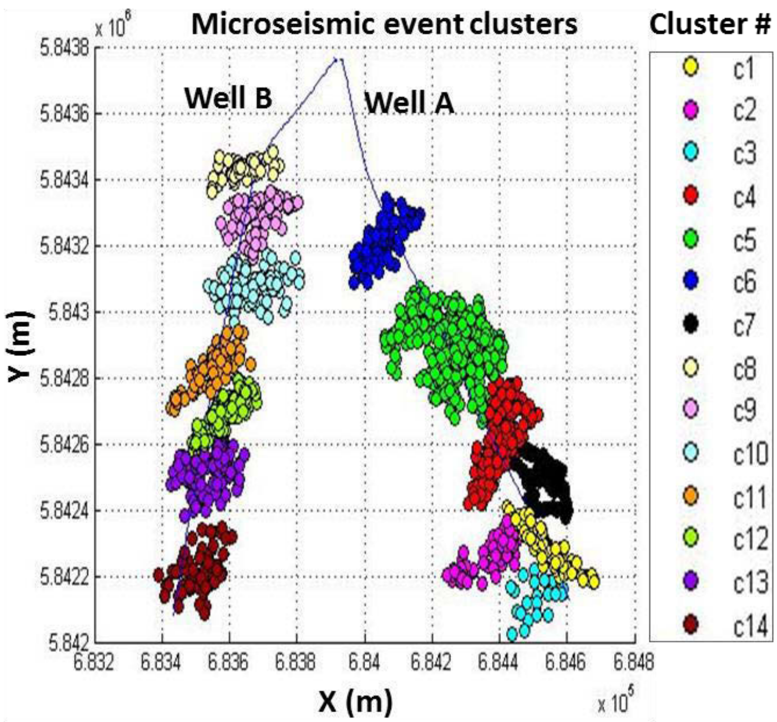

Figure 4.5: MS event clustering based on spatial distribution. Each well A and B is divided into seven clusters.

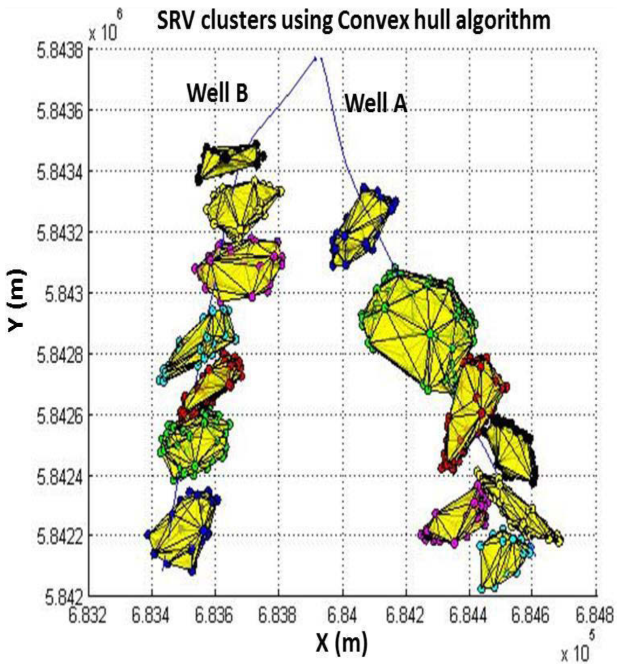

Figure 4.6: Stimulated reservoir volume (SRV) computed for each cluster using convex hull algorithm.

Table 4.1: Statistics of microseismic analysis calculated for each convex hull.

Cluster #	Mean (M_w)	STD (M_w)	SRV (m^3)	Zone
1	-1.74	0.19	$1332x10^3$	A
2	-1.64	0.21	$557x10^3$	
3	-1.75	0.23	$763x10^3$	
4	-1.89	0.20	$1843 x10^3$	B
5	-1.95	0.20	$6893x10^3$	
6	-1.98	0.17	$922x10^3$	
7	-1.74	0.23	$1407x10^3$	A
8	-1.95	0.21	$606x10^3$	C
9	-1.83	0.15	$1390x10^3$	
10	-1.87	0.15	$2093x10^3$	
11	-1.94	0.15	$1223x10^3$	
12	-2.07	0.21	$1338x10^3$	B
13	-2.12	0.16	$2209x10^3$	
14	-2.04	0.18	$1448x10^3$	

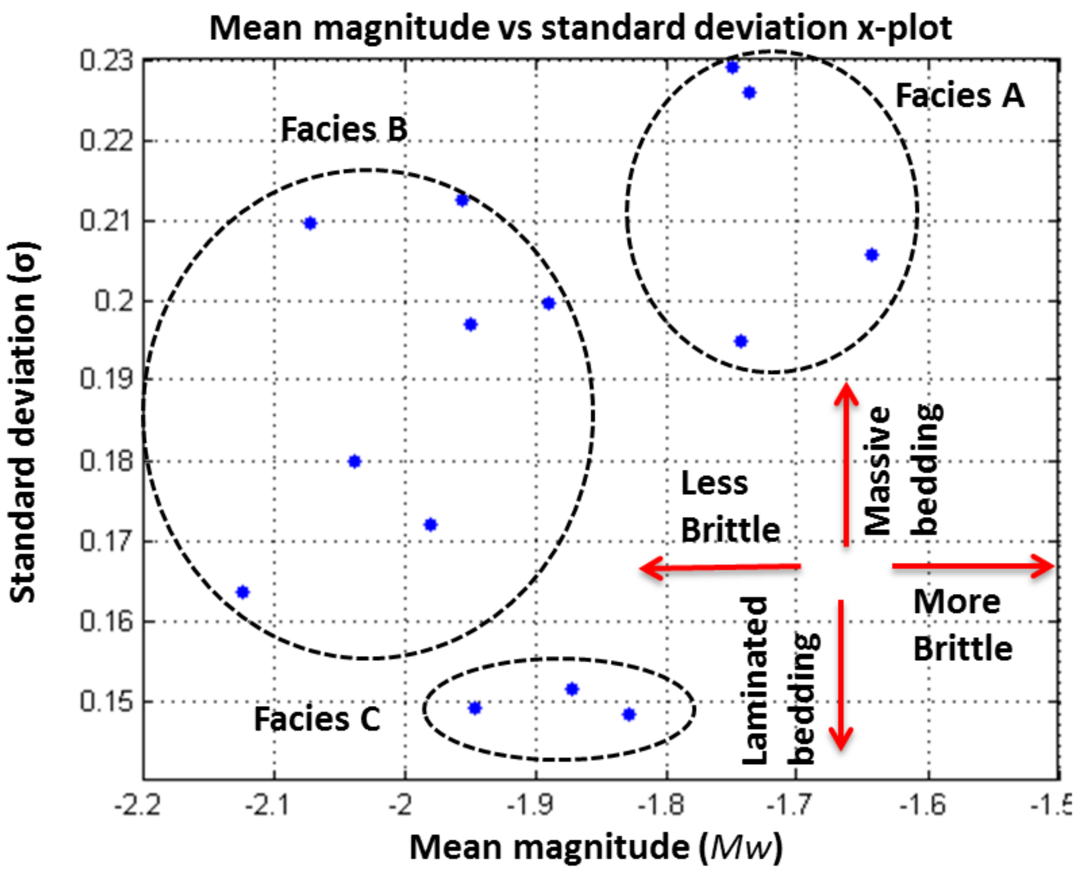

Figure 4.7: Mean magnitude (*Mw*) vs standard deviation (σ) cross-plot. Zones A, B and C are interpreted as three distinct microseismic facies.

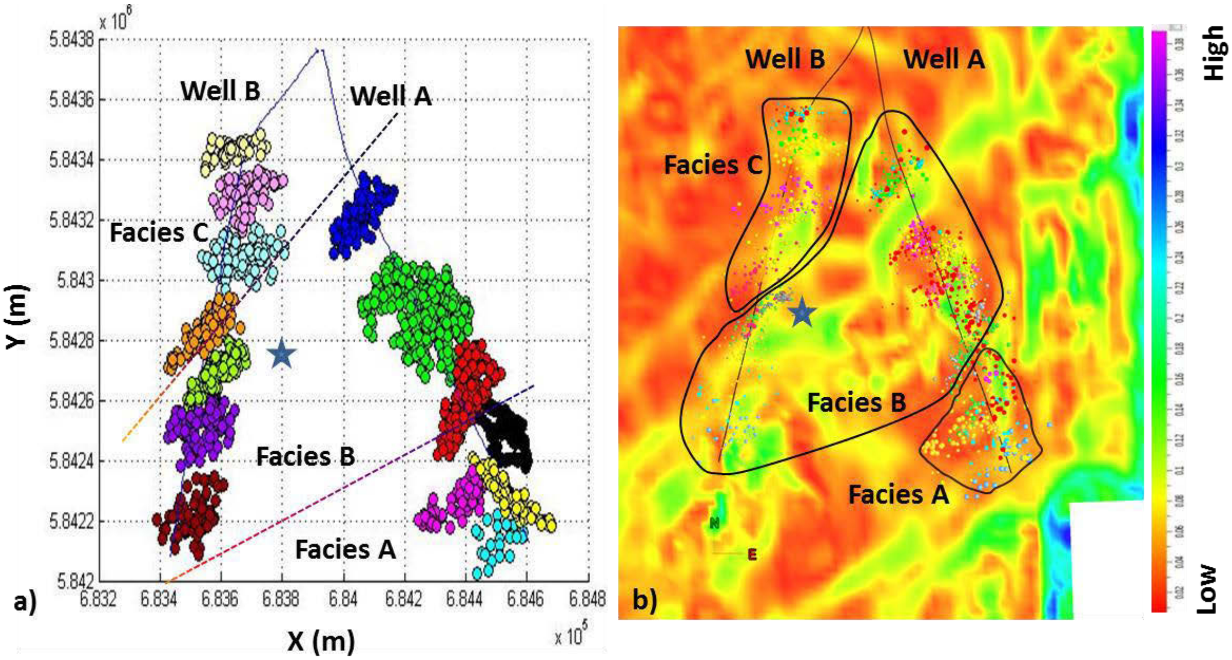

Figure 4.8: a) Microseismic zonation of well A and B based on mean magnitude-standard deviation cross-plot, interpreted as three distinct microseismic facies. b) Depth slice of most-positive curvature (k_1) at Glauconite level overlain with microseismicity and *microseismic facies zones*. Strong NE-SW (green) lineaments follow major surrounding structure, part of barrier bar complex.

4.2.2 Reservoir classification based on magnitude statistics, b-value & rock fabric

An integrated approach is developed, based on proposed links between magnitude, *b*-value and rock fabric (Haege et al., 2013). Significant variations and complex geometry in fracture evolution is observed in short intervals along the lateral path of the well A and B in our study area. The factors that cause this variability are still under study. In addition to local stress variations and heterogeneity of the reservoir rock, pre-existing faults/fractures are expected to play an important role in developing complex fracture patterns (Haege et al., 2013).

The following workflow was applied to analyze magnitude, *b*-values and rock fabric statistics.

- QC magnitude distribution and variation along lateral and vertical section;
- identifying zones of varying geomechanical behaviour based on magnitude-event density cross-plots, *b*-values and correlation with surface seismic attributes.

4.2.2.1 Magnitude statistics analysis

The magnitude-distance cross-plot shown in Figure 4.9 is very helpful in certain QC aspects. Typically, hydraulic fracture treatments create events that are visible above a distance-dependent detection magnitude (Zimmer et al., 2007). The minimum detection limit is computed which is M_W -2.5 in our case, as indicated by trend of red line in Figure 4.9. A magnitude of completeness threshold needs to be established to remove detection bias (Maxwell et al., 2011). It is estimated that events with magnitude of -2 and greater will be recorded anywhere within ~1100m of the source.

Since the hydraulic fracture treatment was undertaken using an open-hole completion methodology with essentially the same parameters for each stage, it is expected that if the reservoir and stress state is uniform then the microseismic response for every stage should remain similar (Reynolds et al., 2012). The results, however, show a complex distribution of magnitudes indicating variability in rock fabric (pre-existing zones of weakness) within the reservoir, as shown in Figure 4.1 and 4.10. In particular, we observe a variable depth distribution and variable density of microseismic events consisting of a mix of relatively low and high magnitude events.

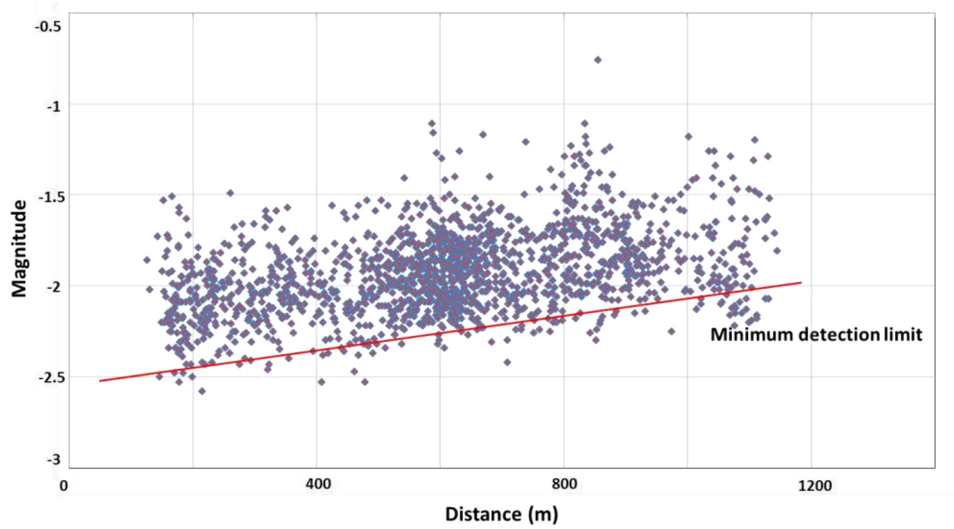

Figure 4.9: Magnitude-Distance cross-plot shows the minimum detection limit. A magnitude limit of -2 will remove the detection bias within a distance of ~1100m.

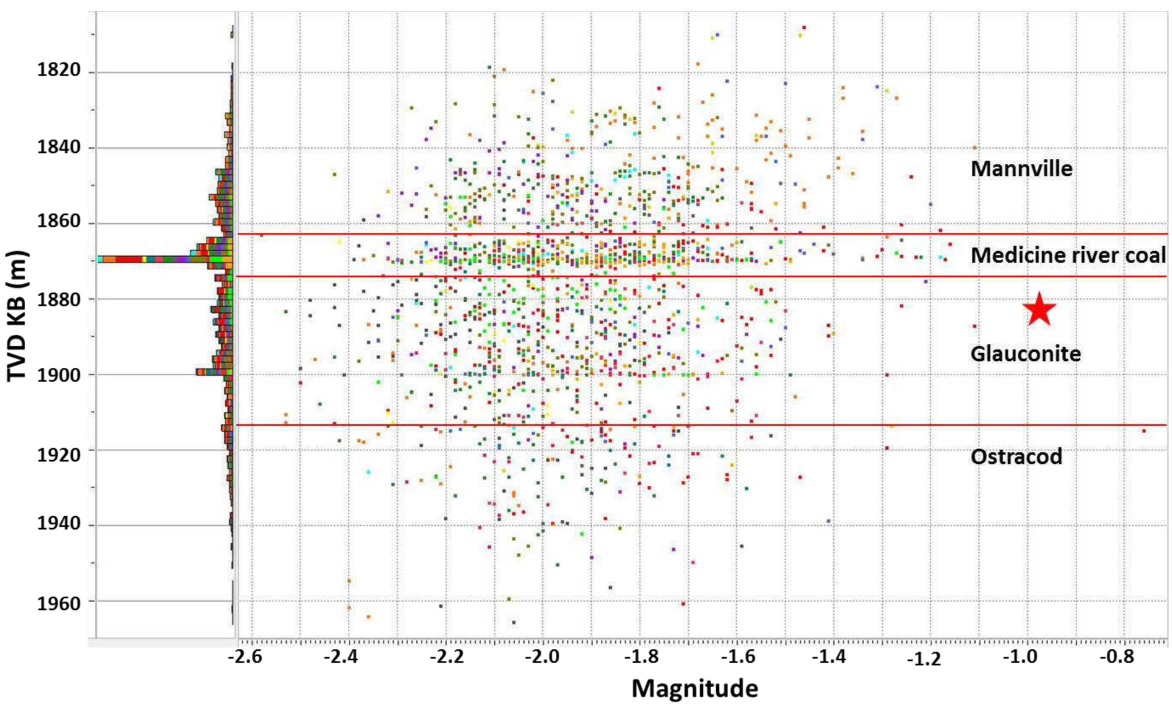

Figure 4.10: True vertical depth (TVD)-Magnitude cross-plot showing complex distribution of low/high magnitudes along depth of reservoir indication variability in rock fabric.

It is evident from the true vertical depth (TVD) versus time and TVD-magnitude cross-plots of microseismic events in Figure 4.2 and 4.10, respectively, that microseismic activity stimulated by the hydraulic fracture treatment occurs at a range of depths that extends into strata above and below the treatment zone i.e. Glauconite, indicated by the red star symbol. Caution should be exercised in the interpretation of these event depths, as they may contain artifacts related to the large velocity change at the Medicine River Coal. Nevertheless, it is evident from Figure 4.2 that fracture height growth above and below the reservoir level has likely occurred.

Well A and B exhibit significant differences in apparent fracture height growth through the aerially extensive Medicine River Coals. In Figure 4.2, the distribution of microseismic events near well A shows that most occur above the reservoir zone, i.e. within Medicine River coal and Upper Mannville. In contrast, microseismic event clouds near well B indicate that microseismicity occurs within and below the reservoir zone. It is also evident in Figure 4.2 that saturation of events and apparent “blunting” of the event distribution occurred near the interface of Medicine River Coal, at depth of 1865m. As rock mechanical properties of coals generally tend to reduce fracture propagation, bedding-plane slippage may have occurred at interface (Reynolds et al., 2012; Pike, 2014). I attribute this difference in microseismic event distribution in wells A and B to heterogeneity and varying rock fabric throughout the reservoir, in addition to the overlying coals and shale section. Based on a comparison of these results with surface seismic attributes shown in Figure 3.2 to 3.11 and 4.8b, I interpret the reservoir to be compartmentalized; wells A and B have distinct facies with varying rock fabric.

A large fraction of the event clusters in wells A and B are aligned subparallel to the regional maximum horizontal stress (SHmax) direction, which is NE-SW. Event clusters that are oblique to this trend are interpreted as re-activation of pre-existing zone of weakness (Eaton et al., 2014), as shown in Figure 4.1 and 4.3b. It can also be seen from Figure 4.1 that the majority of the events tend to occur on the east side of well B. Although this may, in part, reflect observation bias due to the location of the monitor well, this pattern appears to correlate with a positive curvature anomaly running approximately N-S as shown in Figure 4.8b.

I cross-plotted microseismic event locations with magnitude and *b*-value statistics. Varying zones of magnitude and *b*-value are identified and projected onto the most positive curvature attribute at Glauconite level for correlation purposes. This overlay highlights relationships between magnitude, *b*-value statistics, rock fabric and observations from surface seismic.

I have divided magnitude-event density cross-plot into three zones and categorized them into three different ranges of magnitude, which are interpreted to represent ductile deformation, frac related events and brittle deformation or pre-existing zone of weakness.

Figure 4.11a, shows a magnitude-event density cross-plot. A zone of low-magnitude events (-2.2 to -2.6) is highlighted in red. Highlighted events may correlate with most positive curvature (k_1) anomalies. Low magnitude events in this zone are interpreted as associated with ductile deformation regime where fractures started to develop. A magnitude-event density cross-plot in Figure 4.12 shows the events highlighted with magnitude range of -1.6 to -2.2. Correlation with most positive curvature attribute reveals that most of the event population resides on or near most-positive curvature anomalies. Microseismicity in this zone is interpreted as operationally induced events that correlate closely with the hydraulic fracture treatment, within a brittle deformation regime. Finally, the largest magnitude events from the catalog exhibit a complex spatial distribution. Figure 4.13 shows a cross-plot that highlights zones of relatively high magnitude events, in a magnitude range from -1 to -1.6. Based on interpretation of the seismic attributes, it is found that the microseismic events with high magnitude correspond to the zones with a high degree of rock fabric, which may represent pre-existing zones of weakness, within a brittle deformation regime. Most of the post-pumping events reside in this zone, indicative of microseismicity that persisted after treatment operations were finished. Corresponding events appear to correlate with most positive curvature (k_1) anomalies, suggesting that the zones where re-activation of paleo-fractures might have occurred.

Another interesting correlation is found from the integration of microseismic event distribution and attribute analysis in Figure 4.14, where I have compared most positive (k_1) and most negative (k_2) curvature attributes with microseismic events. Both k_1 and k_2 extracted events are cross plotted against each other and a polygon highlighting a dense cloud of events is shown in Figure 4.14a. It is observed from the distribution of events that most of the events tend to stay in close proximity to most positive curvature anomalies but are distal from the most negative anomalies at the Glauconite level. This correlation suggests that zones of weakness where microseismic events are focused may represent subtle structural hinge lines that are detectable using 3D seismic.

4.2.2.2 *b*-value statistics analysis and rock-fabric

Haege et al., (2013) discuss the relationship of *b*-values with moment magnitude and rock fabric, wherein reactivation of pre-existing zones of weakness normally generates high magnitude events with relatively low tectonic *b*-value of ~1, whereas induced fracture related microseismicity is typically characterized by a higher *b*-value of ~2. The *b*-value can be computed by plotting the event magnitude distribution on a semi-log plot (Grob and van der

Baan, 2011). This distribution, which is also, called G-R relationship or Gutenberg-Richter relation (Gutenberg and Richter, 1944) indicates a power law behaviour represented by a linear curve and demonstrated in the formula:

$$\mathrm{Log}\, N = a - bM \quad , \qquad (4.1)$$

where N denotes the number of events with a magnitude $\geq M$, a and b are parameters that describe a given magnitude distribution. The slope of linear part of the curve thus represents the b-value for the events that are above the magnitude of completeness Mc - the smallest magnitude at which all events of that size are detectable (Wessels et al., 2011). Mc is estimated to be -2.0 for this study, as apparent in Figure 4.15. The constant b for specific event catalog represents the frequency of occurrence of different size of events; a higher b-value indicates a relatively greater proportion of small magnitude events compared to large magnitude events (Wessels et al., 2011).

The b-value has been calculated for event catalog, facies zones A, B and C (Figure 4.8) and for individual fracture stages summarized in Table 4.2. The computed b-value varies across different zones and stages. Statistical analysis of b-value (Table 4.2) and correlation with surface seismic attribute in Figure 4.17 suggests that the reservoir is compartmentalized, with different facies zones and rock fabric. A relationship of b-value variations with reservoir heterogeneity is discussed by El-Isa and Eaton (2014), who suggests that b-value is higher for a more ductile deformation regime, whereas a more brittle deformation regime yields lower b-value.

Although caution is required for over-interpreting b-value in cases where there are relatively few events (Boroumand., 2014), we observe that a cross-plot of b-value against treatment stages (Figure 4.16) shows unusually high b-value > 4 in 6 out of 24 stages (1, 6, 13, 14, 21, and 22). It is also evident from the figure that well B corresponds to higher b-value than well A. Higher *b*-value event stages are plotted onto most positive curvature in Figure 4.17a; comparison with magnitude statistics in Figure 4.11 suggests that these events correlate with low-magnitude zones where ductile deformation initiates. Mid-range *b*-value event stages i.e. (3, 4, 7, 8, 9, 10, 11, 12, 16, 17, 18, 19, 20, 23 and 24) are plotted back onto positive curvature in Figure 4.17b. This zone with a relatively complex spatial distribution of events is interpreted to represent a more brittle deformation zone, within which microseismicity is most directly linked with the hydraulic fracture treatment (e.g. a leak-off zone around the hydraulic fracture system). It is also noted that most of the events reside in this zone and also correlate with the facies zone B (Figure 4.8, 4.12). Lower *b*-value event stages i.e. (2, 5, PP1, 15 and PP2) are also plotted on most positive curvature in Figure 4.17c. When compared to magnitude statistics in Figure 4.13, it is seen that most of the post-pumping events reside in this zone, which is inferred to represent re-activation of paleo-fractures.

Magnitude statistics and *b*-value variation for facies zone A, B, and C thus suggest that the reservoir is compartmentalized. This compartmentalization may reflect different depositional environments with lithofacies varying from porous sandbars to silty interbar facies. To consider other influences on *b*-value such as rock fabric and in-situ stresses, a large distribution of microseismic event catalog is required (Boroumand., 2014). Ideally, the number of events for *b*-value analysis needs to be statistically comparable across all regions. Unfortunately, the data catalog provided suffered from incompleteness due to lack of event density in some stages. Consequently, some of the variability in *b*-value is undoubtedly related to catalog bias.

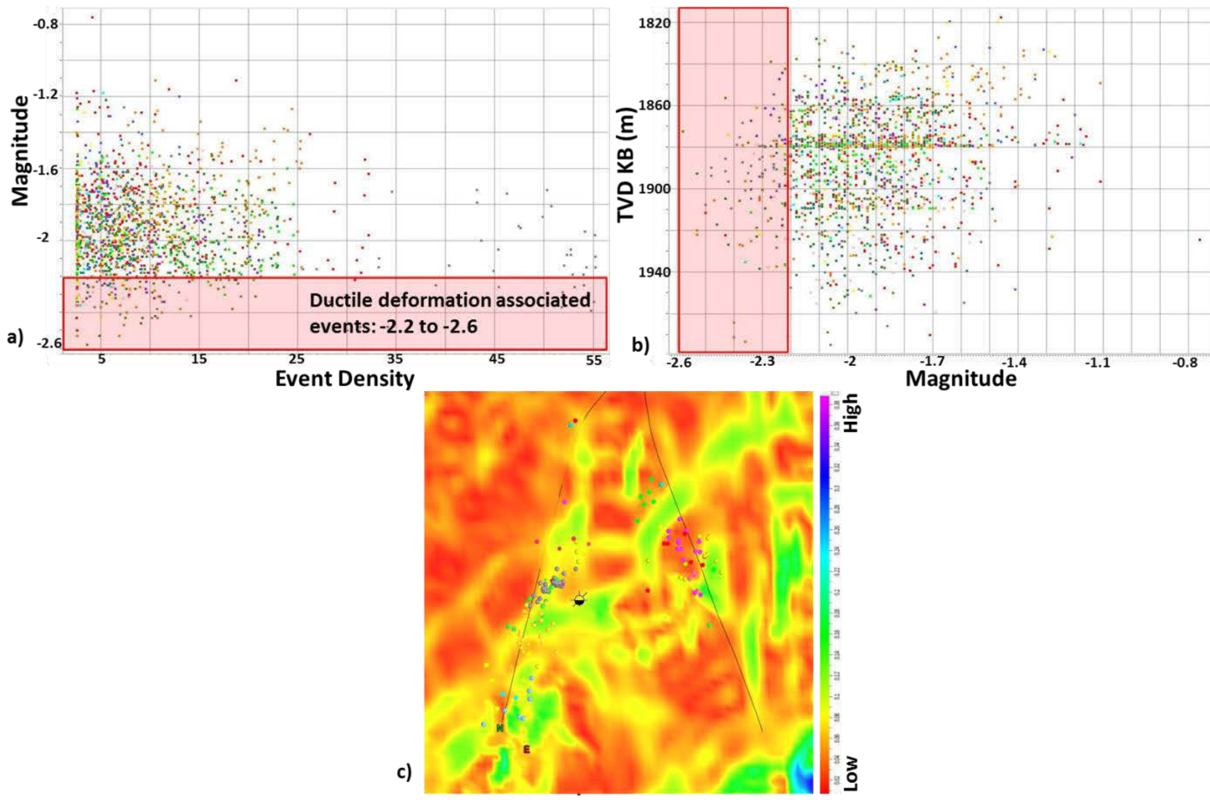

Figure 4.11: a) Magnitude-event density cross-plot highlighting a low magnitude range of -2.2 to -2.6, the zone showing where inferred ductile deformation initiated, b) TVD-magnitude cross-plot showing another view of low magnitude events, c) Low magnitude events plotted on most positive curvature (k_1), showing that fracture initiated on or near positive curvature anomaly.

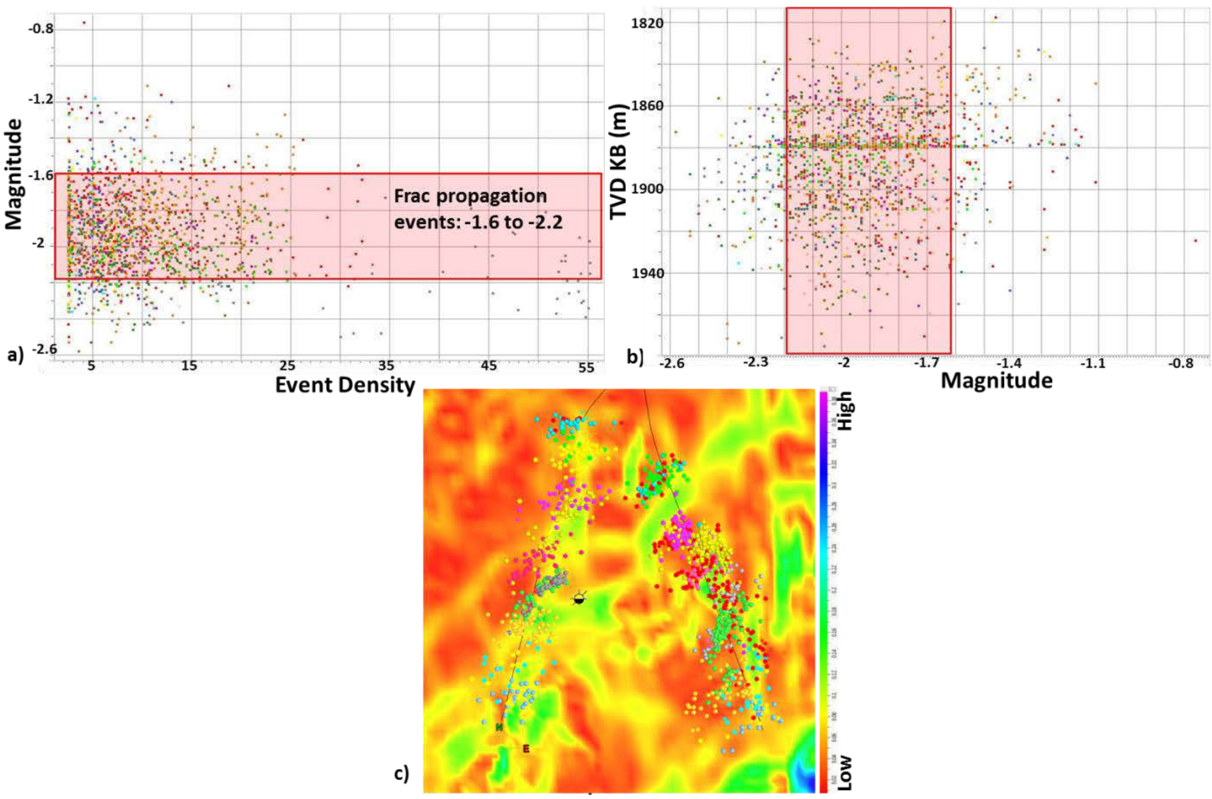

Figure 4.12: a) Magnitude-event density cross-plot, highlighting a magnitude range of -1.6 to -2.2, the zone where most of the hydraulic fracture treatment related events occur and inferred to represent a brittle deformation zone, b) TVD-magnitude cross-plot showing another view of microseismic distribution in this zone, c) Corresponding microseismic events plotted on most positive curvature (k_1), showing that most of the event population reside on or near most positive curvature anomalies, and are approximately aligned with regional maximum horizontal (SHmax) direction in a NE-SW orientation.

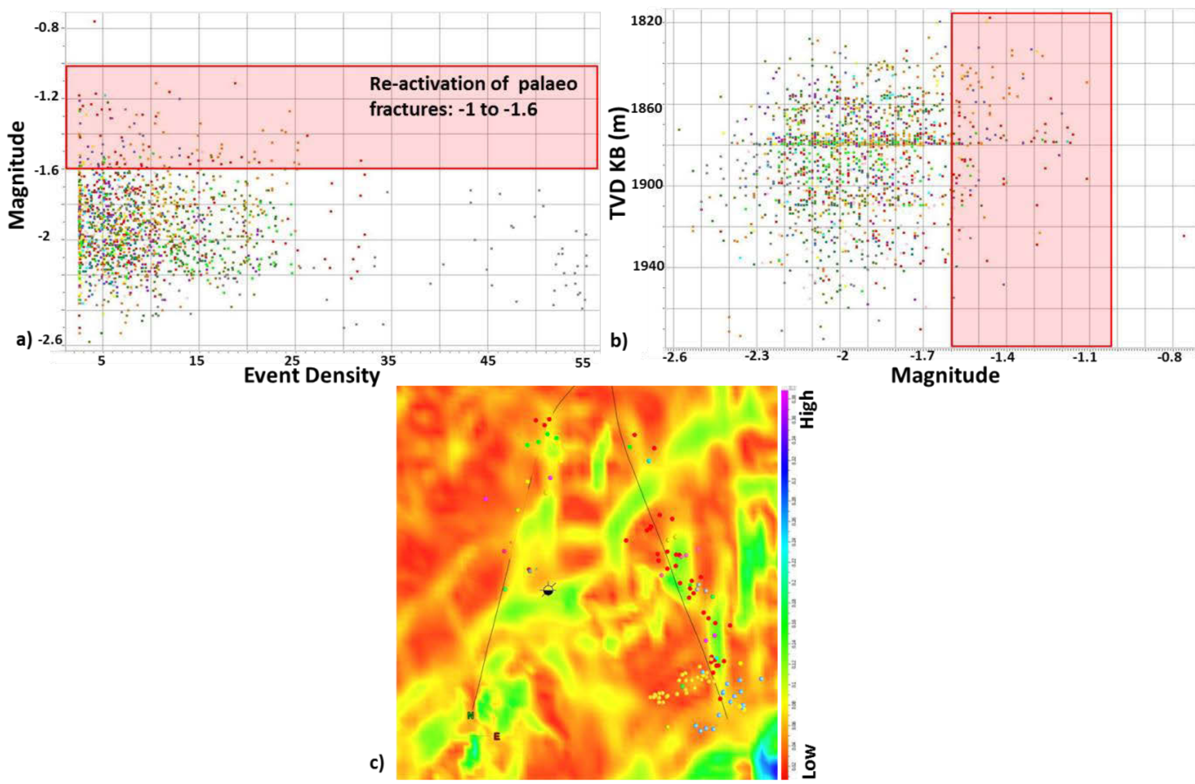

Figure 4.13: a) Magnitude-event density cross-plot highlighting a magnitude range of -1 to -1.6, interpreted as the zone showing where re-activation of paleo fractures occurred, b) TVD-magnitude cross-plot showing another view of high magnitude events, c) Corresponding high magnitude events plotted on most positive curvature (k_1), showing where inferred re-activation of natural fractures occurred.

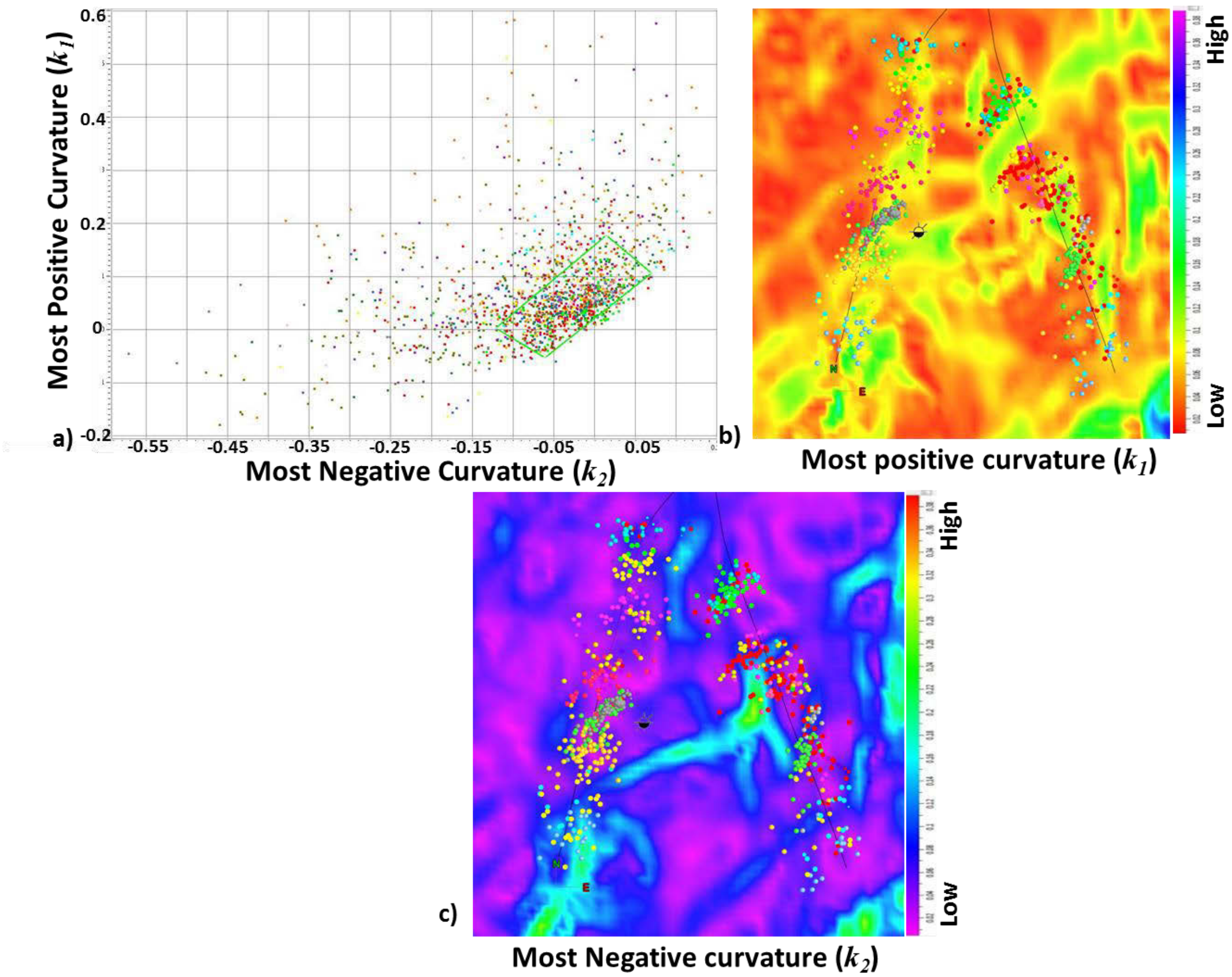

Figure 4.14: a) Cross-plot of most positive (k_1) and most negative (k_2) curvature attributes computed for microseismic events, polygon in green color showing dense cloud of events. Corresponding event cloud is plotted back onto, b) most positive curvature (k_1) attribute at Glauconite level, c) most negative curvature (k_2). Note that most of the events tend to be in close proximity to most positive curvature anomalies and avoid most negative anomalies.

Table 4.2: Summary of *b*-values calculated for each stage including post-pumping events.

Well Name	Stage #	*b*-Value	No. of Events
Well A & B	All Events	2.02	1660
Zone A	A	2.58	227
Zone B	B	2.00	1028
Zone C	C	3.23	270
Well A	1	**4.55**	38
	2	1.48	19
	3	2.43	33
	4	2.53	92
	5	1.91	109
	6	**4.7**	59
	7	2.82	51
	8	2.6	124
	9	3.01	72
	10	2.88	27
	11	2.22	81
	12	2.26	25
	PP1	1.59	240
Well B	13	**4.92**	33
	14	**4.01**	30
	15	1.92	18
	16	3.67	81
	17	3.36	86
	18	2.16	114
	19	2.9	67
	20	3.65	62
	21	**4.08**	41
	22	**4.3**	76
	23	2.5	22
	24	2.68	41
	PP2	1.3	19

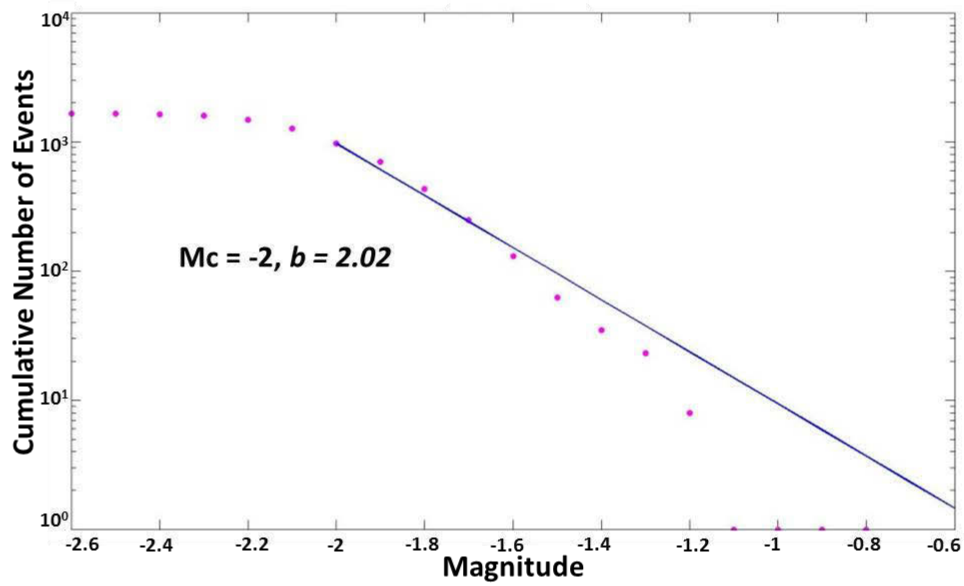

Figure 4.15: Magnitude-frequency distribution of seismicity of the whole catalog, obtained with a maximum likelihood formula (Aki, 1965). The fit on linear part of the curve indicates a *b*-value of 2.02.

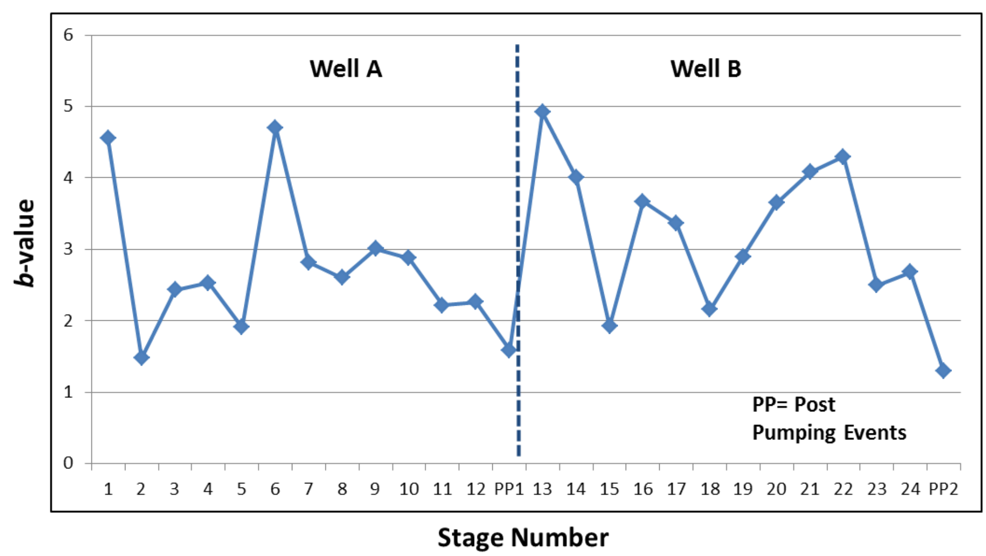

Figure 4.16: Variation of the *b*-value over 24 event stages. Six stages are characterized by relatively high *b*-value. In addition, note the relatively high *b*-value variations in well B.

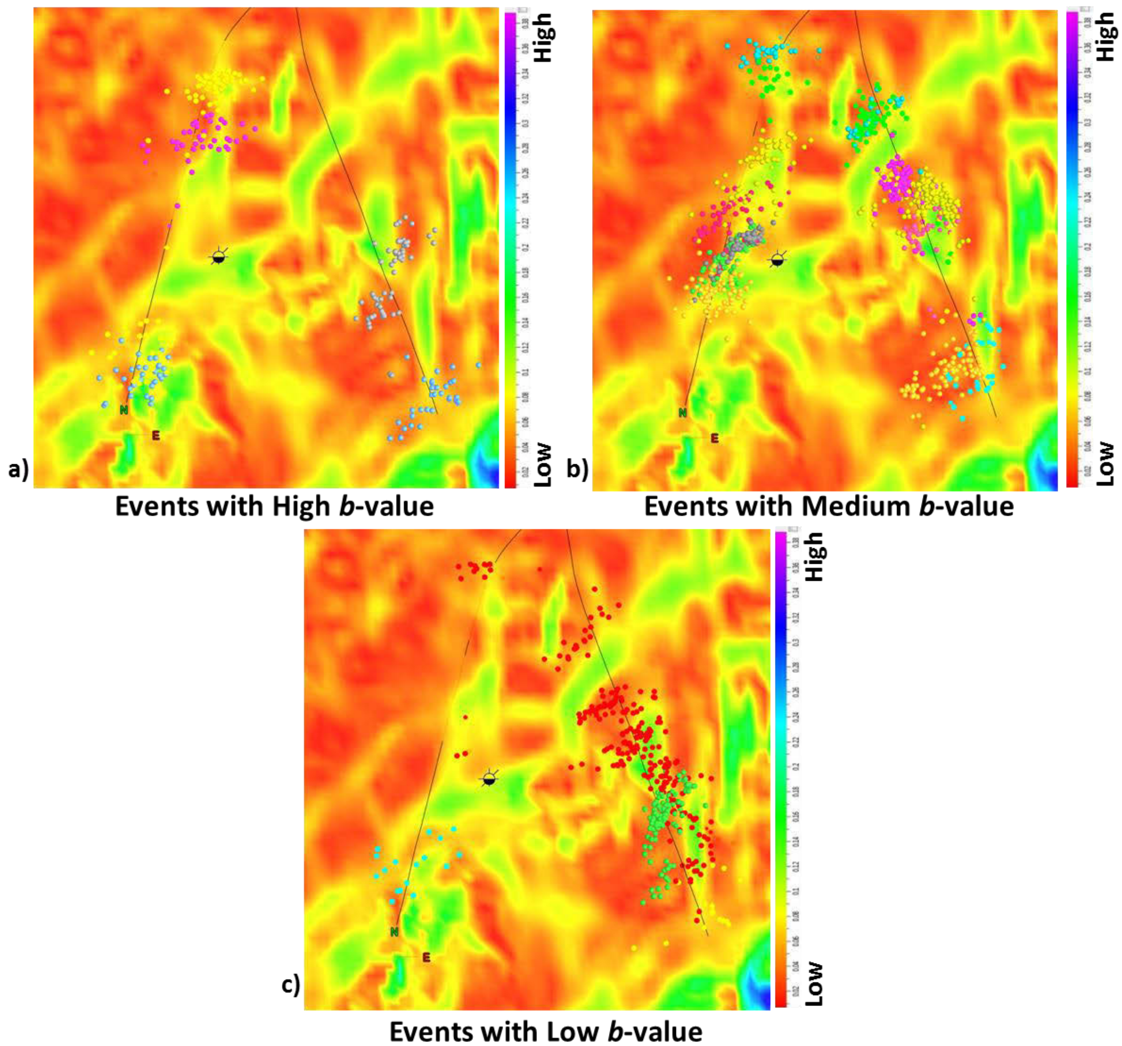

Figure 4.17: a) Event stages with high *b*-value projected back onto most-positive curvature, b) As in (a), for medium *b*-value treatment stages, c) As in (a), for low *b*-value treatment stages.

Chapter Five: **Conclusions and future directions**

Integrating microseismicity with surface seismic data can provide valuable insight for delineating unconventional reservoirs that may aid in further development of these resources. Based on various technical analysis and techniques used in this study, we make the following conclusions and suggest recommendations for future work.

- Microseismic events from the dataset considered here exhibit a complex spatial distribution, with ~50% oriented in the direction of SHmax i.e. NE-SW. The remaining events are oblique to SHmax and are inferred to represent reactivation of pre-existing fractures.
- Fracture heights vary between the two treatment wells A and B, although these wells are in close proximity (< 1 km). We attribute this to the differences in rock properties to variable characteristics of overlying, laterally extensive coals, silt and shale beds, where blunting of the microseismicity is observed along bedding plane.
- The majority of the events tend to occur on the east side of well B. This may in part reflect observation bias due to the location of the monitor well, but also appears to correlate with a positive curvature anomaly running approximately N-S.
- Curvature anomalies evident from surface seismic attributes may delineate hinge lines associated with potential depositional features, such as sandbar and interbar sands. For example, one feature is sub-parallel to regional depositional trend i.e. NE-SW (part of barrier bar complex), whereas another is transverse to the depositional trend (potential

connection with barrier bar) and is almost parallel to the sediment transport direction i.e. N-S direction.

- Comparing curvature anomalies with clusters in mean magnitude (*Mw*) and standard deviation (σ) cross-plot shows a set of attributes that are interpreted to be indicative of specific sedimentary depositional environment, In particular, integration of microseismic and 3D attributes may provide information about mechanical bed thickness and brittleness as well as heterogeneity. Based on the properties of these three cluster zones shown in Mw-σ cross-plot and their comparison with most positive curvature anomaly, we call these characteristics *"microseismic facies"*.
- Attribute analysis provides supportive evidence for my interpretation of the Hoadley barrier complex, which suggests that interbar sands may be associated with negative curvature anomalies. These features appear to limit fracture propagation and may lead to fracture asymmetry.
- Post-pumping events appear to correlate with reactivation of pre-existing fractures. About ~80% of the post pumping events are correlated with high magnitude and low *b*-value events. This evidence confirms that these events are related to pre-existing zones of weakness or high rock fabric.
- Variability of *b*-value, even from stage to stage in two *HZ* treatment wells is quite diverse. Large variation in *b*-value is apparent in our dataset, but caution is required as these may reflect bias arising from catalog incompleteness.
- Attribute analysis, magnitude statistics and *b*-value variations appear to reflect reservoir heterogeneity, rock fabric and compartments in the reservoir. These may in turn reflect variations in depositional environment and lithofacies.

5.1 Possible sources of error

In spite of the careful analysis, numerous inherent sources of errors resulting from the acquisition and processing of seismic and microseismic data need to be considered. The accuracy of located microseismic events is typically affected by the errors introduced in arrival-time picking and the selected velocity model. Akram (2014) discussed the impact of microseismic event location uncertainty due to arrival-time picking and velocity model errors. Figure 5.1 shows the propagation of arrival-time picking errors into hypocentre locations through a probabilistic approach. Assuming Gaussian distribution of observed arrival-time picks around their true values, a probability density function can be formed as follows:

$$P = Cexp(-0.5\left[\frac{\sum_{i=1}^{N}\left(t_{pi}^{o}-t_{pi}^{m}\right)^{2}}{\sigma_{p}^{2}}+\frac{\sum_{i=1}^{N}\left(t_{si}^{o}-t_{si}^{m}\right)^{2}}{\sigma_{s}^{2}}\right], \qquad (5.1)$$

Where C is a normalization factor, t^0 and t^m are the observed and model arrival times, σ_p and σ_s are the standard deviations of P- and S-arrivals. The uncertainty is shown for 10 microseismic events located at different source-receiver offset using 14 receivers with 15m spacing in a vertical borehole, for a homogeneous velocity model (Vp = 4500m/s and Vs = 2598m/s). The standard deviation for both P- and S-arrivals is 0.0025s. The uncertainty in microseismic events increase with source-receiver offset. The sources near the receiver array can be located with higher confidence as compared to the receivers at far offset, for microseismic data with varying S/N. The placement of receivers as compared to the source depth is another factor that can impact the accuracy of located events. The events situated at the center of an array get better receiver aperture and therefore can be located more accurately as compared to the events above or below the receivers where the angular aperture is poor (Akram, 2014). In our case, the receivers are located above the reservoir level (Figure 4.2), thus making them more sensitive to these errors.

Apart from these errors, errors in polarization angle estimates and subsurface velocity model contribute significantly to the hypocentre location accuracy. A flat layer constant velocity model is typically generated from sonic logs and calibrated using known source locations. Although calibrated, this only corrects for local velocity behavior and can introduce significant errors in the microseismic event locations.

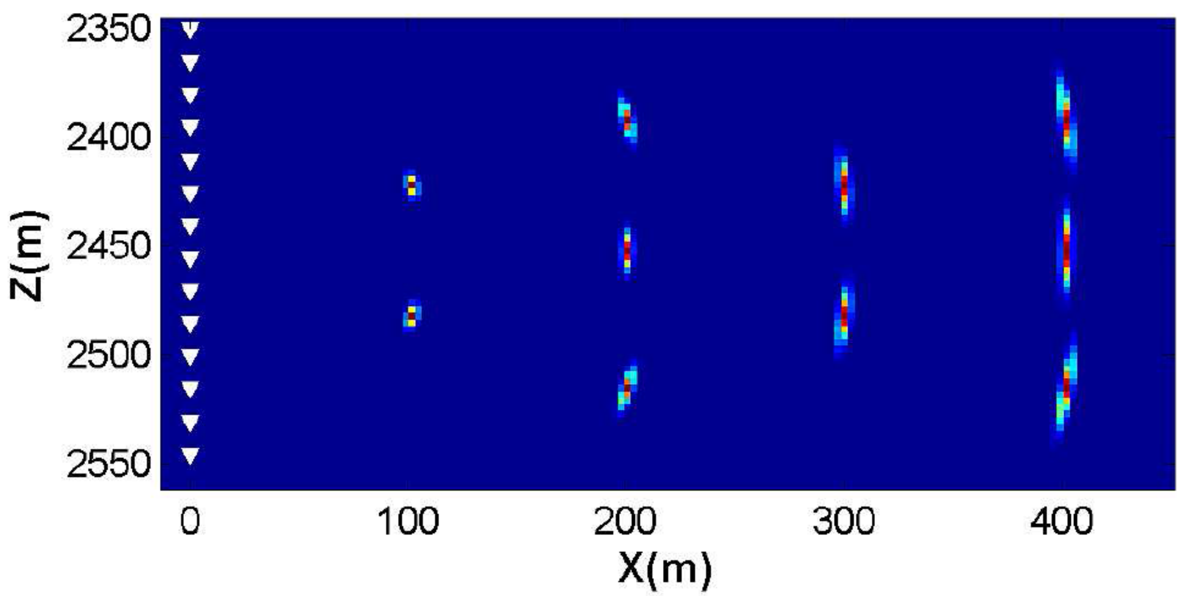

Figure 5.1: Example of microseismic location uncertainty in a homogenous velocity model due to 0.0025s standard error in arrival-time picks (from Akram, 2014). The uncertainty estimates using a probabilistic approach were computed for 10 sources and 14 receivers in a vertical well.

On the other hand, seismic data can also be affected by velocity model as it is used in time-to-depth conversion. Care must be taken in picking consistent velocity models for both seismic and microseismic data to avoid errors in depths which can ultimately impact their integrated correlation/interpretation. Other key factors which may cause errors in the interpretation are the acquisition footprint and the subsequent processing, poor well-to-seismic tie, and ignoring the use of common datum for comparisons of data from different sources.

5.2 Future directions

- This research should be extended by incorporating the inversion of pre-stack seismic data (if available). Using pre-stack seismic data can provide rock physics properties that can be used in combination with the seismic and microseismic attributes for improved understanding of the reservoir.

  The principal stresses and rock properties can be computed from mechanical attributes (ν, E) and anisotropic stress attributes (AVAZ, AVO) using wide-angle, wide-azimuth pre-stack seismic data. Simultaneous inversion of pre-stack 3D seismic data yields P-impedance (Zp), S-impedance (Zs), Vp/Vs, Poisson's ratio (ν) and Young's modulus (E). Zp and Zs are used as litho-fluid indicators, Poisson's ratio is TOC indicator and Young's modulus can be treated as brittleness indicator, which in turn is used to estimate information about reservoir skeleton.

- Seismic deformation seen at Glauconite level along the trajectory of well B, as positive curvature anomaly may be associated with depositional features, damage caused by extensive microseismic activity in this zone, or changes in velocity due to the injection of huge volume of hydraulic fracture fluid. It is therefore recommended to verify the anomaly through analyzing surface seismic data before and after hydraulic fracture stimulation, petrophysical analysis, waveform inversion or even re-processing of the seismic dataset.

- The current study presents a general framework of how microseismic information can be utilized in terms of understanding unconventional reservoirs. I recommend a more detailed microseismic analysis including source parameters such as moment tensors for the integrated work.

References

Aki, K., 1965, Maximum likelihood estimate of *b* in the formula log (N) = a − *b*M and its confidence limits: Bulletin of Earthquake Research Inst. (BERI) Tokyo University, **43**, 237-239.

Aki, K., Fehler, M., Aamodt, R.L., Albright, J.N., Potter, R.M., Pearson, C.M., and Tester, J.W., 1982, Interpretation of seismic data from hydraulic fracturing experiments at the Fenton Hill, New Mexico, Hot Dry Rock Geothermal site: Journal of Geophysical research, Vol **87**, No. B2, Feb 10, 1982.

Akram, J., Eaton, D., and St.Onge, A., 2013, Automatic event-detection and time picking algorithms for downhole microseismic data processing: 4th EAGE Passive Seismic Workshop.

Akram, J., 2014, Downhole microseismic monitoring: processing, algorithms and error analysis: Ph.D. Dissertation, The University of Calgary, Alberta.

Barber, C., Dobkin, D.P. and Huhdanpaa, H., 1993, The Quickhull algorithm for convex hull: Geometry Centre Technical Report GCG **53**, University of Minnesota, 15 pp.

Barclay F., Bruun, A., Rasmussen, K.B., Camara-Alfaro, J., Cooke, A., Cooke, D., Salter, D., Godfrey, R., Lowden, D., McHugo, S., Ozdemir, H., Pickering, S., Gonzalez-Pineda, F., Herwanger, J., Volterrani, S., Murineddu, A., Rasmussen, A., and Roberts, R., 2008, Seismic inversion reading between the lines: Oilfield Review, Spring, 42–63.

Barnes, A. E., 1997, Genetic classification of complex seismic trace attributes: 67^{th} Annual International Meeting: SEG, Expanded Abstracts, 1151-1154.

Boroumand, N., 2014, Hydraulic fracture *b*-value from microseismic events in different regions: Geoconvention 2014.

Brown, A.R., 2004, Interpretation of Three-Dimensional Seismic Data: Sixth edition, AAPG Memoir 42, SEG Investigations in Geophysics, No.**9**.

Canadian Society for Unconventional Resources, 2014, Understanding hydraulic fracturing: Retrieved January 22, 2015, from CSUR: http://csur.com/.

Canadian Society for Unconventional Resources, 2012, What are unconventional resources, Alberta: Retrieved January 25, 2015, from CSUR: http://csur.com/.

Chen, Q., and Sidney, S., 1997, Seismic attribute technology for reservoir forecasting and monitoring: The Leading Edge, **16**, 445-456.

Chiang, K. K., 1984, The giant Hoadley gas field, south-central Alberta - In J.A. Masters, (Ed), Elmworth - Case study of a deep basin gas field: AAPG Memoir, **38**:297-313.

Chirinos, X.E.R., 2010, Hydraulically-Induced Microseismic Fracture Characterization from Surface Seismic Attributes and Seismic Inversion: A North Texas Barnett Shale Case Study: Ph.D. Diss. University of Oklahoma.

Chopra, S., and Larsen, G., 2000, Acquisition Footprint-Its detection and removal: CSEG Recorder, October 2000: pp. 16-20.

Chopra, S., and Marfurt, K.J., 2005, Seismic Attributes-A historical perspective: Geophysics, Vol. **70**, No.5 - P.3SO-28SO, 32 FIGS. 10.1190/1.2098670.

Chopra, S., and Marfurt, K. J., 2007, Seismic Attributes for prospect identification and reservoir characterization: Geophysical developments No.**11**.

Chopra, S., and Marfurt, K.J., 2008, Gleaning meaningful information from seismic attributes: First Break, **26**(9), 43-53.

Chopra, S., and Marfurt, K. J., 2012, Interesting directions being pursued in seismic curvature attribute analysis: SEG Technical Program Expanded Abstracts 2012: pp. 1-6.

Churcher, P.L., Kenny, J., Lamb, D.H., and Flach, P.D., 1996, Characterizing Horizontal Well Performance in a Tight Gas Sand Using Pressure Transient, Production Logging and Geological Data: SPE-37127.

Das, I., and Zoback, M. D., 2013a, Long-period, long-duration seismic events during hydraulic stimulation of shale and tight-gas reservoirs -Part 1: Waveform characteristics: Geophysics, **78**, KS97–KS108.

Das, I., and Zoback, M.D., 2013b, Long-period long-duration seismic events during hydraulic stimulation of shale and tight gas reservoirs -Part 2: Location and mechanisms: Geophysics, **78**, KS109-KS117.

Eaton, D. W., and Forouhideh, F., 2011, Solid angles and the impact of receiver array geometry on microseismic moment-tensor inversion: Geophysics, **76**, no. 6, WC77–WC85.

Eaton, D., Maulianda, B., Hareland, G. and Chen, N., 2013, Estimation of stimulated reservoir volume (SRV) using microseismic observations: Microseismic Industry Consortium, Annual Research Report, Volume **3**: 305-310.

Eaton, D. W., Davis, C., Matthews, M., van der Baan, M., Mostafa, M., Costa Sousa, M., Brazil, E., William-Kovacs, J., and Clarkson, C., 2013a, Hoadley flowback microseismic experiment, Progress Report: In van der Baan, M., and Eaton, D., (Eds), Microseismic Industry Consortium, Annual Research Report, **3**: 95-114.

Eaton, D. W., van der Baan, M., Caffagni, E., Rafiq, A., Roche, V., and Tary,J.B., 2014, Hoadley Microseismic Experiment: Passive seismic monitoring of a tight-sand reservoir during hydraulic-fracture treatment, flowback and production.: Microseismic Industry Consortium, Annual research report Volume **4**-2014-89-104.

Eaton, D. W., Rafiq, A., Pedersen, P. and van der Baan, M., 2014a, Microseismic expression of natural fracture activation in a tight sand reservoir: DFNE 2014 – 265.

Eaton, D.W., Caffagni, E., Rafiq, A., van der Baan, M., Roche, V. and Matthews, L., 2014b, Passive seismic monitoring and integrated geomechanical analysis of a tight-sand reservoir during hydraulic-fracture treatment, flowback and production: URTeC 1929223.

Eaton, D.W., Davidsen, J., Pedersen, P. and Boroumand, N., 2014c, Breakdown of the Gutenberg-Richter relation for microearthquakes induced by hydraulic fracturing: influence of stratabound fractures. Geophys. Prosp. **62**, 806-818.

Eisner, L., Thornton, M., and Griffin, J., 2011, Challenges for microseismic monitoring: SEG San Antonio Annual Meeting, 2011.

El-Isa, Z.H., and Eaton, D.W., 2014, Spatiotemporal variations in the *b*-value of earthquake magnitude–frequency distributions: Classification and causes. Tectonophysics 615-616 (2014) 1-11.

Giger, F., Reiss, L., Jourdan, A., 1984, The reservoir engineering aspects of horizontal drilling: SPE Annual Technical Conference and Exhibition, SPE-13024-MS.

Grob, M., and van der Baan, M., 2011, Statistical analysis of Microseismic event locations and magnitudes, and their geomechanical implications: Recovery, 2011 CSPG CSEG CWLS convention.

Gutenberg, B., and Richter, C.F., 1944, Frequency of earthquakes in California: Bulletin of the Seismological Society of America (BSSA)-944 34:185-188.

Haas, A., and Dubrule, O., 1994, Geostatistical inversion-A sequential method of stochastic reservoir modeling constrained by seismic data: First Break, **12**, 561.

Haege, M., Maxwell, M., Sonneland, L. and Norton, M., 2013, Rock fabric and microseismic: an integrated approach: Geoconvention 2013.

Hampson-Russell Geoview software user manual, 2013, Post stack inversion guide: version **1**, HRS-9 R2.0.3.

Hampson-Russell Strata, 2013, Strata post-stack seismic inversion workshop: presentation slides.

Hayes, B.J.R., Christopher, J.E., Rosenthal, L., Los, G., McKercher, B., Minken, D., Tremblay, Y.M., and Fennell, J., 1994, Cretaceous Mannville Group of the Western Canada: Geological atlas of western Canada sedimentary basin, Chapter **19**, Retrieve December 05, 2014, www.ags.gov.ab.ca.

Heffernan, K., and Dawson, F.M., 2010, An overview of Canada's natural gas resources: CSUG, May 2010.

King, G. E., 2012, Hydraulic fracturing 101: What every representative environmentalist regulator reporter investor university researcher neighbor and engineer should know about estimating frac risk and improving frac performance in unconventional gas and oil wells: SPE Hydraulic Fracturing Technology Conference, 2012.

Latimer, R. B., Davison, R., and van Riel, P., 2000, An interpreter's guide to understanding and working with seismic-derived acoustic impedance data: The Leading Edge, **19**, 242–256.

Liner, C., Li, C.F., Gersztenkorn, A., and Smythe, J., 2004, SPICE: A new general seismic attribute: 74th Annual International Meeting, SEG, Expanded Abstracts, 2004-0433-436.

Mai, H.T., 2010, Seismic attribute analysis and its application to mapping folds and fractures: Ph.D. Dissertation, The University of Oklahoma, Norman, Oklahoma.

Maxwell, S.C., Urbancic, T.I., Steinsberger, N., and Zino, R., 2002, Microseismic imaging of hydraulic fractures complexity in Barnett Shale: SPE-77440.

Maxwell, S.C., Jones, M., Parker, R., Leaney, S., Mack, M., Dorval, D., D'Amico, D., Logel, J., Anderson, E., and Hammermaster, K., 2010, Fault Activation During Hydraulic Fracturing: AAPG search and discovery article # 90172, Geoconvention 2010.

Maxwell, S.C., Cho, D., Pope, T., Jones, M., Cipolla, C., Mack, M., Henery, F., Norton, M. and Leonard, J., 2011, Enhanced reservoir characterization using hydraulic fracture microseismicity: SPE 140449.

Maxwell, S., 2014, Microseismic imaging of Hydraulic fracturing: Improved engineering of unconventional shale reservoirs: SEG distinguished instructor short course series, no. **17**.

Naik, G.C., 2010, Tight gas reservoirs-An unconventional natural source for the future: Retrieved January 22, 2015, from (www.pinedalenline.com/socioeconomic/pdfs/tight_gas.pdf).

Nash, K.M., 2010, Shale gas development: Nova science publishers, incorporated, pp.174.

Newbert, J.D., and Trick, M.D., 1987, A Systematic Deliverability Analysis for the Hoadley Gas Condensate Field: SPE-16938.

Oldenburg, D.W., Scheuer, T., and Levy, S., 1983, Recovery of the acoustic impedance from reflection seismograms: Geophysics, **48**, 1318.

Pelaez, A.S.R., 2012, Prediction of reservoir quality with seismic attributes in Eocene submarine conglomerates (calclithites), Mexico: M.S. Thesis, The University of Oklahoma, Norman, Oklahoma, 27 p.

Pike, K., 2014, Microseismic Data Processing, Modeling and Interpretation in the Presence of Coals: A Falher Member Case Study. MSc. Thesis, University of Calgary, 176 pp.

Reinecker, J., Heidbach, O., Tingay, M., Sperner, B. and Müller, B., 2005, The release 2005 of the World Stress Map: Retrieved February 18, 2014, from http://www.world-stress-map.org.

Reynolds, M., Thomson, S., Peyman, F., Hung, A., Quirk, D., and Chen, S., 2012, A Direct Comparison of Hydraulic Fracture Geometry and Well Performance Between Cemented Liner and Open Hole Packer Completed Horizontal Wells in a Tight Gas Reservoir: SPE 152185.

Roberts, A., 2001, Curvature attributes and their application to 3D interpreted horizons: First Break, **19**, no. 2, 85-100.

Russell, B.H., 1988, Introduction to seismic inversion methods: Course Notes Series, 2, SEG.

Russell B., and Hampson, D., 2006, The old and the new in seismic inversion: CSEG Recorder, December, 5-11.

Smith, D.G., 1994, Paleogeographic Evolution of the Western Canada Foreland Basin, In Geological Atlas of the Western Canada Sedimentary Basin, ed. G.D. Mossop and I. Shetsen, CSPG and Alberta Research Council.

Sorensen, F., and Little, L.C., 1993, A 3-Dimensional Approach to the Modelling of the Hoadley Westerose Gas Reservoir/Surface Pipeline Network: SPE-26143.

Stefik, R. G., and Paulson, K., 2011, When Unconventional Becomes Conventional. SPE-136863.

Surdam, R. C., 1997, A New Paradigm for Gas Exploration in Anomalously Pressured Tight Gas Sands in the Rocky Mountain Laramide Basins: AAPG Memoir, **67**:283-298.

Taner, M.T., Schuelke, J.S., O'Doherty, R., and Baysal, E., 1994, Seismic attributes revisited: 64th Annual international meeting, SEG, Expanded Abstracts, 1104-1106.

Transform software user guide, 2015, Seismic processing, mapping algorithms: TerraSuite 4.1.

Unconventional sources of gas in Canada: Retrieved January 24, 2015, www.history.alberta.ca.

Walker, R.N., 1997, Cotton valley Hydraulic Fracture Imaging Project: Journal of Petroleum Engineering-SPE 38577-1997.

Warpinski, N., 2009, Microseismic monitoring: inside and out: Journal of Petroleum Technology, November 2009, pp. 80-85, DOI: 10.2118/118537-MS.

Wessels, S.A., Pena, A.D.L., Kratz, M., Stround, S.W, and Jbeili, T., 2011, Identifying faults and fractures in unconventional reservoirs through microseismic monitoring: First break Vol.**29**. July 2011.

Williams-Kovacs, J.D., and Clarkson, C.R., 2011, Using stochastic simulation to quantify risk and uncertainty in shale gas prospecting and development: CSUG/SPE 148867.

Zimmer, U., Maxwell, S., Waltman, C. and Warpinski, N., 2007, Microseismic monitoring quality-control (QC) reports as an interpretive tool for nonspecialists: SPE 110517.

APPENDIX A: CONTINUOUS DATA ANALYSIS

One of the objectives of HFME was to perform long-term monitoring of post-frac microseismicity during flowback and production period.

The continuous data harvested for 10.5- month period following the fracture treatment have been visually inspected, including triggered event files by using ESG's WaveVis software. A scheme is developed to classify the events (Eaton et al., 2014b), as described below:

1. Potential high-frequency microseismic events (similar in character to microseismic events recorded and located during the fracture treatment);
2. Low-frequency tremor, characterized by coherent, long-duration, low-frequency (< 100 Hz) energy. Groups of triggered events (1.5 s time window) that are very similar in time are classified as a single tremor event. Possible sources of these signals may include long-period long-duration (LPLD) events (Das and Zoback, 2013a, 2013b) or local earthquakes;
3. Tube waves, which propagate across the array at water velocity (~ 1500 m/s);
4. Low frequency events (LFEs) that show distinct arrivals that appear to be P- and S-waves, but with frequency content similar to tremor;
5. Long Period Long Duration (LPLD) events, with characteristics similar to the events described by Das et al., 2013.

Figure A.1 shows some of the representative examples of events from each of these types. Frequency of occurrence of various types of microseismic events during the HFME project is shown in Figure A.2. The known sources of noise including diesel generator that was used in the first month of recording, dynamite source used for 3D seismic acquisition in January 2013, and spring farm activities are shaded with different colors to facilitate recognition of specific activity. Approximately 23517 triggered events and 16 potential earthquakes were observed during analysis of continues stream of data recorded for 10.5 months. It is obvious from the analysis that some type of events such as LPLD and low frequency tremors occurs in bursts of activity that is not related to the noise sources (Eaton et al., 2014).

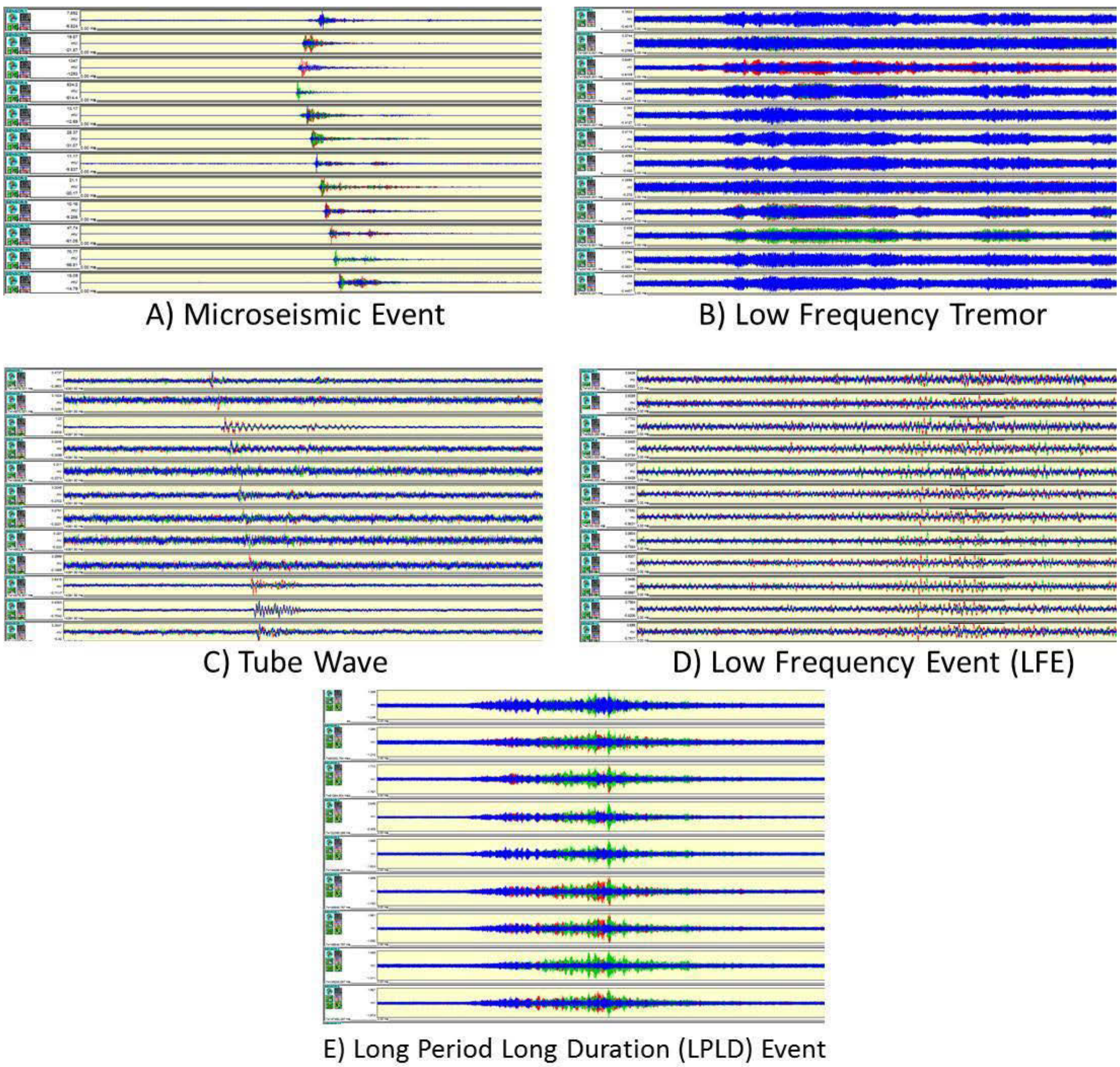

Figure A.1: Example of different classes of events recognized in continuous data analysis. a) Microseismic event, b) Low frequency tremor, c) Tube waves, d) Low frequency event (LFE), e) Long period long duration (LPLD) event.

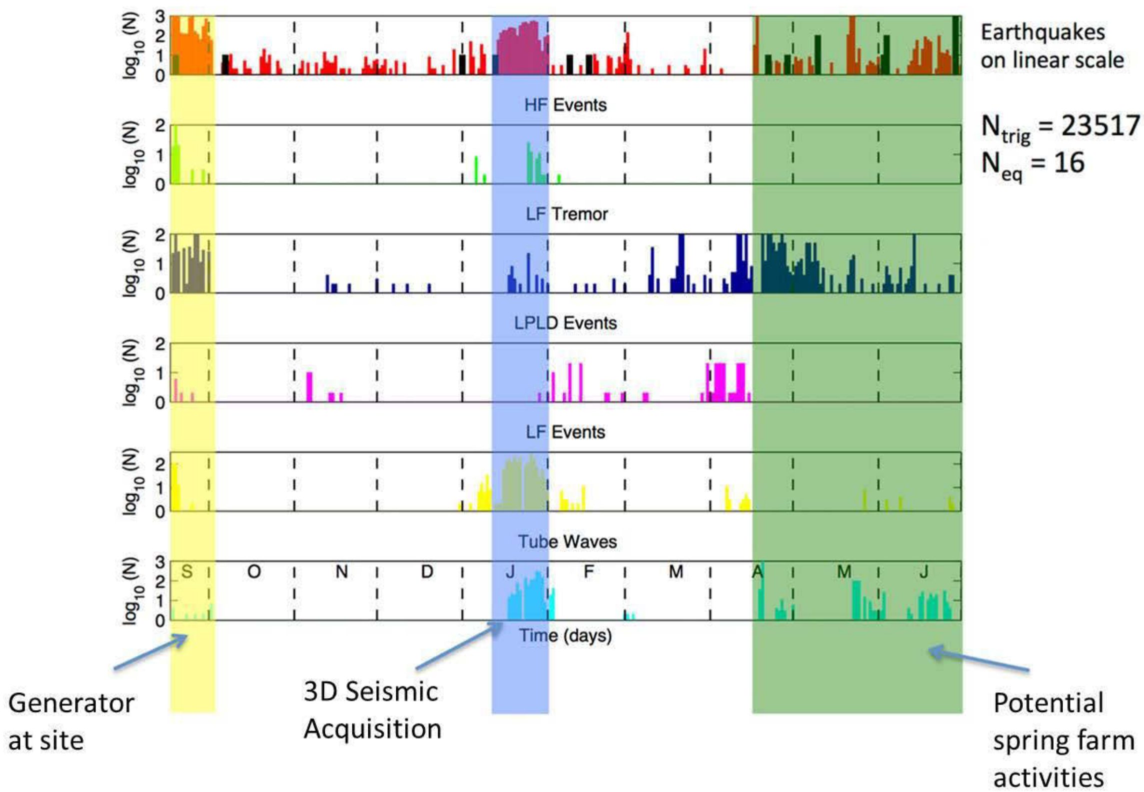

Figure A.2: Frequency of occurrence of different type of events over the period during HFME project (modified from Eaton et al., 2014).